A new method to reduce artifacts (MAR), produced by high-density objects, especially metal implants (MI), in X-ray CBCT is presented. MIs located in the field of view (FOV) result in artifacts influencing clinical diagnostics and treatments. The novel method reduces metal artifacts by virtually replacing MIs by tissue objects of the same shape. This corrected data can be reconstructed with significantly reduced artifacts. After reconstruction, the segmented 3D MIs were re-inserted into the corrected 3D volume. The method was developed for mobile C-arm CBCTs, where misalignments between original 2D data and forward projections must be adjusted before correction.

While doing research on MAR it became obvious that large MIs were hard to segment. Since a good segmentation is a very important prerequisite for an efficient MAR, therefore it was necessary to develop a new segmentation technique by combining two thresholding processes with a reconstruction.

These techniques are applied to clinical data and the results are presented.

Universitätsverlag Regensburg

ISBN 978-3-86845-074-3

gefördert von:

Alumni der physikalischen Fakultät der Universität Regensburg e.V.

Universität Regensburg

Dissertationsreihe Physik - Band 20

Manuel Meilinger

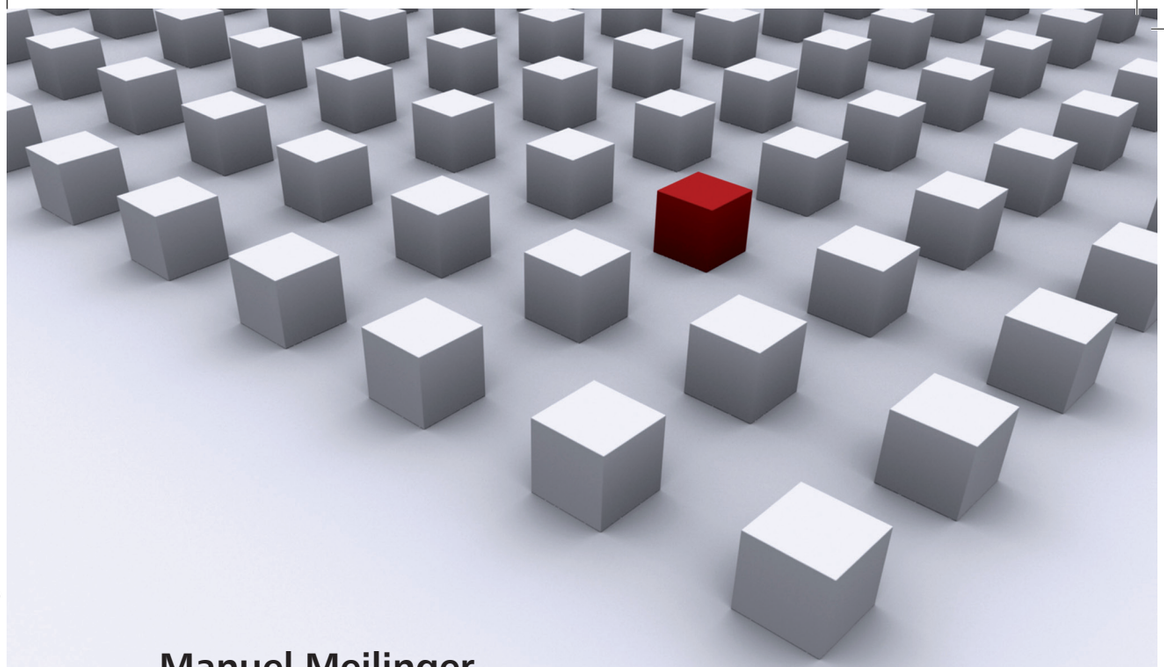

Manuel Meilinger

Metal Artifact Reduction and Image Processing of Cone-Beam Computed Tomography Data for Mobile C-Arm CT Devices

Universitätsverlag Regensburg

Manuel Meilinger

20

Dissertationsreihe Physik

Manuel Meilinger

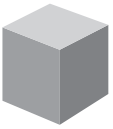

Metal Artifact Reduction and Image Processing of Cone-Beam Computed Tomography Data for Mobile C-Arm CT Devices

Metal Artifact Reduction and Image Processing of Cone-Beam Computed Tomography Data for Mobile C-Arm CT Devices

Dissertation zur Erlangung des Doktorgrades der Naturwissenschaften (Dr. rer. nat.)
der Fakultät für Physik der Universität Regensburg
vorgelegt von

Manuel Meilinger

aus Regensburg
2010

Die Arbeit wurde von Prof. Dr. Elmar W. Lang angeleitet.
Das Promotionsgesuch wurde am 03.12.2010 eingereicht.

Prüfungsausschuss: Vorsitzender: Prof. Dr. Ingo Morgenstern
1. Gutachter: Prof. Dr. Elmar W. Lang
2. Gutachter: Prof. Dr. Josef Zweck
weiterer Prüfer: Prof. Dr. Karsten Rincke

Dissertationsreihe der Fakultät für Physik der Universität Regensburg, Band 20

Herausgegeben vom Präsidium des Alumnivereins der Physikalischen Fakultät:
Klaus Richter, Andreas Schäfer, Werner Wegscheider, Dieter Weiss

Manuel Meilinger

Metal Artifact Reduction and Image Processing of Cone-Beam Computed Tomography Data for Mobile C-Arm CT Devices

Universitätsverlag Regensburg

Fakultät für Biologie und Vorklinische Medizin
Institut für Biophysik und physikalische Biochemie
Computational Intelligence and Machine Learning Group
Universität Regensburg
Universitätsstraße 31
D-93040 Regensburg
►http://www-aglang.uni-regensburg.de

In Zusammenarbeit mit:

SIEMENS

Siemens AG
Healthcare Sector
Special Systems Division
SIM H WS SP S R&D 6
Allee am Röthelheimpark 2
D-91052 Erlangen
►http://www.medical.siemens.com

Bibliografische Informationen der Deutschen Bibliothek.
Die Deutsche Bibliothek verzeichnet diese Publikation
in der Deutschen Nationalbibliografie. Detailierte bibliografische Daten
sind im Internet über http://dnb.ddb.de abrufbar.

1. Auflage 2011

Leibnizstraße 13, 93055 Regensburg

Konzeption: Thomas Geiger
Umschlagentwurf: Franz Stadler, Designcooperative Nittenau eG
Layout: Manuel Meilinger
Druck: Docupoint, Magdeburg
ISBN: 978-3-86845-074-3

Weitere Informationen zum Verlagsprogramm erhalten Sie unter:
www.univerlag-regensburg.de

Metal Artifact Reduction and Image Processing of Cone-Beam Computed Tomography Data for Mobile C-Arm CT Devices

DISSERTATION ZUR ERLANGUNG DES DOKTORGRADES DER NATURWISSENSCHAFTEN (DR. RER. NAT.)
DER FAKULTÄT FÜR PHYSIK DER UNIVERSITÄT REGENSBURG

vorgelegt von

Manuel Meilinger

aus
Regensburg

im Jahr 2010

Die Arbeit wurde durchgeführt am **Institut für Biophysik und physikalische Biochemie** unter der Anleitung von **Prof. Dr. Elmar W. Lang** in Zusammenarbeit mit dem Geschäftsgebiet ‚Special Systems' des Geschäftsbereiches ‚Healthcare Sector' der Siemens AG in Erlangen unter der Betreuung von **Dr. Christian Schmidgunst** und **Dr. Oliver Schütz**.

Promotionsgesuch eingereicht am: 03.12.2010

Prüfungsausschuss:	Vorsitzender:	Prof. Dr. Ingo Morgenstern
	1. Gutachter:	Prof. Dr. Elmar W. Lang
	2. Gutachter:	Prof. Dr. Josef Zweck
	weiterer Prüfer:	Prof. Dr. Karsten Rincke

Contents

Acknowledgments

I would like to thank everybody who helped me in any kind of way to conclude my dissertation.

Universität Regensburg

- First I'd like to thank my doctoral thesis advisor **Prof. Elmar W. Lang** for his professional advice and the cooperative working atmosphere.
- Furthermore, I want to thank the members of staff of the CIML group for their know-how and constructive reviews, especially **Dr. Ingo Keck** with whom I had a lot of interesting and inspiring discussions both about research and private, **Dietmar Birzer** who did his diploma thesis about digital subtraction angiography in cooperation with Siemens and **Sabrina Michailoff** who did a internship about segmentation in our group.

Siemens Healthcare Sector - Erlangen

- First of all, special thanks go to my advisors **Dr. Christian Schmidgunst** and **Dr. Oliver Schütz**, who already supervised my diploma thesis. For each technical or private question, both were at hand and gave willing advice and answers.
- **Alexander Neagu**, I thank for the good working atmosphere and very good reception in his group.
- Further I want to thank all the other employees from Siemens in Erlangen, mainly **Dr. Rainer Graumann**, **Dr. Holger Scherl**, **Dr. Markus Kowarschik** and **Stefan Schneider** for their advice and the productive discussions during visits in Erlangen or on conferences.

Family and friends

- Special thanks go to my **parents** for the immense support during my study at university and in my whole life.
- Furthermore I want to thank my girlfriend **Carina** for every hour in our past years together, for every word of counsel, for tolerating me and especially for her love.
- A lot of thanks go to my friends also, who accompanied me during my study and my life. Also a lot of thanks go to **Dr. Anja Scholten**, and **Rick Wynne** who gave me advice and revision about my doctoral thesis.
- And last but not least, again **Eddi**.

Introduction

Motivation

Since its discovery in the 19th century (first publication from W.C. Röntgen December 1895 [44]) X-rays evolved very fast to a very common examination and treatment technology in medicine. And about 70 years after this publication, in addition to 2D imaging Hounsfield developed - with preliminary work from Cormack - the Computed Tomography (CT) [16]. During several scans from different positions a line scan series is acquired. From these lines, scanned from outside of the object of interest, it is possible to compute a 2D image showing the inside of the object using inverse radon-transformation (published by J. Radon in 1917 [40]) or other reconstruction procedures.

Over the years the number of simultaneously scanned lines increased. New techniques like helical CT or dual source CT were developed. A detailed survey until 1990 is described in Webb [56], Kalender [24] gives an overview till 2009. Within this period, the rotation time decreased from 9 days, in the first CT scan from Hounsfield 1968 (he had to use a γ-source instead of an X-ray tube) [56, 58], to 4 minutes during the experiments by Ambrose in 1973 [19] until today at about 300 milliseconds.

Another new engineered technique is the Cone-Beam CT (CBCT). The CBCT is a further development of multi slice CT's. Instead of an array of slices, each irradiated with a fan beam, a whole image is acquired in each angular step. In the beginning X-ray image intensifiers were used, until they were replaced with flat panel detectors (FP) [45].

The C-arm concept is another advance in CT technology. Mobile CT's allow using them during surgeries in the operation room. Patients can be scanned and operated without change in position, which is an important advance e.g. for navigation during surgery. Mobile C-arm CTs using normal electrical connection can be used in every room, reducing the storage space and increasing the usability in conflict areas. The main disadvantage of these mobile devices in the comparison to a fixed gantry is the instability of the C-arm and consequently higher rotation times and unpredictable distortion.

From the beginning CT had to deal with metal artifacts. Shadows and streaks, protruding from metal implants, in the reconstructed images disturb diagnosis or treatment planning. With increasing use of CT imaging in medical applications, the developments in implant surgery and the increasing age of patients, the number of X-ray CT scans with metal objects inside the scan area also increases. For example: In cancer diagnosis and treatment planning CT imaging is used. The most often diagnosed cancer by male patients is prostate cancer and the second most diagnosed cancer for both sex is colorectal cancer[17]. Also most cancer patients are the elderly, but this population group also has the greatest probability for a hip replacement. Colon, rectum, prostate and the hip joints are located in the same segment of the human body, so scans in this area often have to deal with metal artifacts. Additionally, surgeons are interested in checking the position of metal implants after surgery. The possibility of an mobile C-arm CT with reduced, or even without, metal artifacts will allow a quick and easy check of the region of interest, subsequent to the surgical intervention.

Several methods have been published to correct images corrupted by streak artifacts. Some of them treat beams through high-density objects as missing. Other, corrective methods, in which defective segments in the sinogram of CT images are interpolated, were published by Kalender, Hebele and Ebersberger [25], Glover and Pelc [12], Wei *et al.* [57], Yazdia, Gingras and Beaulieu [61], Yu *et al.* [62], Meyer *et al.* [35], Prell *et al.* [39], Lemmens *et al.* [28, 29] and Bal and Spies [2].

The problem is, interpolated substitution methods reduces streak artifacts accepting a loss of information from the structures surrounding high-density objects. The result is an overall loss of image quality and it can even lead to additional artifacts in the whole image.

An approach to correct these additional artifacts is proposed by Meyer *et al.* [35] and used in Prell *et al.* [39].

Kennedy *et al.* [26] provided an artifact reduction by segmentation of the defective voxels and replacing the wrong information with distinct values. Bal and Spies [2] introduced a method of reducing metal artifacts by interpolating missing information derived from a tissue-class model, which has been extracted from the corrupted image via clustering and adaptive filtering. This approach, which is similar to this work, suppresses metal artifacts without inducing additional artifacts. Very similar to Bal and Spies [2] and the present work is a method published by Lemmens *et al.* [28, 29], which uses a different - iterative - reconstruction method.

A completely different approach is used by Naranjo *et al.* [36], they only modify the reconstruction results, due to an assumption that the raw information is lost during scanning or reconstruction.

In this work, an approach to reduce metal artifacts is presented, acquired with a mobile C-arm CBCT [33, 34]. As a result of the non reproducible projection geometry, caused by unpredictable distortion of the C-arm system during scanning, an realignment process using mutual information must introduced.

Chapter overview

To give a short survey of the present work, a summary of the chapter content is presented.

Chapter 1 contains the theory of the used methods, which are beyond the basics of image processing, and also detailed information about the data acquisition, the reconstruction of cone-beam CT data and the background and origin of the metal artifacts.

The next chapter presents the process of the main field of the thesis. The metal artifact reduction (MAR) is described and the results are discussed. Thereby the advantages and disadvantages of this method are presented and later discussed.

As a part of the MAR, the segmentation is already present in the chapter before. But the presentation of the detailed process of a new projective segmentation is the content of chapter 3. It will be seen, that the new algorithm can fix problems with grave metal artifacts due to large metal objects.

After the discussion in the named chapter, in appendix A a proof of concept, taking place at the beginning of the work, of two dimensional X-ray image stitching which had an effect on the realignment process described in chapter 2.2.3 is explained in a rather short survey.

Appendix B gives a short description of the Hounsfield scale used in CT imaging.

In the content of chapters 2 to 3 and appendix A only the reconstruction algorithm, which was made available from Siemens AG, was present at the beginning of this work.

List of own publications

Patents

- Manuel Meilinger, Christian Schmidgunst

  Verfahren zur Korrektur von Metallartefakten in aus 2D Röntgenbildern reconstruierten Volumendaten.
  (Siemens AG invention disclosure 2008E10971 DE)

  Verfahren zum Erzeugen eines 3D-Bilddatensatzes
  (German patent application 10 2008 050 570 A1)

  Filing Date: 2008-10-06
  Publication Date: 2010-04-15

- Manuel Meilinger, Christian Schmidgunst

  Berechnung, Bewertung und Visualisierung der Bildbereiche im 3D Volumen bei der Bildgebung mittels Cone-Beam CT, die auf Grund von Abschattung durch Metallobjekte mit einem Verlust an Information behaftet sind.
  (Siemens AG invention disclosure 2010E06008 DE)

  Filed together with another invention disclosure by Klaus Engel, Oliver Klar, Markus Kowarschik, Holger Scherl as:
  Verfahren und Vorrichtung zum Bereitstellen von Güteinformation für eine Röntgenbildgebung
  (German patent application 10 2010 034 918.6)

  Filing Date: 2010-08-20
  Publication Date: pending

- Manuel Meilinger, Christian Schmidgunst, Oliver Schütz

  Bewertung und Optimierung der Lagebeziehung zwischen Objekt- und Scangeometrie bei der 3D Bildgebung mittels einen C-Bogen System zur Verbesserung der 3D Bildqualität.
  (Siemens AG invention disclosure 2010E07034 DE)

  Verfahren und Vorrichtung zum Ermitteln des Einflusses von Abschattungen für eine Röntgenbildgebung
  (German patent application 10 2010 034 917.8)

  Filing Date: 2010-08-20
  Publication Date: pending

- Manuel Meilinger, Christian Schmidgunst

  Segmentierung von Metallobjekten in 3D Volumendatensätzen basierend auf Information in den 2D Projektionsbilder und dem rekonstruierten 3D Volumen.
  (Siemens AG invention disclosure 2010E07037 DE)

  Published via priorartdatabase.com:
  http://priorartdatabase.com/IPCOM/000201083#

  Publication Date: 2010-11-08

Articles and conference proceedings

- Manuel Meilinger, Oliver Schütz, Christian Schmidgunst, Elmar W. Lang
  Alignment correction during metal artifact reduction for CBCT using mutual information and edge filtering
  Proc. 6th Int. Symp. Im. Sig. Proc. Anal., 2009. ISPA 2009., pages 135–140. IEEE, 2009
- Manuel Meilinger, Oliver Schütz, Christian Schmidgunst, Elmar W. Lang
  Metal artifact reduction in CBCT using forward projected reconstruction information and mutual information realignment
  World Cong. Med. Phys. Biomed. Eng., September 7 - 12, 2009, Munich, Germany, volume 25/II of IFMBE Proc., pages 46–49. Springer, 2009.
- Manuel Meilinger, Oliver Schütz, Christian Schmidgunst, Elmar W. Lang
  Metal Artifact Reduction in Cone Beam Computed Tomography using Forward Projected Reconstruction Information
  Z. Med. Phys. - accepted 2011-03-08, DOI: 10.1016/j.zemedi.2011.03.002.

Talks

- Manuel Meilinger, Peter Gruber, Christian Schmidgunst, Oliver Schütz, Elmar W. Lang
  Maschinelle Lernverfahren zur adaptiven, anisotropen Rauschreduzierung in 3D - Datensätzen von Röntgentomographen
  Dreiländertagung 2007 (DGMP, ÖGMP und SGSMP), September 25-28, 2007, Bern, Switzerland.
- Manuel Meilinger, Oliver Schütz, Christian Schmidgunst, Elmar W. Lang
  Alignment correction during metal artifact reduction for CBCT using mutual information and edge filtering
  6th International Symposium on Image and Signal Processing and Analysis, ISPA 2009, September 16-18, 2009, Salzburg, Austria.
- Manuel Meilinger, Oliver Schütz, Christian Schmidgunst, Elmar W. Lang
  Metal artifact reduction in CBCT using forward projected reconstruction information and mutual information realignment
  World Congress 2009 Medical Physics and Biomedical Engineering, September 7-12, 2009, Munich, Germany.

Poster

- Manuel Meilinger, Peter Gruber, Christian Schmidgunst, Oliver Schütz, Elmar W. Lang
  Metal Artifact Reduction in Cone Beam Computed Tomography using Reconstructed Date and Mutual Information Realignment
  DPG Frühjahrstagung 2010, March 21-26, 2010, Regensburg, Germany.

1. Theory

In this chapter the mobile C-arm CBCT prototype from Siemens Healthcare, the theory of X-ray cone beam computed tomography, the origin of the metal artifacts as well as a few advanced image processing methods are described. A detailed description of the first topics can be read in the PhD thesis of Christian Schmidgunst[46].

1.1. Mobile C-Arm CBCT device

The mobile CBCT prototype consists of two main components. The main body supplies the X-ray source with energy, contains the control unit and provides the fixing for the second main component, the flat-panel detector (FP).

1.1.1. Basic unit

The basis for the prototype is a Siemens (Erlangen, Germany) 'Powermobil' module (fig. 1.1), which can supply the X-ray tube with the necessary power (peak is about 20 kW) to sustain a pulsed radiation with 100 kV tube voltage and a pulse width of 7 ms. The original products using the 'Powermobil' posses as detector an image intensifier and are able to make only 2D images.

The basic unit holds a isocentric C-arm with a diameter of approximately 130 cm and a tube-detector distance of about 120 cm. In comparison to the production model, this prototype is modified to be able to make an automated orbital movement (with about 180 degrees) for 3D scanning.

To move the device manually it is necessary that the whole C-arm is built from carbon fibers to reduce the weight without decreasing the stability. But due to the weights of the tube and the detector, and the need of different counterweights, it is not stable enough to perform an orbital rotation without distortion, both predictable and unpredictable. Though the incalculable deformation is low, it is not negligible.

Figure 1.1.: 3D soft-tissue-imaging prototype.
Source: Siemens Healthcare

Because of that, a realignment algorithm (cp. chap. 2.2.3) is needed to perform a metal artifact reduction (MAR) for mobile devices.

The X-ray tube can provide a radiation from 40 kV to 125 kV tube voltage with a tube current from 0.2 mA to 6.7 mA for about 12.5 pictures per second.

1.1.2. Flat-panel detector

As written above, in contrary to the original production model the prototype carries a plat-panel detector (FP). Different FPs (detector size 40 cm×40 cm and also 30 cm×30 cm) were used during the project.

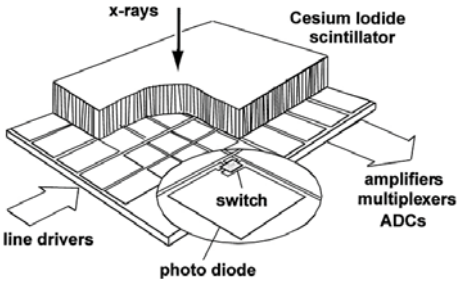

Figure 1.2.: Schematic drawing of a flat-panel X-ray detector unit showing the amorphous silicon pixel matrix covered by a cesium iodide scintillation layer.
Source: Strotzer [51]

The used detectors were indirect FD's. The X-ray photons hit a CsI(Tl) scintillator and their energy was converted to emit visible photons via several steps and by the use of electron-hole pair production and recombination. These photons were detected using photodiodes of amorphous silicon (a-Si:H) driven by a TFT layer [45, 46].

Figure 1.3.: Varian flat-panel detector.

Flat panel detectors have several advantages during a 3D scan compared to image intensifiers (IT).

- ITs are affected by the earth magnetic field, in the best case the detector is calibrated after every change in position.
- FDs have an almost linear signal response.
- The dynamic range of a IT is considerable smaller than that of a FD.
- Because of the better signal conversion of a FD, the cumulative dose during a 3D scan is clearly smaller than that of a IT.
- FD gets distortion-free reproductions of the image information.

Different corrections must be applied to the raw data to gain a usable 2D image for reconstruction. A detailed description and application is available in publications by Schmidgunst and Maschauer [31, 45–48]. Here as short survey of these correction is presented.

Offset correction

Due to structural differences between the parts of the FD, each pixel can have a different offset value, without X-ray radiation from the source (dark frame). To correct these values the device is acquiring dark frame images for different temperatures and computes offset maps.

Delta correction

The second step is to account for the change in sensitivity for each pixel because of the long term C-arm distortion or aging. For this a white field (with active X-ray tube) series is made during an orbital rotation. With the use of the offset map a delta-map is created.

Temperature correction

Because of the mobile design an active cooling system for detector or tube is not practicable due to the weight. With a nominal power consumption of 50 W and the external X-ray shields, this can lead to a temperature of about 50 °C. In consideration of the application of the mobile device, a temperature range from about 15 °C to 50 °C is possible. To correct this, several offset and gain-maps for various temperatures are collected. The ratio between an offset (respectively a gain) map for temperature t and t_E (t_E is the end temperature after warm-up, with $t < t_E$) is stored as temperature map.

Multi point gain correction

The recorded images with active X-ray (white frame) source had to be plain white. Based on the Heel effect and the spherical propagation a correction is needed. Comparable to the offset correction a gain map is generated using several white frame images. In fact, for each dose setting (tube voltage constant, tube current variable) a gain map has to be created. To accommodate for this problem, several gain maps along the dose dynamic range are computed. The necessary gain map for an individual dose setting is then interpolated.

DGR combination

The FDs used in the CT are able to utilize a dual gain readout mode (DGR) which supports two different sensitivities for two adjacent lines. This enables

the FD to cover a greater dynamic range. In the DGR combination the so called high gain and low gain images, belonging to the higher, respectively lower, sensitivity, are combined. Because this combination is computed after the previous corrections it is possible to use the different global mean values of the appropriate gain maps.

Defect pixel correction

Due to several causes single pixels or wholes lines or columns of pixels in the FD can be defective from the beginning or get faulty during the use or storing. A defect pixel map contains all information about these pixels. As long as at least 4 of the 9 pixels in a 3×3 neighborhood are valid, a defective pixel is interpolated using the median of its neighbors.

Lag correction

Indirect FDs suffer from image lag effects, due to charge trapping and release in the detector pixels. These effects result in so-called 'comet' and 'streak' artifacts in CBCT [49, 50]. With the information of pictures taken shortly before, these lag effects can be estimated and corrected.

1.2. Cone-beam computed tomography

Like in conventional CT, cone-beam computed tomography (CBCT) uses projection data to reconstruct cross-sections of the scanned object. As further development of CT, CBCT did not use one-dimensional line scans to reconstruct two-dimensional cross-sections, but two-dimensional images to reconstruct a three-dimensional volume.

1.2.1. Image acquisition

The whole process of image acquisition for a series of two-dimensional X-ray fluoroscopy images is shown in figure 1.5. After the mobile device is positioned at the table with perpendicular C-arm, locating the area of interest in the isocenter (the radiation isocenter is the point in space through which all the central beams of radiation passes), the arm takes up its initial position. This is necessary to operate the time triggered X-ray system as reproducible as

possible to enhance the spatial resolution. The scan consists of 100 to 400 images, taken with a constant imaging rate, over the angular range of 180 degrees plus cone angle. This additional angle is inevitable to acquire the required information, from at least 180 degrees, for all points inside the total reconstruction volume, due to the conical form of the X-ray beam (cp. chap. 1.2.4). After the recording, the device moves back to its upright starting position and can be used for additional two-dimension imaging or can be carted away.

1.2.2. Reconstruction

The reconstruction of projected information has been mathematically solved and published by Radon in 1917 [40], but different approaches of the data acquisition (some of them violate assumptions made by Radon) implicate different solutions and implementations.

For CBCT the filtered back projection (FBP, see [3, 41]), in use for two-dimensional reconstruction, was adapted by Feldkamp, Davis and Kress [10] for CBCT reconstruction (FDK). A short survey of the FBP, FDK and other methods can be read in Turbell [55].

In the research published in this thesis, the following adapted version of the FDK was used.

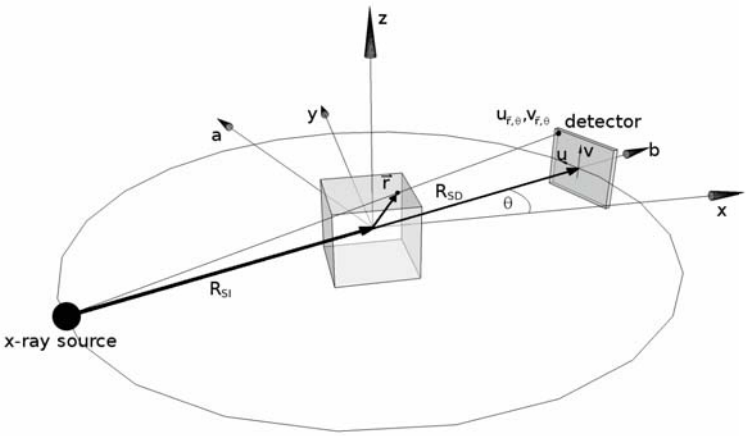

Figure 1.4.: Geometry of CBCT projection with a planar detector

Step 1: The C-arm is positioned perpendicularly at the table, locating the area of interest in the isocenter.

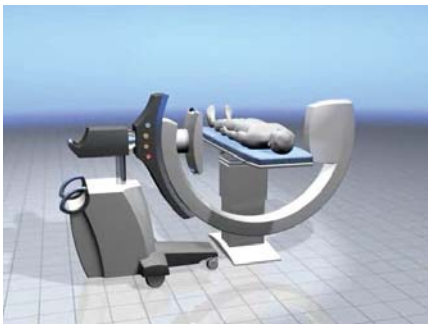

Step 2: The arm takes up its initial position.

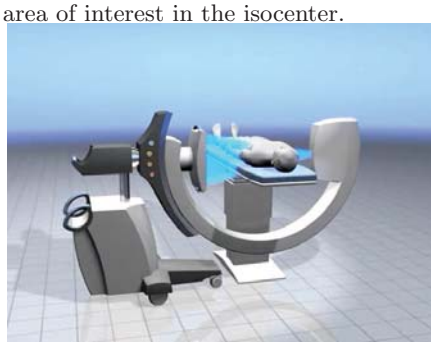

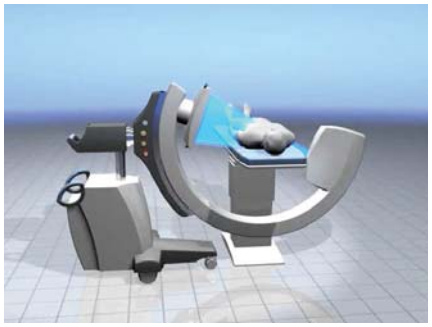

Step 3: During a complete orbital rotation (180 degrees plus cone angle) 100 to 400 evenly distributed images are taking.

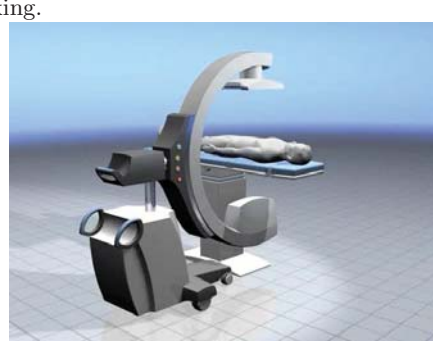

Step 4: After the scan the C-arm takes up perpendicular position again, after that the device can be removed or further scans processed.

Figure 1.5.: Process flow of mobile C-arm CBCT volume scan
Source: Siemens Healthcare - Internal report 2004

In FDK a voxel in the reconstructed volume $\mu_{FDK}(\mathbf{r})$ is computed as follows (see fig. 1.4):

$$\mu_p(\mathbf{r}) = \int_0^{2\pi} \frac{R_{SI}R_{SD}}{U(x,y,\theta)^2} p^F\left(u_{\mathbf{r},\theta}, v_{\mathbf{r},\theta}, \theta\right) \mathrm{d}\theta \tag{1.1}$$

Here $\mathbf{r}$ is the vector in the volume pointing at voxel x, y, z. $u_{\mathbf{r},\theta}$ (respectively $v_{\mathbf{r},\theta}$) is the corresponding pixel coordinate on the detector which is hit by an X-ray beam through voxel $\mathbf{r}$ in angular position θ. The point of origin of x, y, z is the isocenter, the point of origin of u, v is the center of the FD.

R_{SI} is the distance from the X-ray source to the isocenter, R_{SD} the distance from the source to the detector and

$$U(x,y,\theta) = R_{SI} + x\cos\theta + y\sin\theta \tag{1.2}$$

is a distance weighting term.

$p^F(u,v,\theta)$ is the filtered pixel value $p(u,v,\theta)$ at the coordinates u and v on the detector in angular position θ, this value can be derived from the acquired intensity value $I(u,v,\theta)$ using the natural logarithm and the intensity without attenuation I_0. It is given by:

$$p^F(u,v,\theta) = \left(\frac{R_{SD}}{\sqrt{R_{SD}^2+u^2+v^2}} p(u,v,\theta)\right) * h(u) \tag{1.3}$$

$$p(u,v,\theta) = -\ln\left[\frac{I(u,v,\theta)}{I_0}\right] \tag{1.4}$$

Here the term $\frac{R_{SD}}{\sqrt{R_{SD}^2+u^2+v^2}}$ is a pre-weighting, dependent on the cone-angle and fan-angle [10, 55].

$h(u)$ is the filter function which is convoluted on the image lines. This filter function arises during a change of variables between spherical coordinates and Cartesian coordinates in derivation of the FDK.

Actually according to the derivation, this filter should be a ramp-filter (often denoted as Ram-Lak Filter because of Ramachandran and Lakshminarayanan [41]) in frequency space, but due to various problems occurring in real measurements like noise and digitalization, high frequencies must be diluted, not amplified. As consequence a mixture between a ramp-filter and a low-

pass is used, like a Shepp-Logan or Hann (often denoted as Hanning) filter (cp. fig. 1.6).

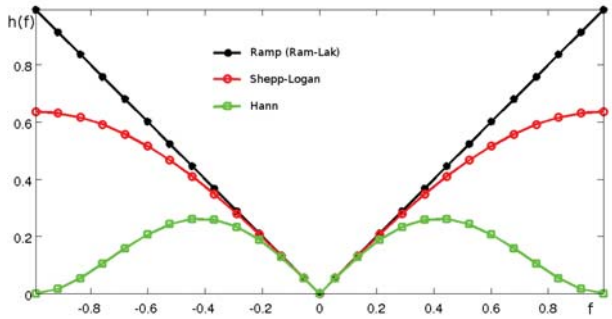

Figure 1.6.: Comparison between usual FBP filter in frequency space (black (asterisk): ramp (also Ram-Lak), red (circle): Shepp-Logan, green (box) Hann)

As mentioned the FDK describes a reconstruction for circular CBCT. Also referred to before, the C-arm distorts (cp. chap. 1.1.1) during a scan, and therefore violates this assumption. This violation must be corrected as well as the incomplete scanning (with fewer than 360 degrees, cp. chap. 1.2.4) and the hence resulting overvaluation of certain projection lines (called Parker correction [8, 38]).

Another consequence of this distortion is, that the dependance between v,u and $\mathbf{r}$,θ must be calibrated for each device in regular intervals (cp. [46]).

As another result of the FDK the middle slice (with $z = 0$) is the only one that can be reconstructed accurately. The computation of this slice is identical to a fan-beam reconstruction which is a special case of the FDK.

1.2.3. Forward projection

Several parts of the algorithm need forward projections from modified or simulated volume data to work in the 2D series with this information. A forward projection is a simulation of a radiography process. To get the 2D data, the integral of the X-ray attenuation coefficients along the cone beam path must be computed for each pixel.

The calculation can be pixel- or voxel-driven. Following the pixel-driven forward projection is described and used.

Pixel-driven (also ray-driven or pixel-based) means, that for each pixel in the two dimensional space the ray path along the projection is calculated ($l_{(u,v)_\xi}$) and then the integral in the volume is made. Because of the discrete voxel positions in the volume the integral is replaced by a sum, but different steps along the ray can be used (cp. [55]).

In this work, the so called 'simple method' (cp. [55]) is used: every fixed step size on the ray path, the trilinear interpolation of the involved voxels is calculated and summed.

The result is an image whose values are the integral over all available attenuation coefficients along the used ray:

$$I_{fp}(u,v)_\xi = \int\limits_{l_{(u,v)_\xi}} I(\mathbf{r})\mathrm{d}\mathbf{r} \tag{1.5}$$

where $I(\mathbf{r})$ is an arbitrary volume and $l_{(u,v)_\xi}$ is the ray path through I hitting the image $I_{fp}(u,v)_\xi$ with number ξ at position (u,v).

1.2.4. Field of view (FOV)

In fig. 1.7 it can be seen why it is necessary to scan an object over 180 degrees plus cone angle. In this sketch a cone angle of 15 degrees is used. In the top images the focus lies on point P1, to get information for this point from 180 degrees, a scan from zero degrees (top left) to 165 degrees (top right) is sufficient. But focussed on P2 it is clear why the last shot must be at position 195 degrees (cp. [8, 32, 38]).

The points P1 and P2 define the field of view (FOV), the area in which all the points lie for which enough information (scan angle greater or equal 180 degrees) is acquired. In publications, it is sometimes denoted as field of measurement (FOM).

The case of a CBCT is identical to the fan beam CT in matters of the scan angle, but differs in the matter of the FOV, due to the rectangular detector in the cone X-ray beam. The field of view is shaped like a cylinder with a flat cone on top and on bottom (cp. fig. 1.8).

To make the visualization easier, a cube which encompasses most or all of the FOV (cp. fig.1.9) is reconstructed and used to display.

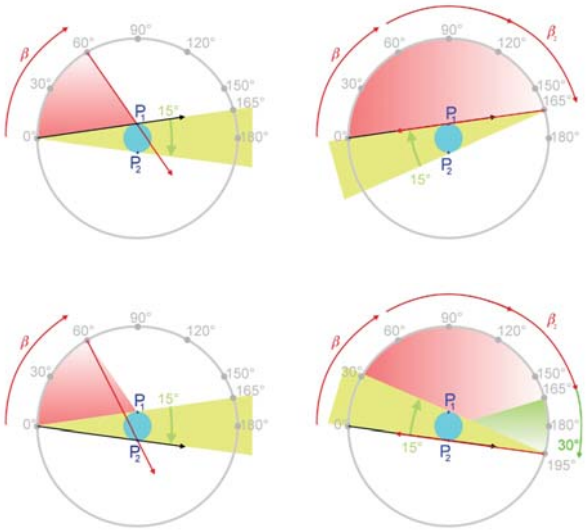

Figure 1.7.: A complete CT scan process over 180 degrees plus cone angle is shown in this figure, where it can be seen why the additional angle is necessary. Also the FOV (cyan circle) is presented.

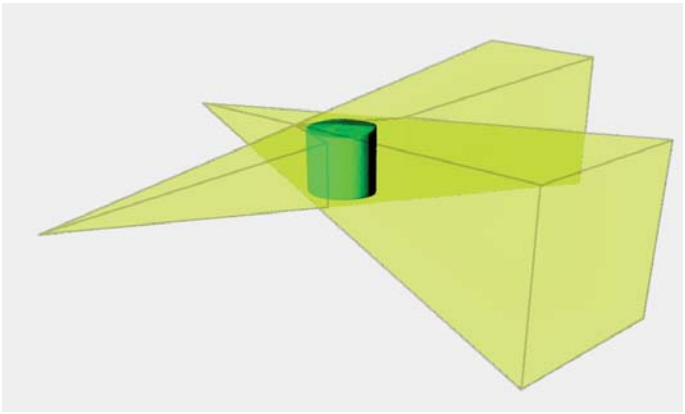

Figure 1.8.: Here the FOV of a CBCT is presented (green), for illustration two cone beams (delimited to the detected area, yellow) are also shown.

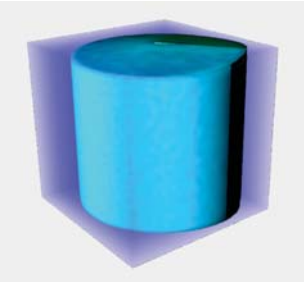

Figure 1.9.: The reconstructed cube (blue) around the FOV (cyan).

It is important to consider, that every information outside the FOV cannot be reconstructed completely and therefore also the forward projection of these voxels is not as good as inside the FOV. Every object outside the reconstruction cube is not reconstructed and therefore is completely missing in any forward projection (cp. chap. 2.2.4).

1.3. Metal artifacts

High density objects like metal implants lead to severe shadow and streak artifacts during CT imaging, in this section the origin and the properties of metal artifacts will be described.

Artifacts arisen of nonlinear polychromatic X-ray sources in CT are described since the end of the 1970's (e.g. by Duerinckx and Macovski [9]), a good overview of the main causes, including simulation studies, is given in an article of De Man *et al.*[7].

1.3.1. Beam Hardening

The main problem in X-ray CT is the lack of a mobile monochromatic X-ray source. Instead of that, polychromatic sources, a combination of bremsstrahlung and X-ray fluorescence, must be used. The attenuation of X-rays through homogenous matter with an constant attenuation (not depending on the energy) with distance r is described by the Beer-Lambert law given by:

$$I(r) = I_0 \exp(-\mu r) \tag{1.6}$$

Where I_0 is the intensity at $r = 0$ and μ is the attenuation coefficient. Often the mass attenuation coefficient μ_m is used, it holds $\mu_m = \frac{\mu}{\rho}$ where ρ is the density of the matter.

For non-homogenous objects with regarding that μ depends on the energy of the radiation (E), a more general form of the Beer-Lambert law must be used ($E_{max} = e \cdot U$ is the maximum energy available in the radiation, given by the tube voltage U and the elementary charge e):

$$I(r) = \int_0^{E_{max}} \left[I_0(E) \exp\left(- \int_0^r \mu(r, E) \mathrm{d}r \right) \mathrm{d}E \right] \tag{1.7}$$

In the following, two different kinds of matter are regarded. First, we regard water (H_2O) as a first approximation for tissue. The attenuation coefficient of water in the interval from 1 keV to 150 keV is shown in figure 1.10. The three main effects are coherent and incoherent scattering plus photoelectric absorption. It can be seen, that the attenuation differs about 1.5 decades in this range.

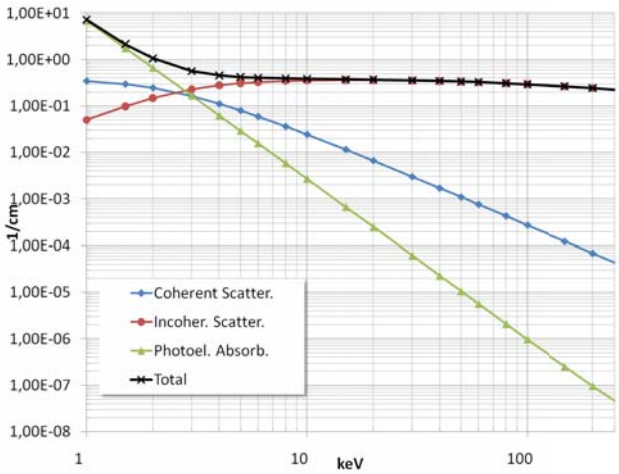

Figure 1.10.: The attenuation coefficient of water.

The next figure (fig. 1.11) displays the same illustration for iron (Fe) as estimation for metal implants. It can be seen that the attenuation differs about 5 decades in the same range and has a step at about 7.11 keV. Figure 1.12 shows a direct comparison of these two curves.

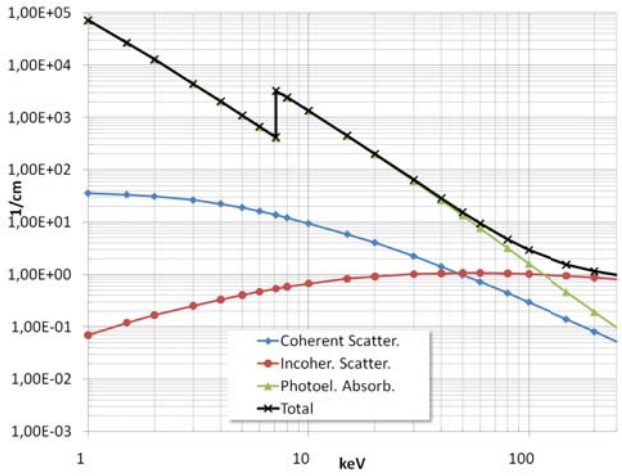

Figure 1.11.: The attenuation coefficient of iron.

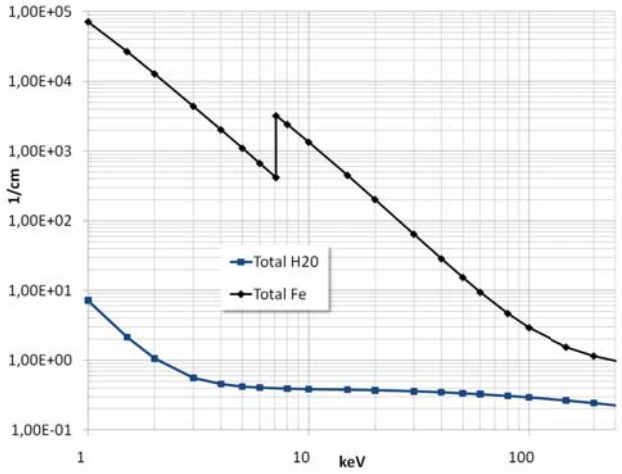

Figure 1.12.: A comparison of the wavelength dependency of the attenuation of water and iron.

To see the effect of these different attenuation spectra an absorption simulation is presented. To simplify the diagrams (w.l.o.g.) only bremsstrahlung is used. The simulation uses the approximation for X-ray spectra from Kulenkampff [27] $I_\lambda \propto \frac{\lambda-\lambda_0}{\lambda^3 \cdot \lambda_0}$, where λ_0 is the cutoff wavelength for the given tube

voltage U, it holds $\lambda_0 = \frac{h \cdot c}{e \cdot U}$, with h the planck constant, c the speed of light and e the elementary charge (cp. [27, 30, 42]). The intensity of the spectrum depends on the tube current and the anode material. For the simulation the exact values are not required, thus for the following the spectra are normalized to a maximum of 1 arbitrary unit (a.u.).

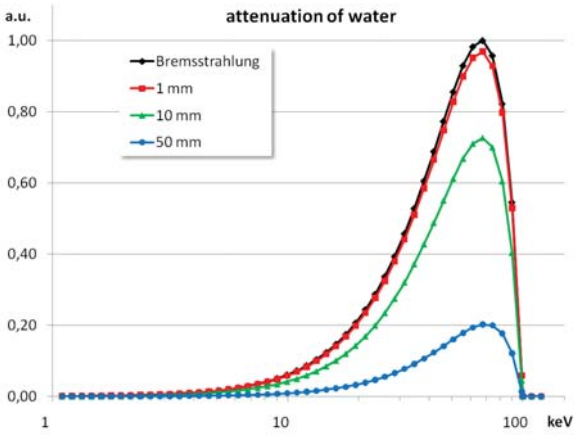

Figure 1.13.: In this figure bremsstrahlung spectra of a 100keV X-ray source without and with absorption in water are shown.

In figures 1.13 and 1.14 two spectra of an X-ray source with a tube voltage of 100 keV are shown. The black lines represent the normalized distribution, the red (respectively green or blue) lines represent the distribution after a passage of 1 mm (respectively 10 mm or 50 mm) of water or after a passage of 0.1 mm (respectively 1 mm or 5 mm) of iron.

At first sight, it can be seen, that in the case of water the attenuation decreases the intensity equally, while the attenuation of iron is more one-sided.

In fig. 1.15 the difference between the attenuation of water and iron is illustrated. On the ordinate the relative intensity with $I(0) = 1$ is shown in a logarithmic scale, while on the abscissa the relative thickness of the reducing mass from zero to the half-life width is plotted.

To compare the dependencies with the ideal case, a linear attenuation is presented as well. It can easily be seen, that the first sight was correct, the reducing due to the presence of iron is explicitly non-linear. On the other side the attenuation of water differs not much from the perfect case.

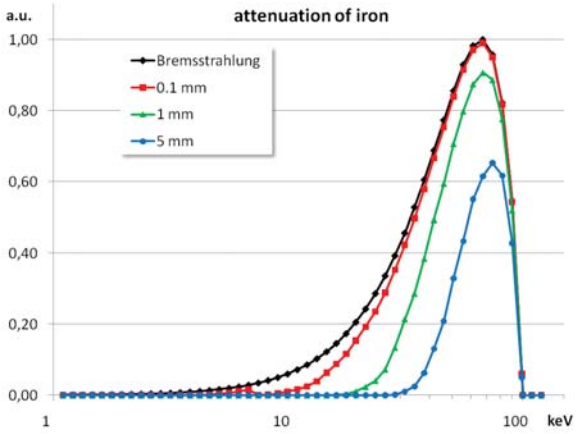

Figure 1.14.: In this figure bremsstrahlung spectra of a 100keV X-ray source without and with absorption in iron are shown.

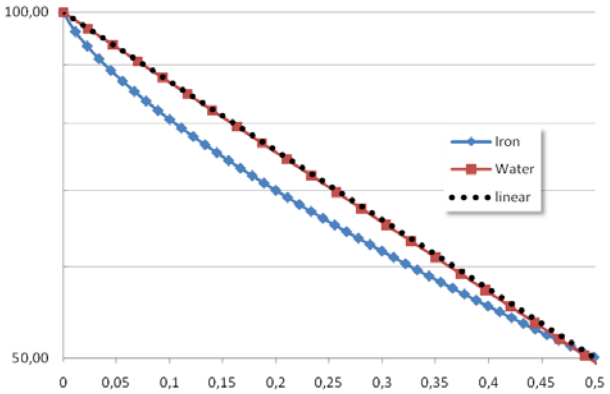

Figure 1.15.: This figure shows the differences in the dependance of the attenuation from the thickness of the attenuating mass. While the reduction by water is nearly linear, the reduction by iron is clearly non-linear. On the ordinate the relative intensity is shown in a logarithmic percent scale, while on the abscissa the relative thickness of the reducing mass from zero to the half-life width is plotted.

This non-linear effect, which increases the measured intensity and therefore leads to an undervaluing of the hardness of the object, results in dark streaks, which lie in the direction of highest attenuation or connect objects (cp. [4, 7]).

1.3.2. Scatter

Another effect is arising from the scattering of the X-ray photons. As can be seen above (cp. fig. 1.10 and fig. 1.11) two of the three main attenuating effects are coherent and incoherent scattering.

The scattered photons can hit the detector at other positions than the direct beam, so additional to the primary intensity (I_P), which is the reduced intensity of the direct beams, a scattered intensity (I_S) occurs. Corrections of this also non-linear effect are often implemented in the reconstruction algorithms. But the scatter artifacts increase if high attenuation material, like metal implants, is present in the scanned object.

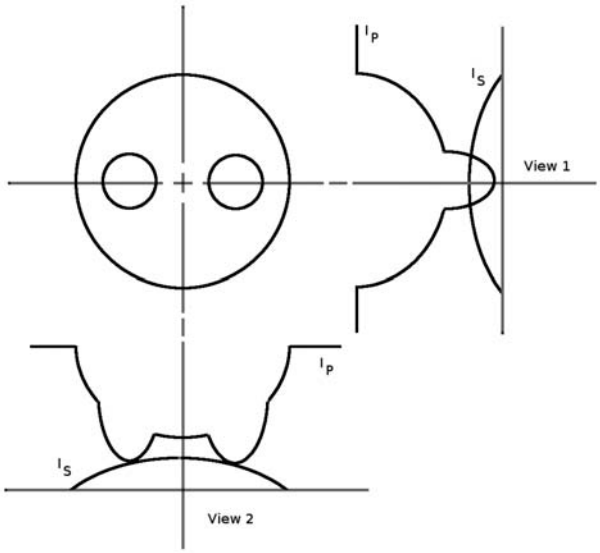

Figure 1.16.: In this image the primary and scattered intensities for two orthogonal angles are shown (cp. [11]).

In fig. 1.16 a water cylinder with two smaller cylindrical metal objects is shown, aside and below the primary and scattered intensity is plotted. It can be seen, that the significance of scattered photons is higher if a lot of regions with metal objects (view 1) lie between the X-ray tube and the detector, because I_S reaches the same order of magnitude as I_P. The result of this non-linear influence is a decrease of the measured intensity (cp. chap. 1.3.1) and therefore leads to the same artifacts as beam hardening (cp. [7, 11, 20]).

1.3.3. Exponential Edge-Gradient Effect

Because of the finite dimension of the source and detector elements, each pixel gets the integral of an area of X-ray beams after the reduction of the scanned material. For a given Line L (cp. fig. 1.17) from source to detector the attenuation factor is defined as:

$$F_A = \exp\left(-P_A\right) = \exp\left(-\int_L \mu(x,y)\mathrm{d}l\right) \tag{1.8}$$

where $P_A = \int_L \mu(x,y)\mathrm{d}l$ is the projection of the attenuation coefficient $\mu(x,y)$ at position (x,y) and dl is the differential of length along the line L.

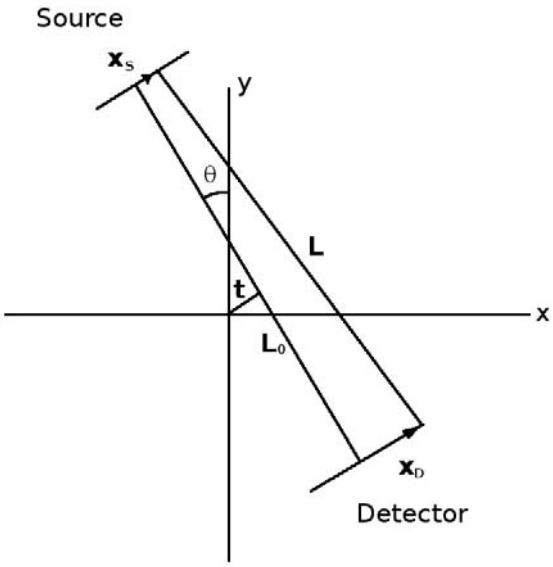

Figure 1.17.: Geometry of a finite-width projection, where t is the impact parameter and θ the view angle. The projection line L starts at position $\mathbf{x}_S$ on the source and ends on position $\mathbf{x}_D$ on the detector. The vector $\mathbf{x}_D$ is constrained to lie in one pixel of the detector, the vector $\mathbf{x}_S$ is constrained to all starting positions that lead to an ending position in that detector pixel (cp. [22]).

To compute the measured signal of a finite width of the source $\mathbf{x}_S$ and the detector $\mathbf{x}_D$ with an unreduced intensity of I_0 and two normalized source $\left(\int S(\mathbf{x}_S)\mathrm{d}\mathbf{x}_S = 1\right)$ and detector $\left(\int D(\mathbf{x}_D)\mathrm{d}\mathbf{x}_D = 1\right)$ functions an average over the vectors $\mathbf{x}_S$ and $\mathbf{x}_D$ is needed:

$$I(t,\theta) = I_0 \int S(\mathbf{x}_S) \int D(\mathbf{x}_D) \exp(-P_A(t,\theta,\mathbf{x}_S,\mathbf{x}_D))\mathrm{d}\mathbf{x}_D\mathrm{d}\mathbf{x}_S \tag{1.9}$$

W.l.o.g the EEGE appears in parallel beam geometry, too. It also occurs when the source and detector functions are constant over $\mathbf{x}_S$ or respectively $\mathbf{x}_D$, then the following simplified equation can be used:

$$I(t,\theta) = I_0 \iint \exp\left(-\int_{L(t,\theta,\mathbf{x}_S,\mathbf{x}_D)} \mu(x,y)\mathrm{d}l\right) \mathrm{d}\mathbf{x}_D\mathrm{d}\mathbf{x}_S \tag{1.10}$$

Looking at figure 1.18 two beams are shown. The amount of material blue and green is the same in both beams, only the configuration differs.

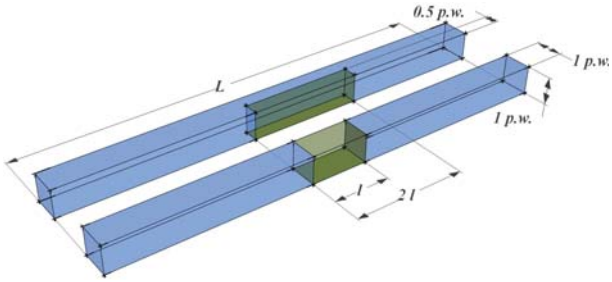

Figure 1.18.: Two parallel beams (length L) from source (left side) to detector (right side) with a pixel dimension of $1p.w.^2$ (**p**ixel **w**idth). The ratio between material 1 (blue) and material 2 (green) in both beams is identical, but in the upper beam (beam B1), in contrary to the lower beam (beam B2), a hard edge along the beam is present.

With attenuation coefficients of α for the blue and β for the green region the primary intensities of the two beams are:

$$I_{B1} = \frac{1}{2} I_0 \left[\exp\left(-L\alpha\right) + \exp\left(-\{L-2l\}\alpha - 2l\beta\right)\right] \tag{1.11}$$

$$I_{B2} = I_0 \left[\exp\left(-\left\{L-l\right\}\alpha - l\beta\right)\right] \tag{1.12}$$

It can easily be seen that this difference violates the assumption, that the so called 'raw-data' (or pixel value cp. $p(l,\theta) = p(u_l, v_l, \theta)$ in chap. 1.2.2)

$$p(t,\theta) = -\ln\left[\frac{I(t,\theta)}{I_0}\right] \tag{1.13}$$

can be related to a spatial average (S_P) of P_A:

$$p(t,\theta) \approx S_P(t,\theta) \tag{1.14}$$

with

$$S_P(t,\theta) = \iint P_A(t,\theta,\mathbf{x}_S,\mathbf{x}_D)\mathrm{d}\mathbf{x}_D\mathrm{d}\mathbf{x}_S \tag{1.15}$$

Because of that violation artifacts are created, due to their origin called Exponential Edge-Gradient Effect (EEGE).

The difference $E = p - S_P$ is depending on the difference between α and β. But it can be shown, that E is always negative [22].

Simulations reveal, that the artifacts, produced by the EEGE, are both dark and bright streaks protruding from the edges of the high contrast objects, like metal implants, only depending on the configuration [7, 22].

1.3.4. Noise

Duerinckx and Macovski [9] show that the noise variance and cross-correlation of a reconstructed CT image (in this calculation w.l.o.g. an one slice CT device is used) with a monochromatic X-ray beam is:

$$\sigma^2(\mathbf{r}) = \frac{1}{\pi n_0} B\left\{\exp\left(\overline{P}_A(t,\theta)\right) * h^2(t)\right\} \tag{1.16}$$

$$R(\mathbf{r}_1,\mathbf{r}_2) = \frac{1}{\pi n_0}\iint \exp\left(\overline{P}_A(t,\theta)\right) h\left([\mathbf{r}_1 - \mathbf{t}]\cdot\mathbf{u}_t\right) \times h\left([\mathbf{r}_2 - \mathbf{t}]\cdot\mathbf{u}_t\right)\mathrm{d}\mathbf{t} \tag{1.17}$$

with the notation:

$$\iint \mathrm{d}\mathbf{t} = \frac{1}{\pi}\int_0^{\pi}\int_{-\infty}^{\infty}\mathrm{d}\theta\mathrm{d}t$$

where t is the distance from the center line (also named impact parameter cp. fig. 1.17) and $\mathbf{r}$, $\mathbf{r}_1$ and $\mathbf{r}_2$ are points on the reconstructed image, n_0 is the total count of unattenuated photons with no absorbing material in the CT, $B\{a * b\}$ is the filtered back projection (cp. chap. 1.2.2) of signal a convoluted with the filter b. $\overline{P}_A(t,\theta)$ is the expectation of $P_A(t,\theta)$ (cp. chap. 1.3.3), $h(t)$ is the filter kernel (cp. chap. 1.2.2) and $\mathbf{u}_t$ is the unit vector along $\mathbf{t}$.

Eq. (1.16) shows various differences to the normal reconstructed data:

$$\mu \sim B\left\{\overline{P}_A(t,\theta) * h^2(t)\right\}$$

One difference is, that a non linear function (exp) is introduced, which explains the increased noise in the center of a reconstructed cylinder. This artifact can be compared to cupping artifacts because of polychromatic X-ray beams. Simply put, fewer photons are transmitted through the center of a cylinder which increases the noise.

More important for the arise of metal artifacts is eq. (1.17). Where an anisotropy can be seen, if the geometrical interpretation of the equation, for $|\mathbf{r}_1 - \mathbf{r}_2| \gg w$ with w is the full width at half maximum of the point spread function of the reconstruction algorithm (for more details see [1, 9, 43]), is looked at. This anisotropy and the dependence of $\sigma^2(\mathbf{r})$ from $\exp\left(\overline{P}_A(t,\theta)\right)$ leads to streak artifacts (both dark and bright) around objects with high attenuation (cp. [1, 7, 9, 43]).

1.3.5. Motion and Aliasing

Another problem that can cause streak artifacts is motion of the scanned object during the scan.

It can easily be seen that motion of a sharp edge during the scan causes streak artifacts along the projection lines of the misaligned images during an FDK reconstruction, because each recorded image (or line) is convoluted with the filter and then projected over the whole reconstruction volume (or image).

After the filtering (the filter is either a high pass (ram-lak) or a middle pass (combination of low and high pass) filter cp. chap. 1.2.2) intense edges remain as high signals, because of their broad frequency spectrum. This signal results in an intense line in the reconstructed data. During the reconstruction process the different angles correct these lines to the original object, only if the edge is always in the right place within the reconstructed image. Due to the motion, each moved edge introduce a line which cannot be corrected with the other angles. These lines remain as streak artifacts (cp. [7, 12]).

Another similar effect comes from 'detector or view under-sampling'.

In case of 'detector under-sampling' Joseph, Spital and Stockham [23] show that the relationship between the Fourier transform (FT) of the detected discrete sampled data (denoted as $\hat{Q}_\theta(\omega)$) and the Fourier transform of the real data $\hat{p}_\theta(\omega) = FT\{p(t,\theta)\}$ is:

$$\hat{Q}_\theta(\omega) = \sum_{m=-\infty}^{\infty} \hat{p}_\theta(\omega + 2\pi m/d) \tag{1.18}$$

with $m = [0, \pm 1, \pm 2, \ldots]$ and d as sampling distance. It can be seen clearly, that components of $\hat{p}_\theta$ with frequencies above the Nyquist frequency ($\omega_N = \pi/d$) contribute as aliasing frequencies below ω_N of $\hat{Q}_\theta$.

In the case of 'view under-sampling' the scan persists of too few angles. Joseph and Schulz [21] specify a minimum number of views N_{min} which are necessary to reconstruct the data without additional streak artifacts from view under-sampling.

These aliasing artifacts can be ignored if an adequate detector and scanning geometry is used. Therefore this work did not detail this effects (see [7, 21, 23]).

Neither the artifacts of motion nor those of aliasing are limited to metal objects, but high-attenuating parts in the field of view (FOV) increase their strength.

1.4. Image Processing

In this section a few advanced image processing techniques are described which are used during the MAR or segmentation process (compare the following chapters). Basic methods and algorithms like Gaussian filtering, edge detection or similar can be found in several image processing textbooks like 'Digital Image Processing' [13, 14], a German equivalent 'Digitale Bildverarbeitung' [18] or others.

1.4.1. Bilateral Filter

A simple nonlinear advancement of a Gaussian filter is the Gaussian case of the bilateral filter, which is a combination of a domain filter and a range filter (denoted according to Tomasi and Manduchi [54]).

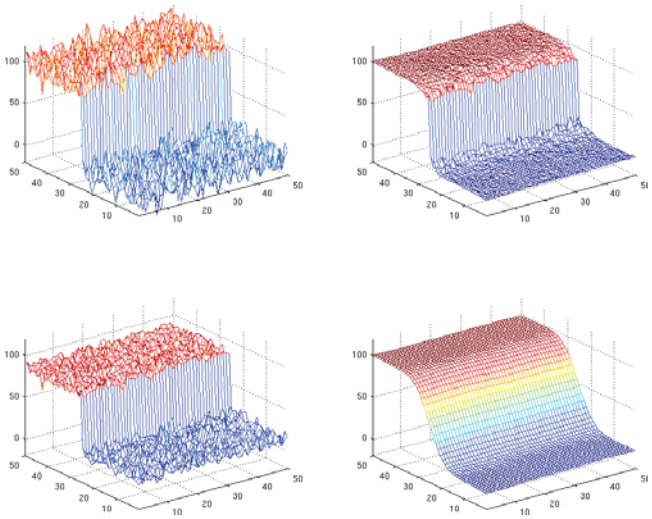

Figure 1.19.: A 100-gray-level step with a Gaussian noise with $\sigma = 10$ gray levels is shown in the upper left corner. In the upper right corner a bilateral filter with $\sigma_D = 5$ pixels and $\sigma_R = 50$ gray levels is applied. To compare the combination with a pure range filter with $\sigma_R = 50$ gray levels and a pure domain filter with $\sigma_D = 5$ pixels the results of these filter are shown in the lower left (range filter) and lower right (domain filter) corner.

The domain filter in this case is a Gaussian filter depending on the Euclidean distance between two pixels defined as follows:

$$I_{FD}(\mathbf{x}) = \frac{1}{\sigma_D\sqrt{2\pi}} \int I(\mathbf{t}) \exp\left[-\frac{1}{2}\left(\frac{||\mathbf{t}-\mathbf{x}||}{\sigma_D}\right)^2\right] \mathrm{d}\mathbf{t} \tag{1.19}$$

where $I(\mathbf{x})$ is the image and $I_{FD}(\mathbf{x})$ the domain filtered image at the point $\mathbf{x}$ and σ_D is the standard deviation.

Analog, the range filter is depending on the similarity of the value between two pixels defined as follows:

$$I_{FR}(\mathbf{x}) = \frac{1}{\sigma_R\sqrt{2\pi}} \int I(\mathbf{t}) \exp\left[-\frac{1}{2}\left(\frac{||I(\mathbf{t})-I(\mathbf{x})||}{\sigma_R}\right)^2\right] \mathrm{d}\mathbf{t} \tag{1.20}$$

The combination of these two filters can be easily obtained by:

$$I_F(\mathbf{x}) = \frac{1}{N} \int I(\mathbf{t}) \exp\left\{ -\frac{1}{2} \left[\left(\frac{||\mathbf{t}-\mathbf{x}||}{\sigma_D} \right)^2 + \left(\frac{||I(\mathbf{t})-I(\mathbf{x})||}{\sigma_R} \right)^2 \right] \right\} \mathrm{d}\mathbf{t} \tag{1.21}$$

where the factor N takes care of the normalization and is defined as follows:

$$N = \int \exp\left\{ -\frac{1}{2} \left[\left(\frac{||\mathbf{t}-\mathbf{x}||}{\sigma_D} \right)^2 + \left(\frac{||I(\mathbf{t})-I(\mathbf{x})||}{\sigma_R} \right)^2 \right] \right\} \mathrm{d}\mathbf{t} \tag{1.22}$$

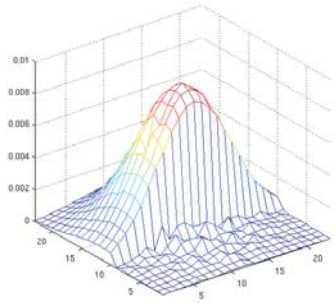

Figure 1.20.: Filter kernel of the bilateral filter, centered two pixels to the left of the step shown in fig. 1.19.

It can clearly be seen, that the bilateral filter is nonlinear, because the weights depend on the image value, non-iterative and a simple enhancement of a Gaussian blurring.

It combines the advantage of a simple smoothing algorithm from the domain filter and the edge preserving habit of the range filter.

In fig. 1.19 an application of a bilateral filter is shown. To show the benefit in comparison to the usage of only a domain or range filter the results are plotted also. The figures shows that a solo used range filter alters the step size (the step difference decreased notably) and distorts the whole image, while a domain filter alone flattens the edge as expected.

The filter kernel itself centered two pixels away from the middle of the step to the left is shown in figure 1.20. Here it can be seen, that the range part concentrates the domain filter on the appropriate side of the step. The filter kernel centered two pixels to the right looks similar but mirrored at the edge.

The described algorithm can be used without iteration. Only the range filter and the normalization must be computed for each pixel. As a result, the bilateral filter is a fast edge-preserving filter which can easily be implemented as a preprocessing step to various image processing.

1.4.2. Mutual Information

For realignment and image registration it is necessary to obtain a criterion of similarity. A possible criterion for this is mutual information (MI).

MI is a quantity that measures the mutual dependence of two random variables, defined by one of the following equations:

$$I(X;Y) = H(X) - H(X|Y) \tag{1.23}$$

$$I(X;Y) = \sum_i \sum_j p(x_i, y_j) \log \frac{p(x_i|y_j)}{p(x_i)} \tag{1.24}$$

where $I(X;Y)$ is the MI and $H(X)$ the entropy (respectively $H(X|Y)$ the dependent entropy) of the random variables X, Y with n possible values $\{x_1, x_2, \ldots, x_n\}$ and $\{y_1, y_2, \ldots, y_n\}$, and $p(x_i)$ as probability mass function (pmf) with $p(x_i, y_j)$ as combined and $p(x_i|y_j)$ as dependent pmf (for further details cp. Thomas [53]).

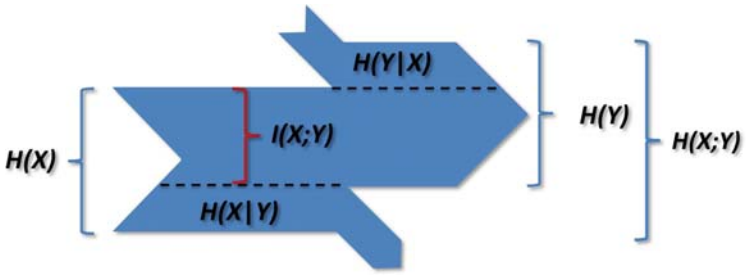

Figure 1.21.: Here eq. (1.23) is shown descriptively. The overlapping area between the information of X and Y is the mutual information.

A descriptive overview is given in figure 1.21. Here the information of two sources X, Y, described through the entropy of the random variables, is visualized. As can be seen, the information of X and Y is overlapping but not completely identical. To get the information of Y from the information of

X it is necessary to lose some information, denoted by $H(X|Y)$, and to get another, denoted by $H(Y|X)$.

The big overlapping part of the two random variables is the amount of mutual information and describes the similarity of the two sources. In this work the MI of two signals is calculated via the entropy using the following variation of eq. (1.23):

$$I(X;Y) = H(X) + H(X) - H(X;Y) \tag{1.25}$$

The entropy is evaluated via an estimation of the probability distribution using the histograms of the signals.

1.4.3. Erosion

In the second part of this work (cp. chap. 3) a common technique processing binary images, called erosion, is used to cut of the border pixels of presegmentations. A short overview will explain the result of an erosion.

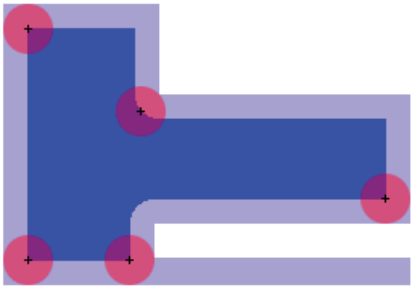

Figure 1.22.: A erosion with a disc of radius 15.5 pixel (red circle) is shown in this figure. The light and the dark blue area marks the shape before the erosion, the dark blue area the result.

An erosion of an image is a process which makes areas with the value '1' smaller. The basic idea is to compare an image with a structuring element also called 'probe'. It is tested if the simple structuring element fits the shapes in the image or not.

Using a disc with an distinct radius as a structuring element, every pixel that can be used as center of that disc, with the constraint that every part of the disc is inside a shape, is part of the resulting shape, as can be seen in figure 1.22.

2. Metal artifact reduction

As explained in chapter 1.3 cone-beam computed tomography (CBCT) images may be corrupted with artifacts caused by high-density objects such as metal implants, dental fillings or surgical clips. These streak and shadow artifacts, also known as 'starburst' artifacts (cp. [12]) because of their streak like appearance, and 'Hounsfield balk' because of the balk like shadow between metal objects, occur due to beam hardening, scatter, noise, exponential edge-gradient effect and motion (cp. chap. 1.3).

In this chapter our approach to correct these artifacts is presented. All presented steps, with the exception of the reconstruction, were developed especially for this study. Some basic ideas for the development were given by Schmidgunst, Schütz and Meilinger. In particular the segmentation process - described in detail in chapter 3 - was newly designed for this analysis.

2.1. Image acquisition

The used images were acquired using different stages of development of the C14 C-arm CBCT (cp. chap. 1.1) in clinical studies in Munich.

The first study was done in a cooperation with the surgical hospital and health care facility in the town center, which is a part of the Ludwig-Maximilian university in Munich. The main aim was a CT monitoring of osteosynthesis processes for joint reductions during operation, with the main focus on endoscopic and angle-stable techniques. Currently in case of doubt, postoperative monitoring must be accomplished, due to the mobility and large clearance of the C14 operative monitoring even for shoulder joints can be realized.

The second survey was a cadaver study in cooperation with the university hospital 'Rechts der Isar' (on the right hand side of the river Isar) in Munich. This study was made to obtain a data set of miscellaneous body parts with and without metal implants, which can be used to compare original artifact free images (respectively volumes) with artifact reduced images (or volumes).

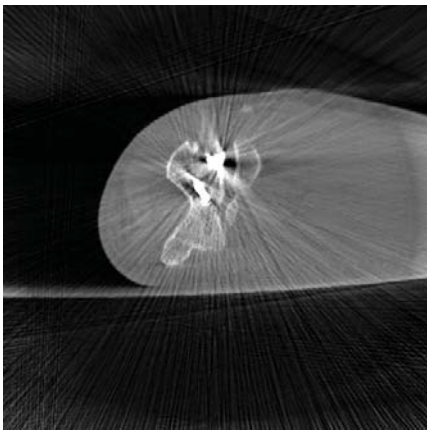

Figure 2.1.: Here an example of metal artifacts is given. The shadow around the implants and the streaks protruding the metal corrupt the whole image.

In figure 2.1 a slice of a reconstructed volume corrupted by metal artifacts is presented. The streaks and shadows can be extinguished clearly. The following section deals with these artifacts and reduce them, the results are shown afterwards.

2.2. Method

The created algorithm is divided in six major steps, explained in the following sections:

A *Reconstruction and segmentation:* The acquired 2D series is reconstructed and afterwards the metal objects are segmented.

B *Metal replacement:* The attenuation coefficients in the segmented metal volume are replaced with the attenuation coefficient of tissue. Other defective areas inside the human (or just as well animal) body are replaced with the attenuation coefficients of tissue. Finally the streak artifacts are denoised.

C *Forward projection and Alignment:* Next, the corrected 3D volume is forward projected to gain the correction values for the 2D X-ray series. The corrected projections, just obtained, must be realigned to account for distortions.

D *Truncation correction:*Due to the FOV, objects lying completely or partially outside this volume are truncated (or even completely ignored) during the forward projection. This loss of information must be corrected as well before, in the next step, the original 2D series can be corrected.

E *Metal area replacement:* In the next step the 'metal pixels' in the 2D series are replaced with the aligned and truncation corrected values. The 'metal pixels' are identified via forward projection of the segmentation.

F *Second reconstruction and metal transfer:* Afterwards the corrected 2D series is reconstructed and a corrected volume without artifacts but also without metal objects is obtained. Finally the original metal objects, segmented in step A, are transferred to the corrected volume.

2.2.1. Reconstruction and segmentation

After the recording of the 2D series, various preprocessing steps must be applied to the 2D data, like offset, gain, defect, temperature and lag correction (cp. chap. 1.1.2). This preprocessed data is denoted in the following with

$$I(u,v)_\xi \tag{2.1}$$

and

$$p(u,v)_\xi = -\ln \frac{I(u,v)_\xi}{I_0} \tag{2.2}$$

where u and v are the coordinates in the 2D series and ξ is the projection number, with $\xi = 1 \ldots n$ where n is the number of acquired projections angles. For comparison with eq.(1.1) it has to be taken care of $\theta = \xi\beta$ with β is the angle difference between two scan positions, $n\beta = \pi + \kappa$ is the complete acquisition angle of 180 degrees plus the cone angle κ (cp. chap. 1.2.1).

Using a FBP algorithm (cp. chap.1.2.2), the reconstructed and - in Hounsfield units (cp. app. B) - standardized ($HU\{\}$) volume $V(\mathbf{r})$ is gained from $I(u,v)_\xi$, where x, y and z are the three coordinates in the volume, $\mathbf{r} = (x,y,z) \in \mathbb{R}^3$ is a three dimensional vector and μ_I is the result of the FDK as in eq. (1.1).

$$V(\mathbf{r}) = HU\left\{\mu_I(\mathbf{r})\right\} \tag{2.3}$$

Now using a segmentation process all voxels from $V(\mathbf{r})$ inside metal objects must be found. This segmentation step is one of the most important steps

of this method. Every non-segmented metal voxel will generate further 'starburst' artifacts in the end. For small objects a global threshold is sufficient to segment all voxels (e.g. all voxels with values above 1850 Hounsfield units (HU) are classified), either computed with Otsu's method [37] or basic global thresholding [13]. With increasing size of the metal objects, they are generating enough shadow artifacts that interior areas cannot be segmented. This areas can get so big, that metal objects will be virtually separated and therefore cannot be segmented as one continuous object. The whole problem of the segmentation of metal objects in CBCT data and a new projective segmentation algorithm is described in chapter 3.

In this chapter it is assumed that an adequate (either threshold or projective (cp. chap. 3)) segmentation is used and the set of all voxels classified as metal voxels is denoted with M:

$$M = \{\mathbf{r}_i | V(\mathbf{r}_i) \text{ is metal voxel}\} \tag{2.4}$$

This segmentation is the base of most of the following steps.

2.2.2. Metal replacement

The 3D Volume $V(\mathbf{r})$ is a standard reconstruction including all artifacts, but it also includes large areas surrounding the metal objects which are not or only slightly corrupted. This information is used to correct the 2D series. To obtain the correction a forward projection of the reconstructed volume is used.

An important part is the replacement of the metal voxel values with values of tissue, but that is not the only replacement necessary. The artifacts must also be removed, because if a forward projection of volume data with artifacts is computed, the shadows in the near field of the metal objects decrease the attenuation and the result is not usable. Another problem is that the streaks disturb forward projections. Because of their origin the streaks lie along the projection rays, and for this reason the integral along a 'streak ray' is completely wrong. Furthermore, if the metal object itself is replaced by a tissue object but the streaks remain, the projection of them generates a virtual metal object in the projection data.

Due to that, information from metal voxels and corrupted voxels must be deleted, or in case of the metal voxels, replaced with the attenuation value of tissue, so that after the correction and reconstruction the metal objects are replaced by tissues with the same form. This will reduce the artifacts, because tissues will obviously not form the problematic artifacts.

To achieve this, the next step must replace the metal voxels and delete the artifacts. The first is easily achieved, all voxel $V(\mathbf{r}_M)$ with $\mathbf{r}_M \in M$ get a new value of $-40\,\mathrm{HU}$.

After that the artifacts must be deleted. The difference to the main problem of the artifact reduction is, that in this case it is not necessary to restore any disturbed information. The goal is to replace this information neutrally, not to affect the forward projection.

To achieve this goal, two main artifact problems must be differentiated, near the implants and far away. First the case far away is explained.

Far field The easier to solve problem concerns the 'starburst' artifacts in the far field. A simple Gaussian filter will remove these artifact. The loss of sharpness of edges is insignificant, because at the latest the forward projection of the reconstructed information (the next step in the MAR) will loose this sharpness. For this purpose a simple three dimensional Gaussian filter approximated with a binomial distribution is used. In the present data a simple distribution with $\sigma^2 = 2.5$ was sufficient. To accelerate the process the filter vector is clipped to the seven central entries:

That is, the three dimensional filter is a $7\times7\times7$ truncated normalized binomial filter

$$G_3(x, y, z) = G_1(x) \cdot G_1(y) \cdot G_1(z) \tag{2.5}$$

with

$$\mathbf{G_1} = \frac{1}{1002}[45, 120, 210, 252, 210, 120, 45] \tag{2.6}$$

To show the importance of the Gaussian smoothing an example is presented. In fig. 2.2 a real X-ray image acquired with the mentioned system is shown. The detail displays a elbow joint after surgery. In fig. 2.3 the result of the metal implant replacement is shown in the upper left, the same image without the Gaussian filtering before the forward projection is on the upper right, and the difference of these two pictures can be seen in the lower left corner.

At a first look, it seems that the smoothing of the volume only smoothed the data and therefore reduced the edges of the screws.

To verify or falsify that assumption, it is necessary to display the complete area which is affected by the replacement. In order to get that information, in the lower right corner a picture with a consciously wrong replacement is projected and presented. The whole replaced area was set to a considerably higher attenuation. Due to that the affected area is highlighted.

Figure 2.2.: This image is a part of an original X-ray image made with the described C-arm CBCT. A fixed elbow joint with 4 screws and 2 metal pins is shown.

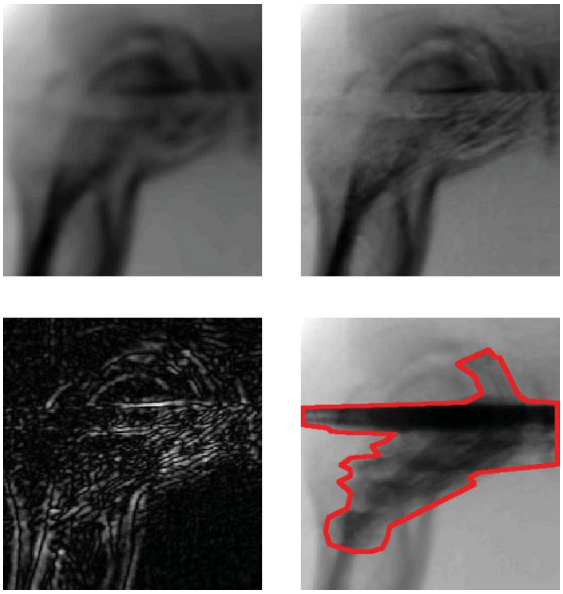

Figure 2.3.: In this image the forward projection of a replaced and smoothed volume is presented in the upper left corner, in the upper right corner only the replacement is applied. In the lower left the difference of the two upper images is shown and in the lower right a purposely wrong replaced and forward projected volume is presented. The red line marks the border of the corrected area (the improved replacement described in chapter 3.3 is used).

It can easily be seen that the border of the replaced area (the red line) encloses all metal implants in this projection. The same can be seen in the other projections and in the volume. The considerably bigger volume that is replaced in comparison to the metal implants is due to the wide area of corrupted voxel in this scan. The reason for that lies in the arrangement between scanner and patient, which was inappropriate (cp. chap. 3.3).

That is, the original edges of the metal objects which protrude in the upper right picture were actually completely erased, but even in the incorrect replaced projection, the edges of the implants can be seen. The assumption above of the first look is false. The metal is 'reconstructed' from the streaks through forward projection, thus it is very important to reduce them by smoothing.

Near field The second problem is in the near field of the metal objects. Between or close to metal objects, the artifacts generate shadows which assume air inclusions inside the observed body. These shadow voxels must be segmented and also replaced by a value of $-40\,\mathrm{HU}$ (like the metal voxels). The segmentation is obtained by two threshold steps and a flood fill operation.

First, all voxels with values above $-550\,\mathrm{HU}$ are classified as 'inside' the body. To find holes in the body, all voxels not classified as 'inside' which are not connected to a voxel outside the body are now also classified as 'inside', using a flood fill operation. This part assures that only voxels truly lying inside the scanned object are replaced. Then all 'inside' voxels with a value below $-340\,\mathrm{HU}$ (in the following denoted as 'air-inclusion' voxels, the value is low enough that the lung is not classified) are replaced with a value of $-40\,\mathrm{HU}$.

An advanced replacement can be obtained, if the reliability from the new segmentation is used. This method is described in chapter 3.3 and already used in the present data sets (e.g. cp. fig 2.3).

An example is presented in fig. 2.4 showing a layer of the reconstructed volume of the elbow joint on the left and all as 'air inclusion' detected voxels on the right. Additional to the correctly segmented voxels the edge of the body is detected also, but due to the few segmentations and the following Gaussian blurring this effect can be ignored.

Because the replacement of metal and 'air inclusion' voxels often leads to sharp edges, the Gaussian filter, which removes far field 'starbursts', is applied as the third and last step of replacement calculations. This way it also reduces edges introduced by the earlier applied correction methods. In the end we obtain the replaced and filtered volume $R(\mathbf{r})$ (see fig. 2.5).

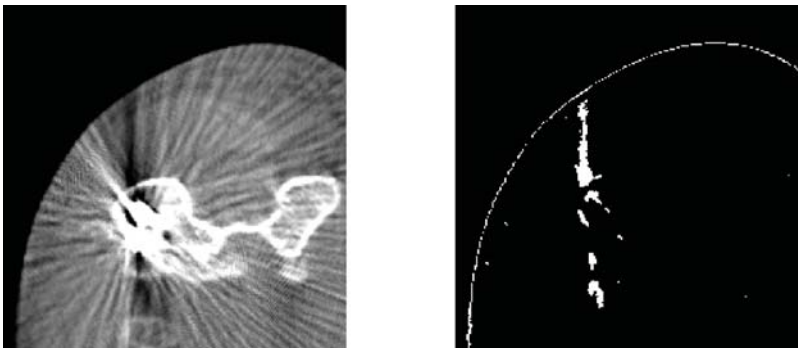

Figure 2.4.: This figure shows a detail of the reconstructed elbow joint with artifacts on the left side (window −550 HU to 1000 HU) and the detected 'air inclusions' on the right side

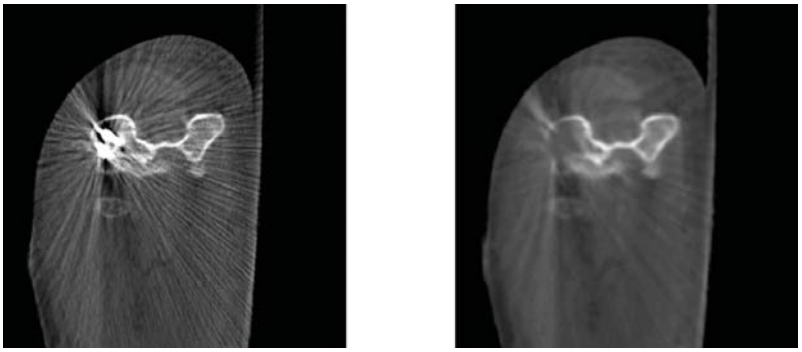

Figure 2.5.: Left a detail of the original reconstruction is shown, right the same detail of $R(\mathbf{r})$ (window −550 HU to 1000 HU)

2.2.3. Forward projections and alignment

To correct the 2D information with the replaced 3D volume, it is necessary to forward project the original 3D data, the metal segmentation and the corrected volume (denoted as $V_{fp}(u,v)_\xi$, M_ξ and $R_{fp}(u,v)_\xi$).

With :

$$M_\xi = \left\{(u_i, v_i)_\xi | l_{(u,v)_\xi} \text{crosses at least 5 voxels} \in M\right\} \tag{2.7}$$

where $l_{(u,v)_\xi}$ is the ray path through the volume hitting the image with number ξ at position (u,v) (cp. chap. 1.2.3).

To reduce the duration of the algorithm it is only required to compute the pixels in a region-of-interest (ROI). To get this region, a whole forward projection of the metal segmentation in 3D is estimated and then a rectangular area around the pixels-to-correct with enough tolerance is chosen.

As mentioned before, one challenge of this method is that a mobile C-arm CT is used for data acquisition. The C-arm is not as stable as a gantry and because of the incomputable distortion, the calibrated geometry, which is used for the reconstruction, differs from the real scan geometry. This difference results in a lateral misalignment between the scanned 2D data and the forward projected data.

To reduce the lost information and also to maintain the intersections between original and corrected structure it is necessary to realign the computed corrections.

During a proof of concept of CT data stitching (cp. annex A) an intrinsic realignment, using among other things, a mutual information criterion [33] was developed. The realignment takes care of a shift in u and in v axis, denoted as d_u and d_v. It can be expanded by a rotation parameter, but a shift correction only is sufficient for the distortion.

To find the correct realign parameters, first the uncorrected unreplaced 3D volume is forward projected into 2D, after that an edge filtering (F_{edge}) is applied to the projected and the original data. The filter takes care of the discrepancy between original ($p(u,v)_\xi$) and projected data ($V_{fp}(u,v)_\xi$) for example as a result of truncation (compare with the next step). Hence only high frequencies are used for registration.

As F_{edge}, a combination of 180 Gabor filters with an angle difference of 1 degree is used (see fig. 2.6).

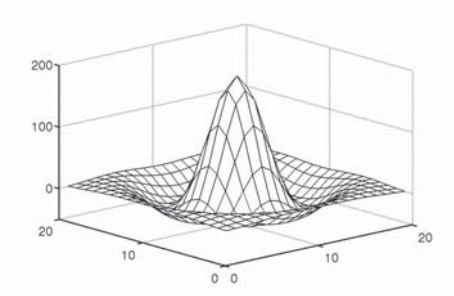

Figure 2.6.: A combination of 180 Gabor filter with a difference of 1 degree, resulting in a Mexican hat, are used as edge filter for the realignment.

These edges were realigned by a maximization of the mutual information. To accelerate this computation, once again only a part of the picture is used. The best part is the area with the metal objects because of the high contrast, therefore the ROI from before can be used.

p^{n_u,n_v,b_u,b_v} is the part of the Image $p(u,v)_\xi$ beginning from point n_u, n_v with an image size $b_u \times b_v$:

$$\begin{aligned} p^{n_u,n_v,b_u,b_v} = p(&n_u, n_v; && \ldots; && n_u + b_u, n_v; \\ &n_u, n_v + 1; && \ldots; && n_u + b_u, n_v + 1; \\ &\vdots && \ddots && \vdots \\ &n_u, n_v + b_v; && \ldots; && n_u + b_u, n_v + b_v)_\xi \end{aligned} \tag{2.8}$$

(analogous $V_{pf}^{n_u+d_u,n_v+d_v,b_u,b_v}$).

To get d_u and d_v we maximize:

$$\arg\max_{d_u,d_v} I\left(F_{edge}\left(p^{n_u,n_v,b_u,b_v}\right); F_{edge}\left(V_{pf}^{n_u+d_u,n_v+d_v,b_u,b_v}\right)\right) \tag{2.9}$$

In figure 2.7 a ROI from an original scan (top left) and the forward projection of the first reconstruction (top right) is shown. It can be seen, that the background ist different due to the incompleteness of the forward projection from the field of view (FOV) (cp. chap. 1.2.4). After the edge filtering (see line 2 of fig. 2.7) this effect is decreased.

The last step of the realignment process is the computation and maximization of the MI between the edge images with shifts in x and y-direction, shown in fig. 2.8. The presented map indicates a maximum at $dy = -2$ and $dx = 0$ (the middle (zero shift), is marked with a dot), that is the forward projected image must be moved 2 pixels to the bottom to align with the original image.

2.2.4. Truncation correction

As mentioned before (cp. chap. 1.2.4 and 2.2.3), reconstructed and then forward projected data differs from the original not only by a misalignment, also truncation is a serious problem.

In the clinical daily routine for the most part the scanned objects are greater than the FOV. It is also possible that other objects are located outside the FOV but inside the scan geometry. In this case, these parts are radiographed

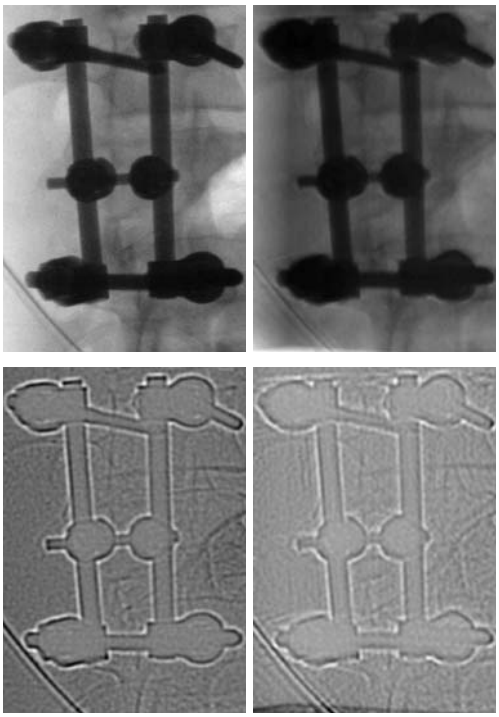

Figure 2.7.: On the top left side a detail of the original CBCT scan and on the right the same area from the forward projection of the first reconstruction is presented. The two images below show the results of a edge filtering.

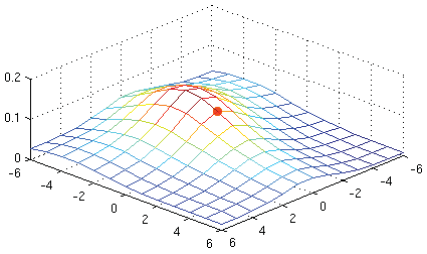

Figure 2.8.: This figure shows the mutual information value for different shifts for the data from fig. 2.7. The height of the surface shows the mutual information and the shift is plotted on the X/Y-axis.

but not reconstructed, due to that fact it is impossible to project them into the correction. If these objects are ignored, additional artifacts are generated.

To correct this problem, a truncation image $Tr(u,v)_\xi$ is generated. It is computed as the difference between $p(u,v)_\xi$ and the realigned $V_{fp}(u+d_u, v+d_v)_\xi$ (as always only the important ROI is calculated).

$$Tr(u,v)_\xi = p(u,v)_\xi - V_{fp}(u+d_u, v+d_v)_\xi \tag{2.10}$$

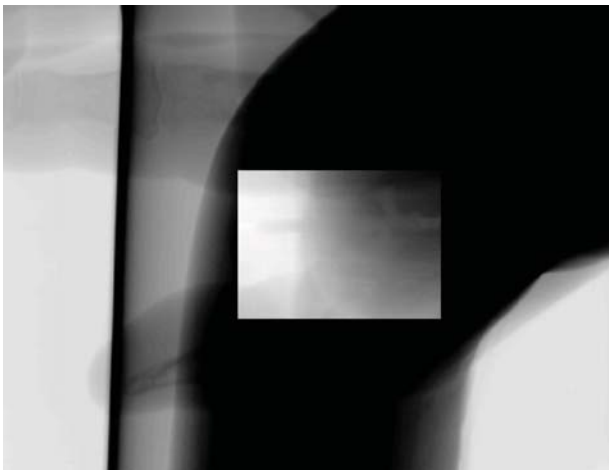

Figure 2.9.: In this figure the truncation correction map of a distinct X-ray CBCT projection image is presented.

To avoid new artifacts in the image section of metal objects, the truncation correction map is computed only around the objects, and then the actual interesting area is interpolated. In figure 2.9 the result is shown. As before, only in an ROI around the metal implants the truncation correction is computed. Because of that it looks like it is possible to see through the arm like through a window in a wall. Most notable the hand of the subject (lying totally outside of the FOV) is continued in the computed area.

2.2.5. Metal area replacement

At this point the metal is segmented and the forward projections of the corrected 3D volume, the realignment parameters, and the truncation correction map are computed. In this step this information is combined.

To avoid discontinuous edges between the original data outside and the corrected data inside the correction area, this area must be adjusted to the original data. The adjustment $E(u,v)_\xi$ is calculated by computing the difference between the original values of the pixels encircling this area and the corrected values of the same pixels. Then every adjustment value inside is interpolated from this boundary and added to the other corrections.

All metal pixels M_ξ (with an additional boundary from 1-2 pixels) were replaced with the corresponding pixels from $R_{fp}(u,v)_\xi$ which were corrected, using the truncation image and the adjustment $E(u,v)_\xi$, and realigned. The resulting 2D series is denoted with $p_1(u,v)_\xi$.

$$p_{cor}(u,v)_\xi = R_{fp}(u+d_u, v+d_v)_\xi + Tr(u,v)_\xi + E(u,v)_\xi \tag{2.11}$$

$$p_1(u,v)_\xi = \begin{cases} p(u,v)_\xi & \text{if } (u \pm 2, v \pm 2) \notin M_\xi, \\ p_{cor}(u,v)_\xi & \text{otherwise.} \end{cases} \tag{2.12}$$

Figure 2.10.: In this figure a complete original projection image is shown. The whole histogram is shown.

To present the results an original image from one of the clinical scans is shown before and after the correction. To enhance the details with a better contrast the histogram window is adjusted to a part of the image. In order to give an overview of the complete image, it is shown in fig. 2.10 windowed over the whole histogram. In fig. 2.11 the image is displayed with a higher resolution and a smaller histogram window. In the upper image, the original scan can be seen, 4 screws and 2 metal pins are inserted in the elbow junction (cp. 2.2).

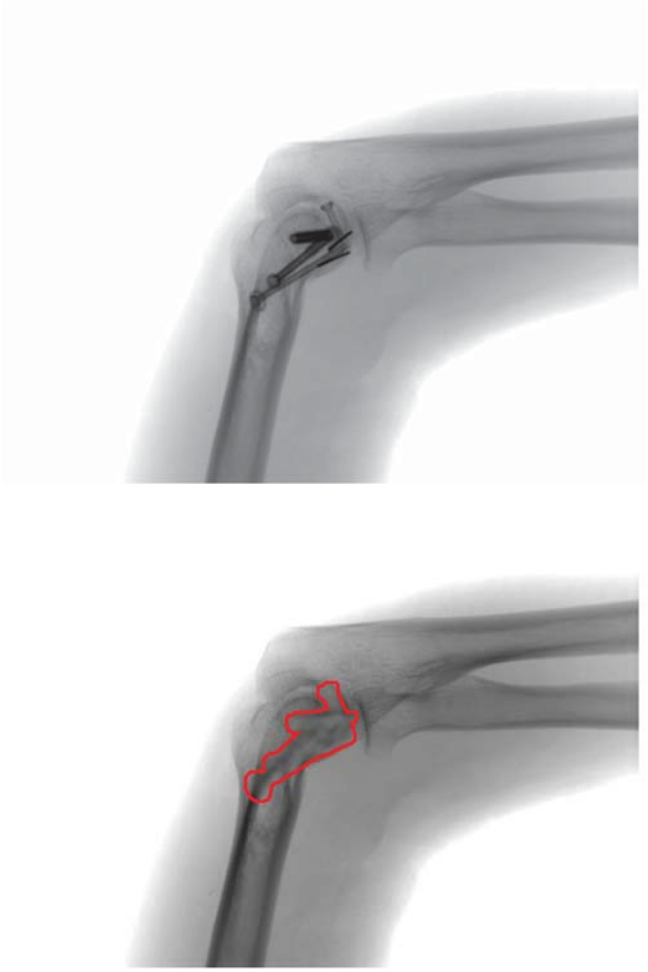

Figure 2.11.: The images above show a comparison between original and corrected versions of a scan from the same angle. The histogram is adjusted to enhance the contrast of important area (cp. fig. 2.10).

Below the corrected image is shown, the red line indicates the area in which corrections are applied. Outside this line the image is identical to the original. It can be seen, that details, like bone edges, continue in the replaced area, pointed out in fig. 2.12.

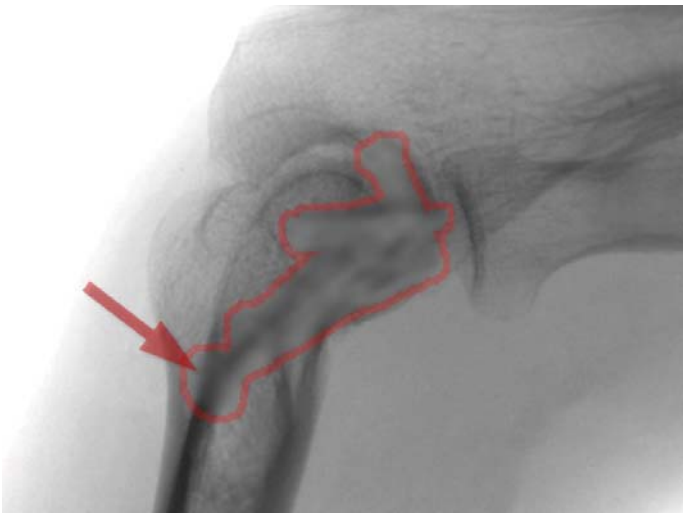

Figure 2.12.: In this figure the corrected area of the lower image in fig. 2.11 is zoomed in. The red arrow highlights a split of the bone edge completely inside of the computed region, even one of the parts stays almost completely inside this area.

In particular it can be seen that complex structures, like bone edges splitting inside the corrected area which cannot be easily obtained by interpolations, are preserved.

2.2.6. Second reconstruction and metal transfer

Now the corrected 2D images $p_1(u,v)_\xi$ can be reconstructed again. The resulting 3D volume $V_1(x,y,z)_\xi$ contains all the same information as before, only the metal objects are replaced with tissue, and thereby the artifacts are highly reduced or even vanished.

To use the result for medical treatment or diagnosis, it is necessary to see the metal implants, which vanish during the reduction process. This can be achieved by a superimposition of the known metal segmentation and the corrected reconstruction.

Depending on the application, different superimpositions can be used to show additional information like reliability (cp. chap. 3.3). More details about the improved display are described in chapter 3.4.

2.3. Results

The following pages show the results of the MAR algorithm with all improvements mentioned and developed in this work. The different superimpositions (see above) with more information are shown in the corresponding chapter 3.4.

For illustration of different aspects and results four different scans were used. Scan 1 and 2 were from the study with the surgical hospital, scan 3 to 4 were gathered during the cadaver study. The different parameters used in the scans (like detector size, volume size, number of angles etc.) or in the reconstructions can be read in following tables.

Case	body part	# of pict.	Voltage kV	Current mA	scan date
1	right elbow	400	100	2.3	May 23 2006
2	right heel	200	100	2.3	May 17 2006
3	chest	200	100	4.6	Oct 07 2009
4	left knee	200	100	4.6	Oct 07 2009

Case	2D size (in pixels)	pixel size (in mm)	3D size (in voxels)	voxel size (in mm)
1	1024×768	0.194	$512 \times 512 \times 384$	0.399985
2	1024×768	0.194	$512 \times 512 \times 384$	0.398906
3	768×768	0.194	$512 \times 512 \times 512$	0.298742
4	768×768	0.194	$384 \times 384 \times 384$	0.40

As the following images show, the algorithm reduces the streak artifacts almost completely in all cases and is capable to reduce the shadow artifact efficiently in most cases (a very good example is case 3 in fig. 2.17 and fig. 2.18).

In the first case the segmentation was very easy, a simple threshold was sufficient. But due to the fact, that in several images the patients hand, which was lying outside of the FOV, was positioned in the X-ray beam the truncation correction was necessary.

The second case has no truncation problem and the metal implants were not too much. But inside the bulk of metal implants, problems during the MAR protrude.

Because only in a few pictures, particular in case three, the area between the two groups of connected metal objects can clearly be seen, the shadow artifacts are very large there in the original reconstruction. The algorithm is capable of removing most of these shadows. Also a lot of truncation is present in these recordings, because the chest is in principle larger than the FOV.

The last case was easy to segment like case two, but the amount of metal implants is higher, so more artifacts exist and it is harder to correct them.

In figure 2.13 the different positions of the 4 scans can be seen. To make a comparison easier the results were shown on two opposing pages.

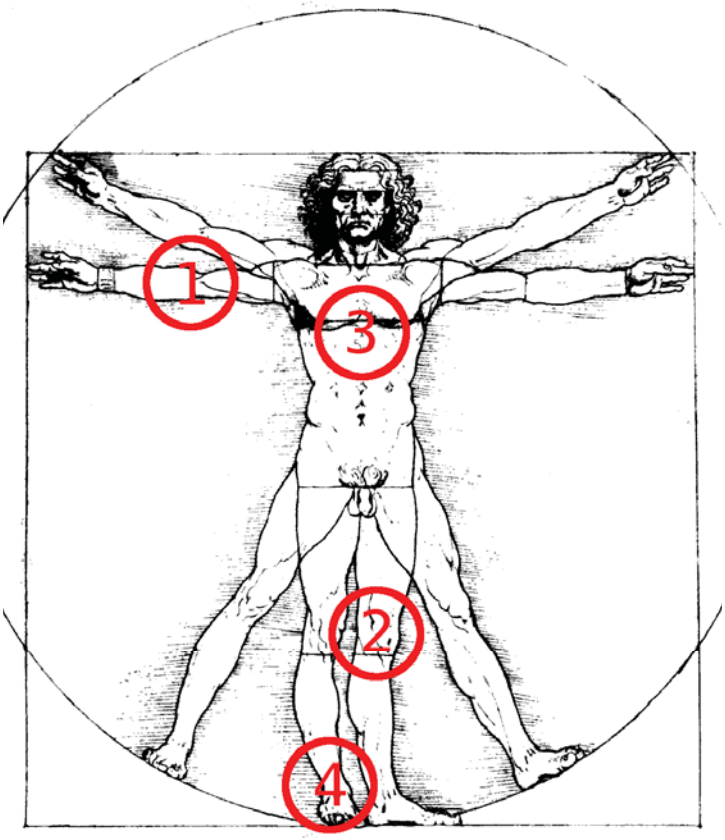

Figure 2.13.: In this sketch from Leonardo da Vinci, the different positions of the four data sets are marked.

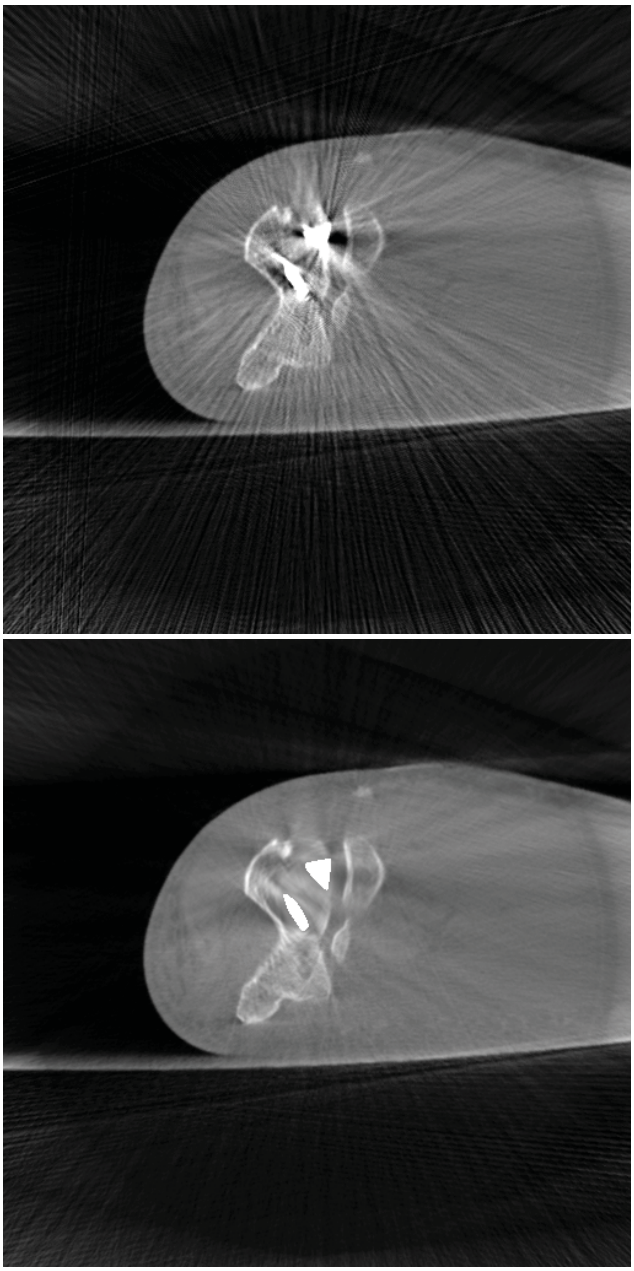

Figure 2.14a: Without (upper) and with MAR (lower)

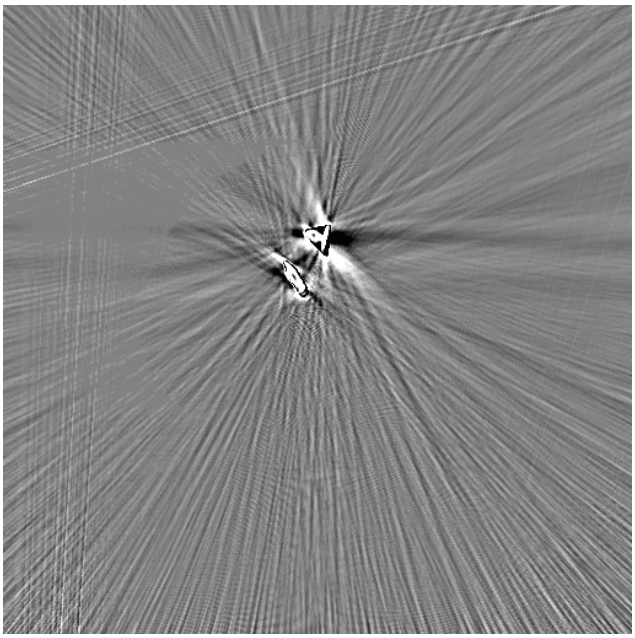

Figure 2.14b: Difference Image

Scan 1 : These details show a slice crossing the elbow joint. On the left the humerus is shown and right of the humerus the beginning of ulna and radius can be seen. Several screws fix the humeral head and surgical neck. The great improvement between the reconstruction with and without metal artifact reduction (MAR) can be seen. Most of the streak artifacts are removed and the big shadow artifacts are strongly reduced. (Windowed from -1000 HU to 1000 HU). The subtraction (Windowed from -500 HU to 500 HU) of the two images is shown above. The main difference concerns the artifacts, practically no anatomical information is affected.

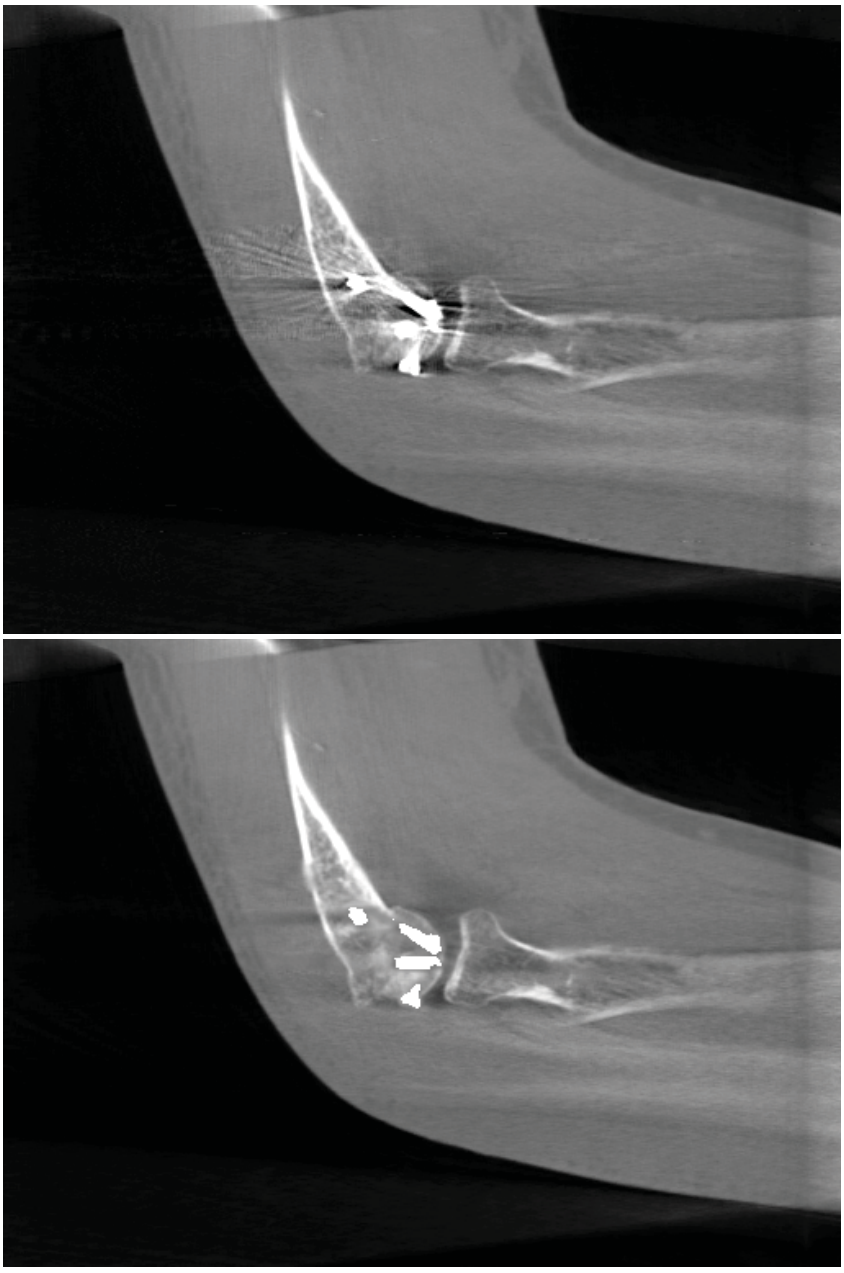

Figure 2.15a: Without (upper) and with MAR (lower)

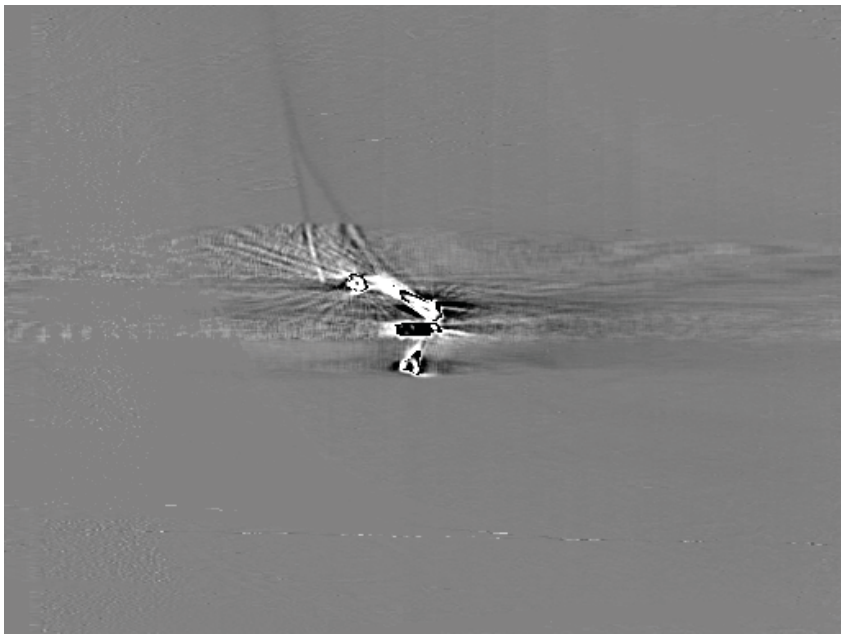

Figure 2.15b: Difference Image

Scan 1 : These details show the same scan, but a slice perpendicular to the fig. 2.14. On the left a part of the humerus, mainly it's head, is shown and on the right, the beginning of the radius can be seen. The streak and shadow artifacts are considerably reduced again. (Windowed from -1000 HU to 1000 HU). The subtraction (Windowed from -500 HU to 500 HU) of the two images is shown as before. As before, the main difference also concerns the artifacts, only the humerus edges near the implants are somewhat disturbed.

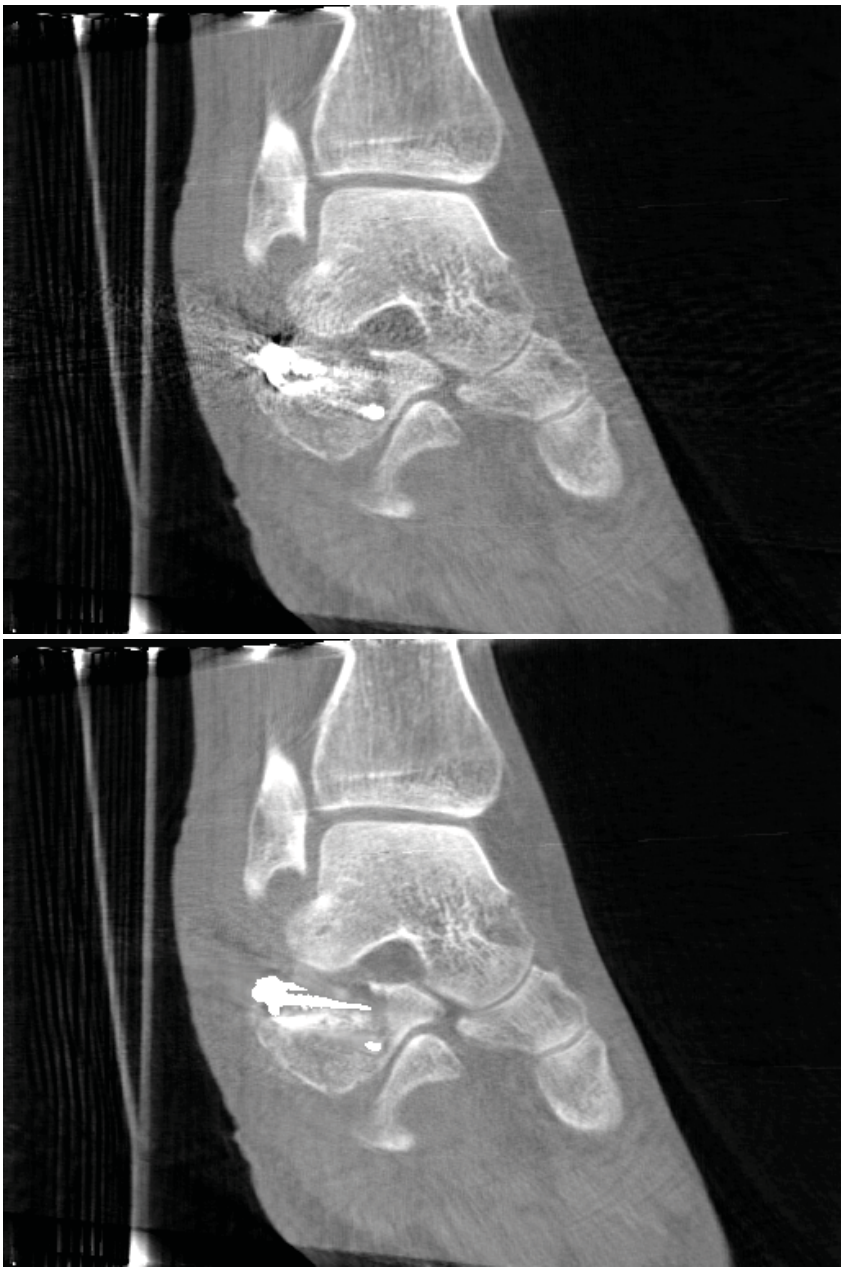

Figure 2.16a: Without (upper) and with MAR (lower)

Figure 2.16b: Difference Image

Scan 2 : These details show the right heel. The slide crosses the fixed calcaneus in mid of the foot. The streak and shadow artifacts are considerably reduced again. (Windowed from −1000 HU to 1000 HU). As before, the main difference also concerns the artifacts (Windowed from −500 HU to 500 HU).

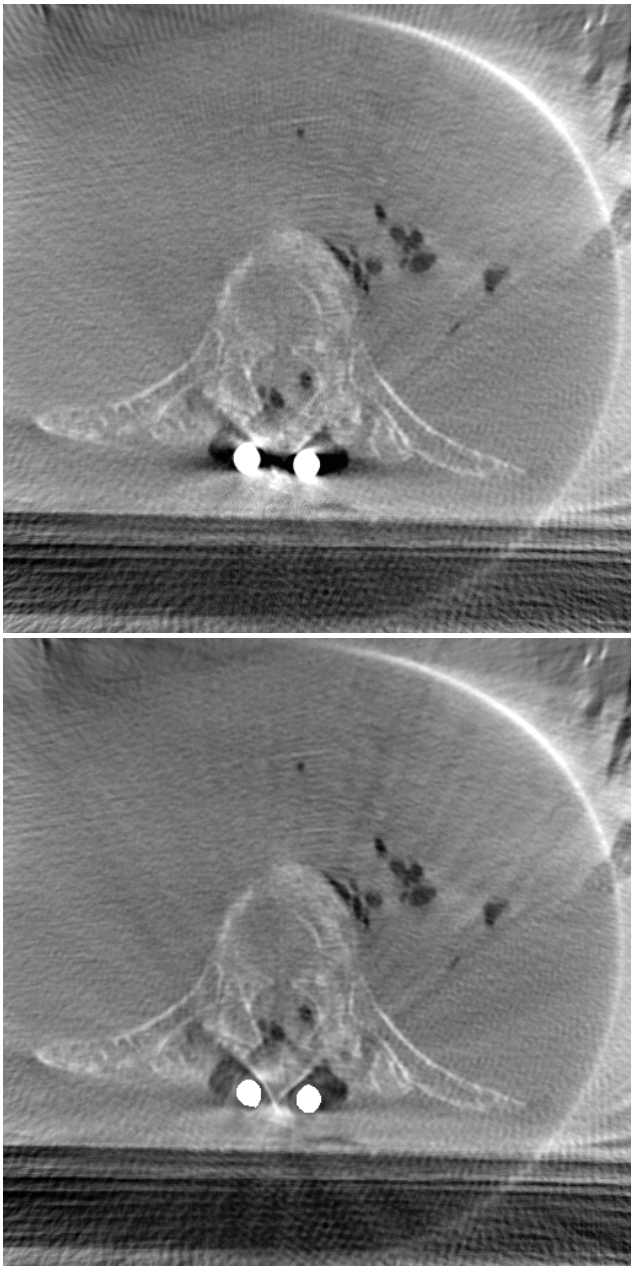

Figure 2.17a: Without (upper) and with MAR (lower)

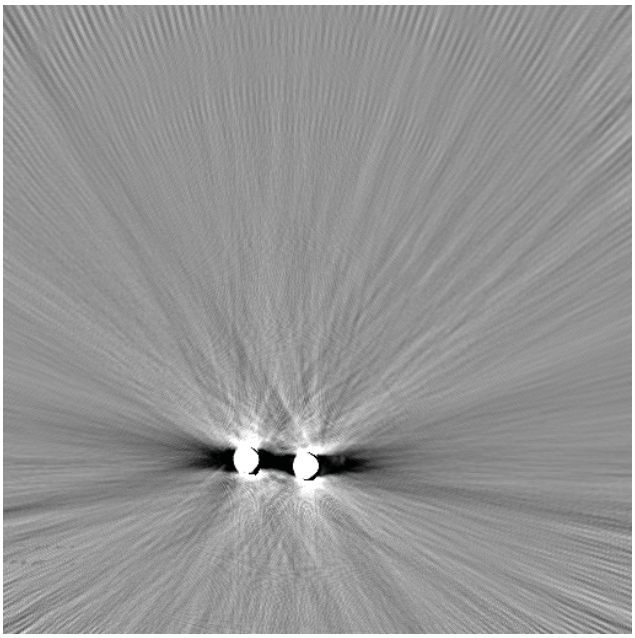

Figure 2.17b: Difference Image

Scan 3 : These details show several thoracic vertebrae in the middle segment of the vertebral column. The slide crosses a vertebral body in transversal plane. In this case the shadows dominate the artifacts, after the correction the shadow artifacts are gone and anatomical structure protrudes (Windowed from -1000 HU to 1000 HU). In the subtraction (Windowed from -500 HU to 500 HU) of the two images additional several reduced streaks can be identified.

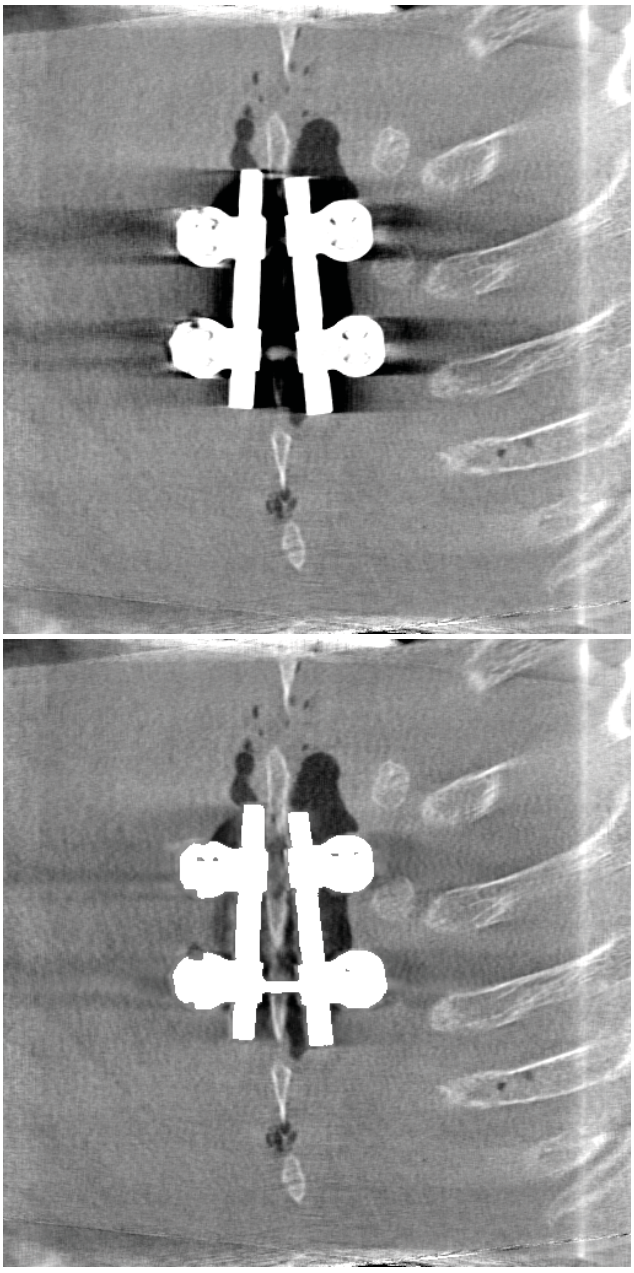

Figure 2.18a: Without (upper) and with MAR (lower)

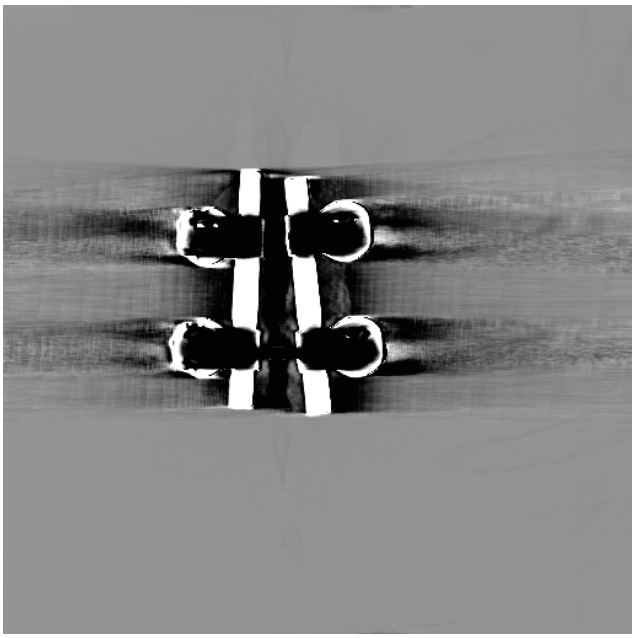

Figure 2.18b: Difference Image

Scan 3 : These details show the same middle segment of the vertebral column as in fig. 2.17. The slide is in coronal plane. As in the figure before the large shadow artifacts are nearly completely corrected, but a additional metal part between the left and right implant appears, the reason for this purpose is the improved segmentation algorithm, with a more detailed presentation this fact can be seen, therefore see chap. 3.4 (Windowed from -1000 HU to 1000 HU). In the subtraction (Windowed from -500 HU to 500 HU) it can be seen, that only areas which are associated to the metal implants, due to the projection geometry, are altered.

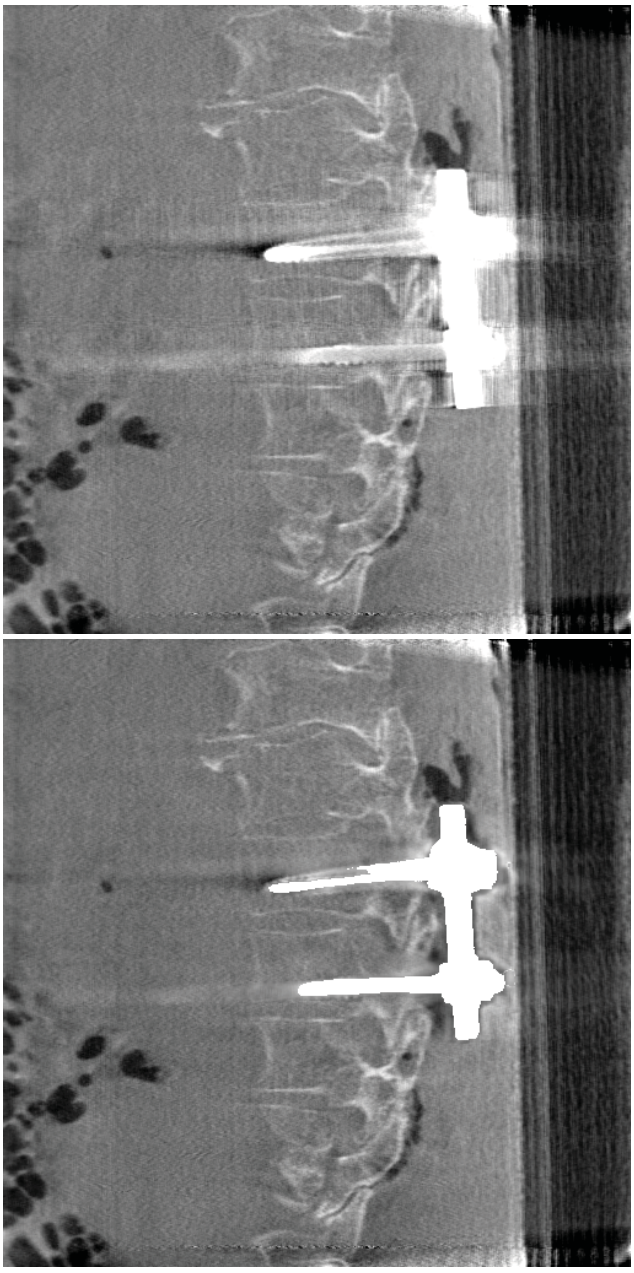

Figure 2.19a: Without (upper) and with MAR (lower)

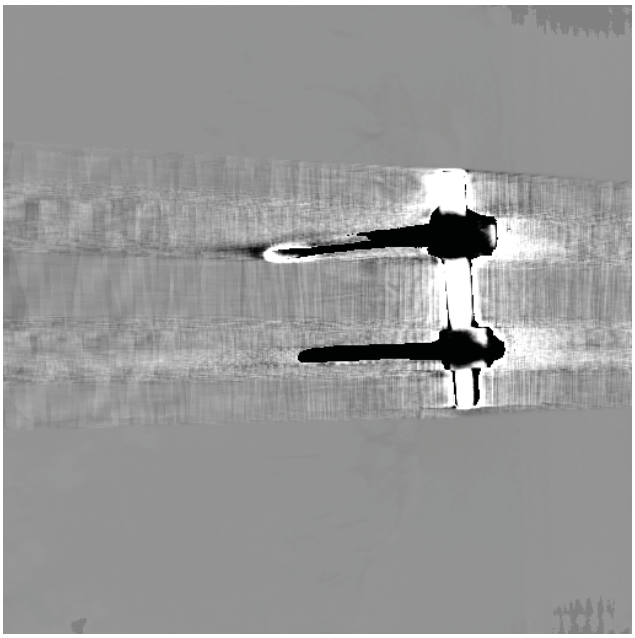

Figure 2.19b: Difference Image

Scan 3 : These details show the same middle segment of the vertebral column as in fig. 2.17 and fig. 2.18. The slide is in sagittal plane. In these slides the metal implants are artificial increased on the right side and the lower metal screw is artificially decreased during the reconstruction. The MAR corrects both effects (Windowed from −1000 HU to 1000 HU). In the subtraction (Windowed from −500 HU to 500 HU) the corrected streak artifacts in transversal plane can be seen.

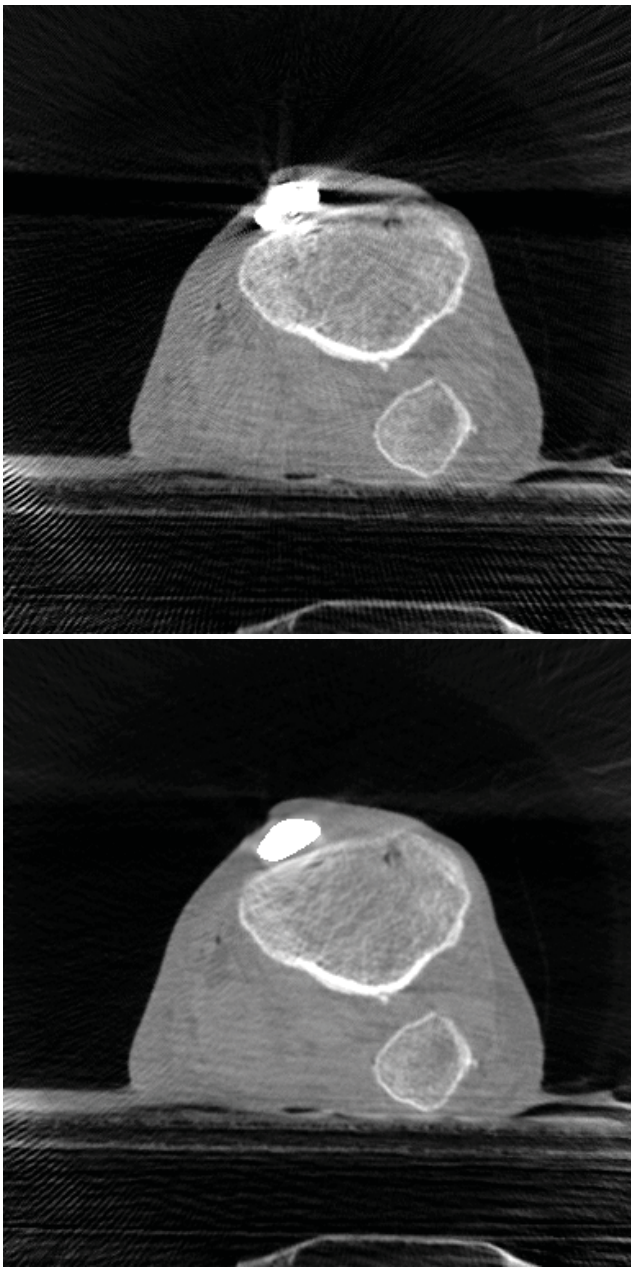

Figure 2.20a: Without (upper) and with MAR (lower)

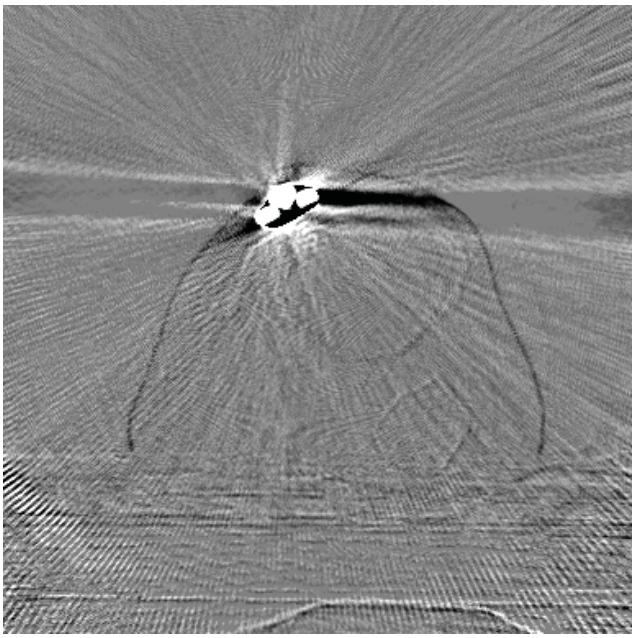

Figure 2.20b: Difference Image

Scan 4 : These details show the knee joint. The slide is in transversal plane and shows the tibia with fixation on side and the fibula. The artifacts are well reduced and the border of the human body is clearly visible (in contrary to the uncorrected image) (Windowed from −1000 HU to 1000 HU). In the subtraction (Windowed from −500 HU to 500 HU) a slight residue of the edges is visible, though not the complete showed difference is owing the MAR algorithm. In this case the HU correction (cp. chap. 2.2.1) had induced a problem between the original reconstruction and the corrected one. Since this was no concern of this work further investigation will be carried out from other site.

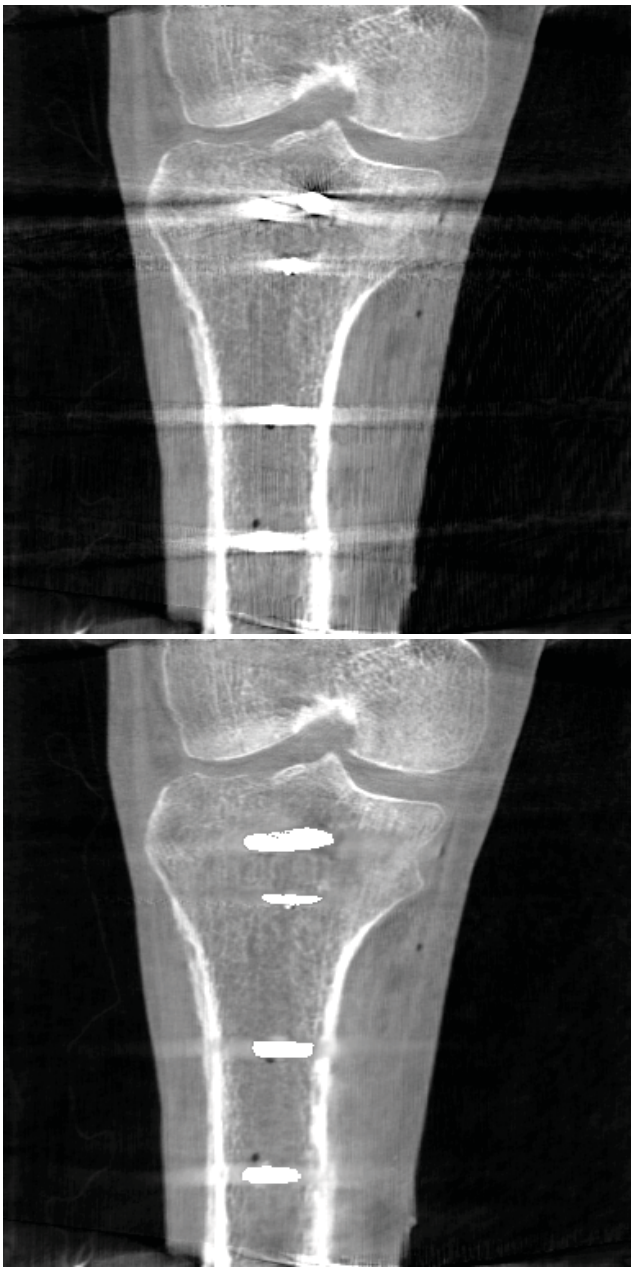

Figure 2.21a: Without (upper) and with MAR (lower)

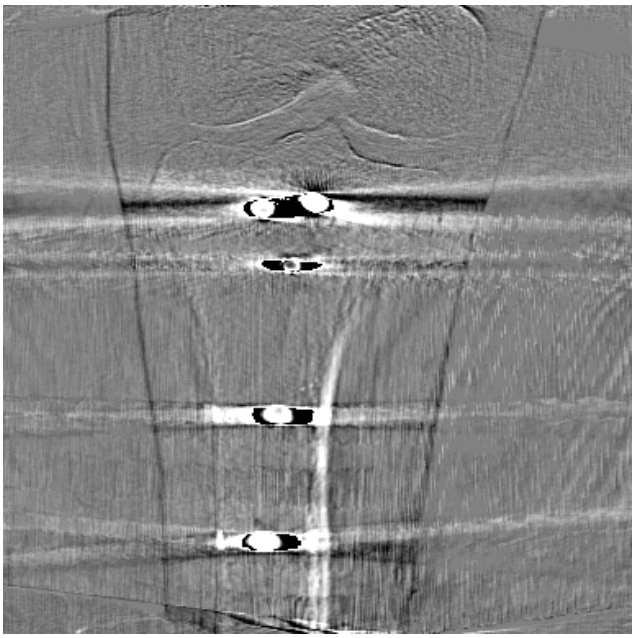

Figure 2.21b: Difference Image

Scan 4 : These details show the knee joint in coronal plane. The slide shows the fixed tibia and a part of the femur. The artifacts are well reduced but it can be seen, that depending on the orientation the MAR algorithm is better or worse (Windowed from -1000 HU to 1000 HU). In the subtraction (Windowed from -500 HU to 500 HU) a residue of the edges is visible like before (cp. fig. 2.20).

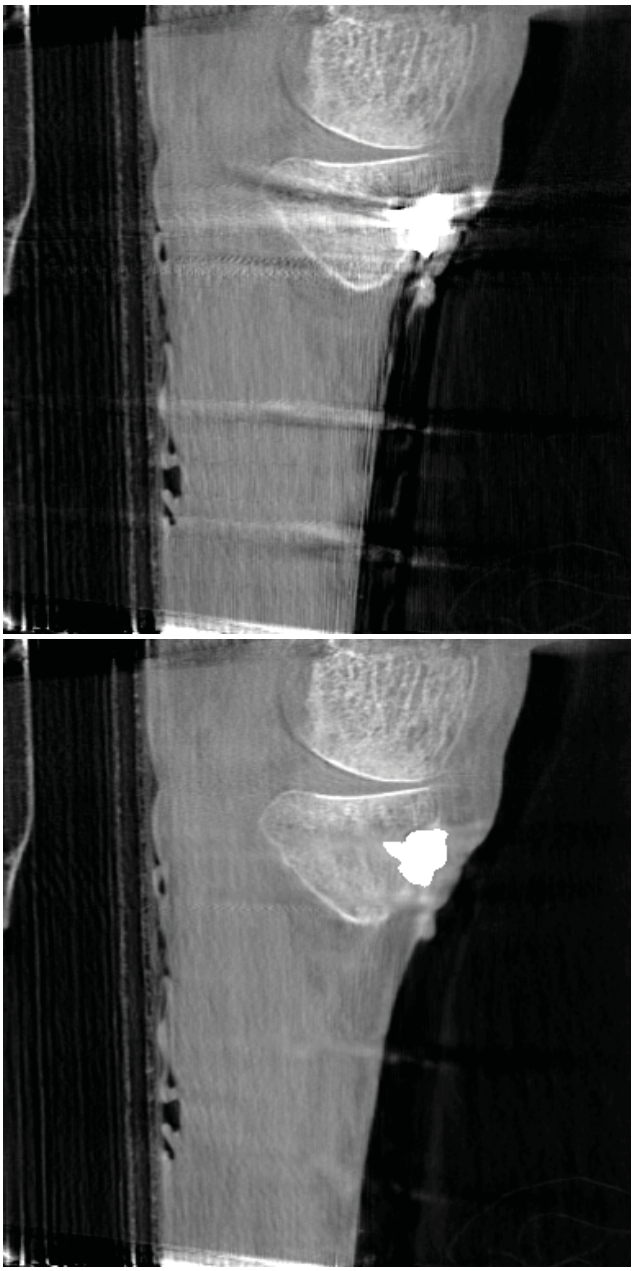

Figure 2.22a: Without (upper) and with MAR (lower)

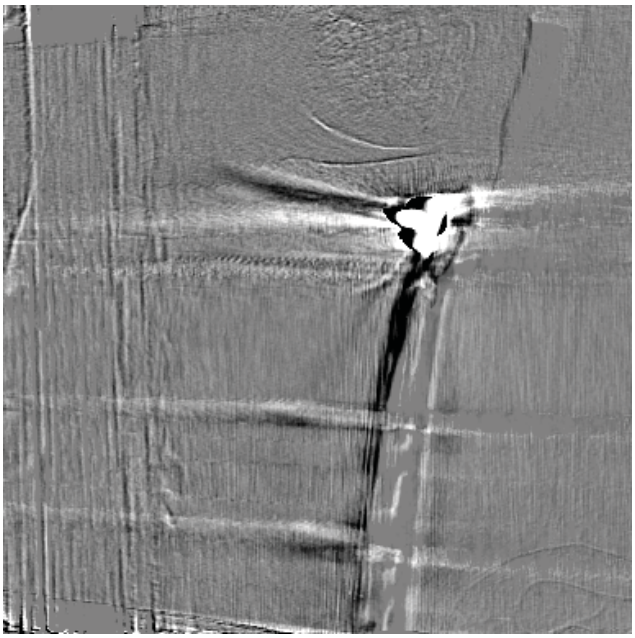

Figure 2.22b: Difference Image

Scan 4 : These details show the knee joint in sagittal plane. Again the fixed tibia and a part of the femur is displayed. The artifacts are considerably reduced in this plane (Windowed from −1000 HU to 1000 HU). In the subtraction (Windowed from −500 HU to 500 HU) a residue of the edges is visible like before (cp. fig. 2.20).

Open problems

A few cases show that sometimes areas located near large metal implants are blurred, e.g. in figure 2.23. Especially large implants lying parallel to the CT rotation plane create these effects, because most of the time during the scan the concerned areas lie behind the metal objects. In chapter 3.3, as mentioned before, a method to identify these bad regions is presented.

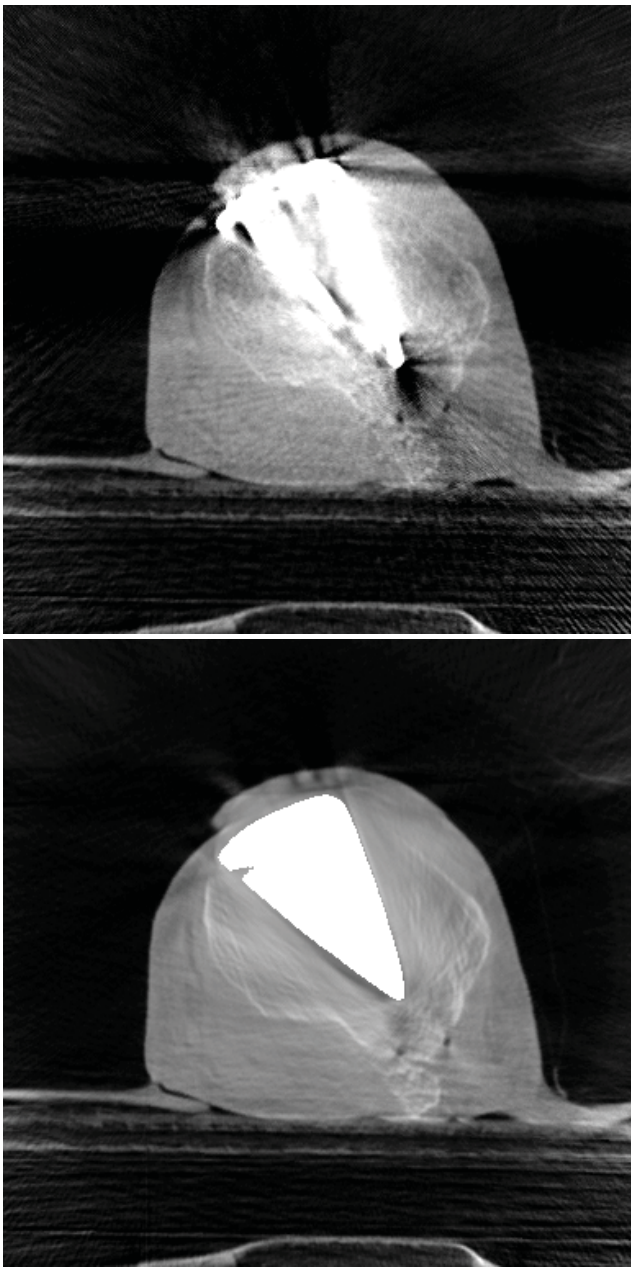

Figure 2.23a: Without (upper) and with MAR (lower)

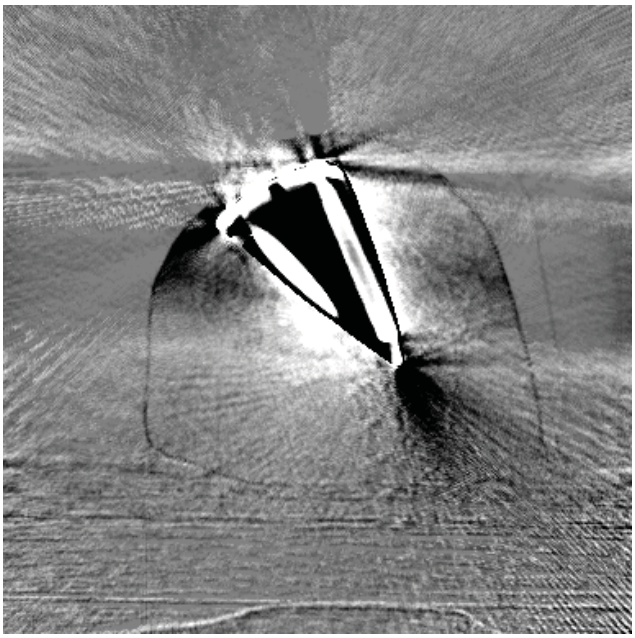

Figure 2.23b: Difference Image

Scan 4 : These details show the knee joint already shown in fig. 2.20. The slide is in transversal plane and shows the tibial head. The metal implant is larger than in the figures till now. It can be seen, that the MAR algorithm corrects the artifact in an appropriate way but blurs information around the metal implant. This effect is also discussed in chapter 3.4(Windowed from -1000 HU to 1000 HU). In the subtraction (Windowed from -500 HU to 500 HU) the blurring can be seen, as the edges appear in the difference image.

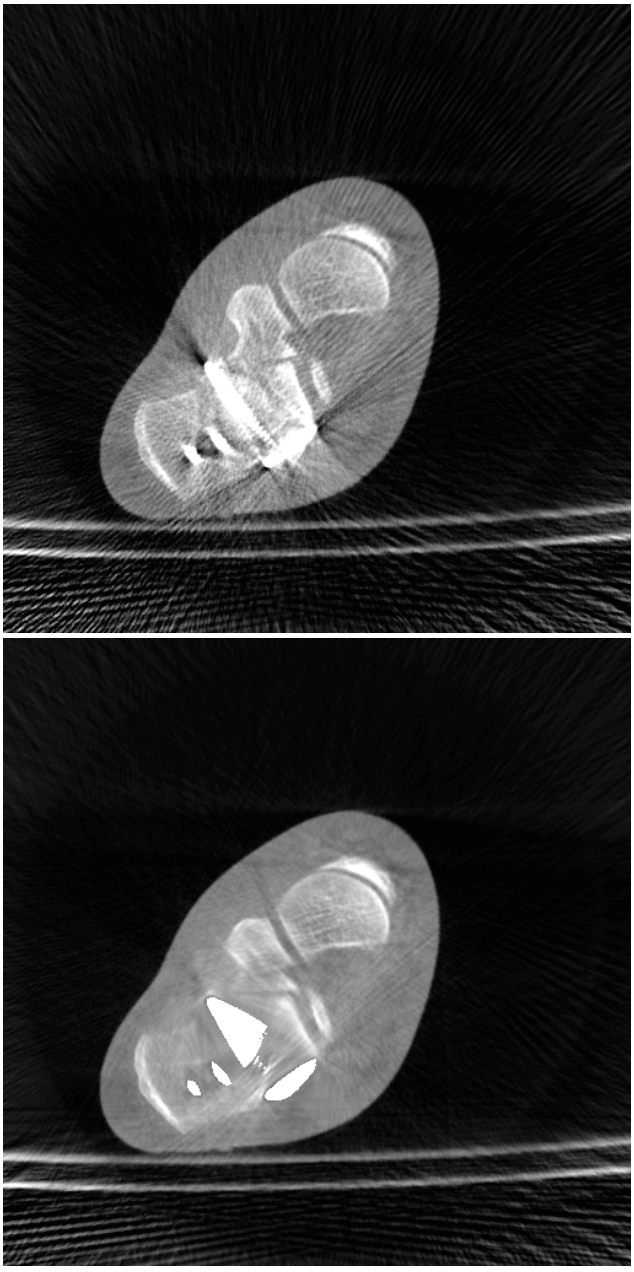

Figure 2.24a: Without (upper) and with MAR (lower)

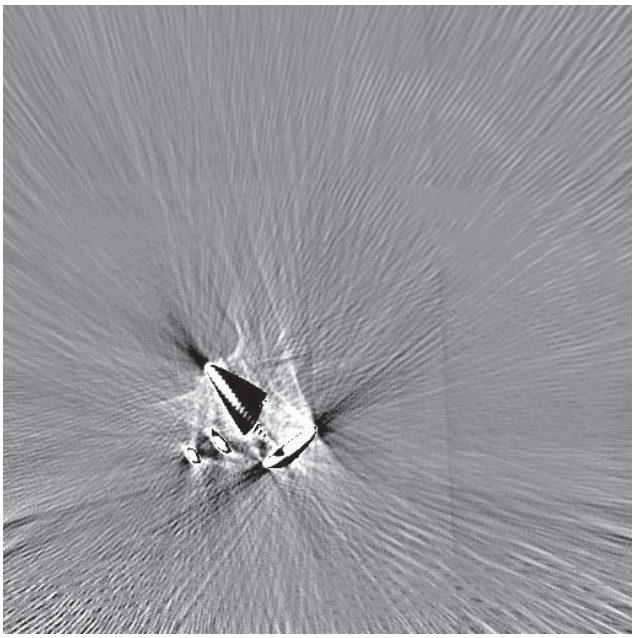

Figure 2.24b: Difference Image

Scan 2 : These details show the right heel from fig. 2.16. The slide crosses the fixed calcaneus in mid of the foot in transversal plane. The streak and shadow artifacts are reduced again but the information around the upper left part of the implants is considerably blurred. (Windowed from -1000 HU to 1000 HU). This blurring is also visible in the difference image (Windowed from -500 HU to 500 HU).

3. Segmentation of metal objects

While doing research on metal artifact reduction it became obvious that metal implants which are large enough to generate shadows that corrupt the metal objects themselves, were hard to segment by using standard methods (listed below).

Because a good segmentation is a very important prerequisite for a functional MAR algorithm, the work focuses also on an advanced method to identify the metal object without a priori information of the implants. Often, this information is not at hand or did not exist (e.g. battlefield injuries), therefore a segmentation method which does not need it is preferred.

A combination of two thresholding processes with a simple reconstruction was initiated by an article from Zhang *et al.* [63] which uses only few user segmented two-dimensional images to reconstruct a three-dimensional metal object. The following method leaves behind user interaction and therefore use more 2D images to compensate.

3.1. Problems

There are several methods to perform the segmentation of metal objects in CT. In the beginning the segmentation was completely left to the health personnel, which must mark the objects in the reconstructed images (cp. [12]). Shortly after, threshold classifiers operating on the recorded integral of attenuation were introduced (cp. [25]).

Due to the integral of the attenuation coefficients it is hard to decide wether a high value comes due to high attenuation coefficients or due to the great distance inside the human body. In fig. 3.1 a single image of scan 3 (cp. chap. 2.3) is shown. To focus on the contrast problem the image is pseudo colored. It can easily be seen, that a simple threshold cannot separate the metal object - which is colored from pink to white - from the human body, which values are in the same range.

It is better to reconstruct the information and segment in the target domain as in Yazdia, Gingras and Beaulieu [61]. After the reconstruction, the values

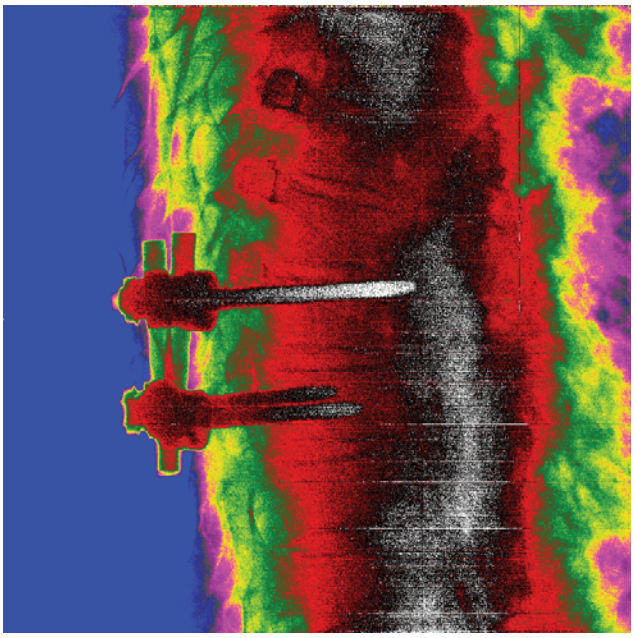

Figure 3.1.: This detail shows the difficulty in separating metal objects with a threshold algorithm in 2D with problematic contrast due to the scan configuration.

represent the attenuation coefficient of single voxels. It will be easy to achieve a threshold above bone range which encompass the metal implants if the reconstruction will be artifact free. But because of the described artifacts (cp. chap. 1.3), which will be reduced using the segmentation, it is hard to segment large metal implants.

In fig. 3.2 the problem of metal artifacts, using the example of simulated beam hardening, is shown. A water body with different number of metal inserts is simulated. The simulation takes X-ray spectra with 100 kV tube voltage and the attenuation of iron and water into consideration. With increasing number of metal objects the amount of artifacts increase. In the mid between the two implants a shadow region can be recognized. After inserting a third object in middle of the whole phantom the metal artifacts get intense enough, that the metal object is extensively corrupted.

If the three metal objects were replaced by one big object, the same effects occur, and the object begins to annihilates itself during the reconstruction.

That means the values of corrupted voxel get to smooth and the metal seems like tissue, or even air.

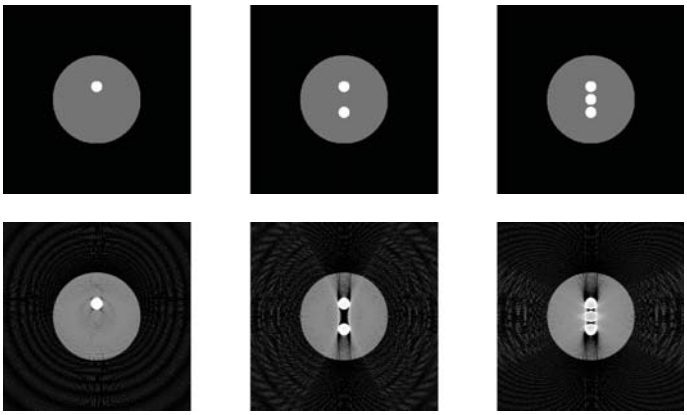

Figure 3.2.: This detail shows the effect of beam hardening. The details in upper line show slices of a phantom, made of a water sphere with different numbers of metal spheres inside. The lower line shows a simple reconstruction of these phantoms with regard of the beam hardening.

A simple threshold algorithm is not able to distinguish metal from water (or tissue), in this case. This can be seen in figure 3.3, where the false positive and false negative ratios of the 'three metal objects' case are plotted against the threshold value. Understandably with increasing threshold the amount of falsely as metal segmented pixels (denoted as false positive) decrease while the amount of pixels the segmentation process wrongly ignores (denoted as false negative) increases. One of the best thresholds in this case is 1 a.u., for this value both ratios are below 30%, another usable threshold is 0.79 a.u. here the sum of both ratios is minimal. Both results are shown in fig. 3.4, it is evident that both segmentations were not ideal.

To solve this problem another method, needing a user input in some of the 2D images, from which the 3D segmentation can be reconstructed, is proposed by Zhang *et al.* [63].

Based on all these ideas, a new segmentation method is presented, which gets considerable good results for different kinds of metal objects.

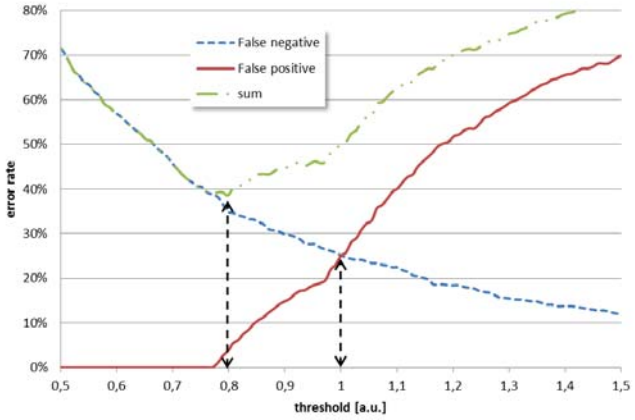

Figure 3.3.: Using the reconstruction of the case with three metal spheres, a segmentation using a simple threshold algorithm was applied. For each threshold value (plotted in arbitrary units) the ratio of false positive respectively false negative segmented pixel and the sum of both ratios is shown. Two possible threshold values are marked.

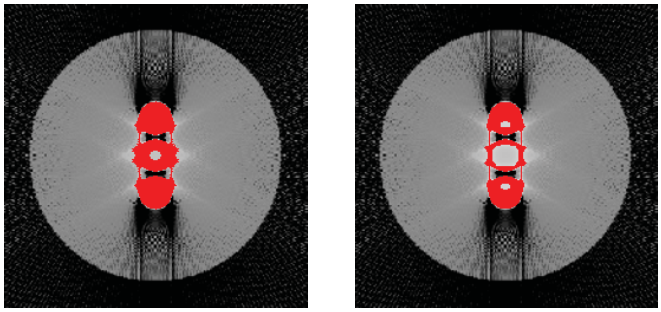

Figure 3.4.: These images show two possible results (cp. fig. 3.3) of a simple threshold segmentation of the data in fig. 3.2 (Left 0.79 a.u., right 1 a.u.). The segmented pixels were marked red.

3.2. Projective segmentation

The aim of this algorithm (named 'projective segmentation') is to classify the metal implants in a two-dimensional X-ray series. To make the process clearer the different steps were presented at an example. Therefore the single

2D image from scan case 3, which is already used above (cp. fig. 3.1) is used again.

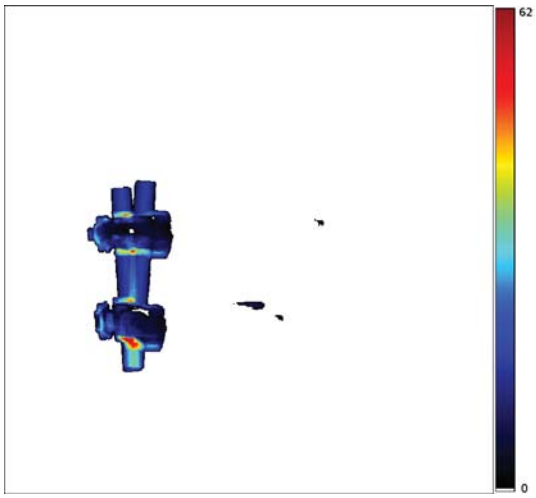

Figure 3.5.: In this figure the forward projection of the coarse segmentation is presented, the values represent the number of segmented voxels an X-ray beam traverse. To ease the visibility a special colormap is used, a value of 0 is represented by white, the other colors stand for 1 (black) to 62 (dark red) traversed voxels.

The first step for this, is a standard reconstruction of the 2D series and a coarse threshold segmentation with a threshold value high enough that definitely no false positive pixels were classified. To be sure, that no artifacts outside of the FOV will be classified, the area outside the FOV is ignored. This three-dimensional pre-segmentation $\tilde{M}(\mathbf{r})$ is forward projected using the projection geometry in the original 2D space (see fig. 3.5).

This projected information $\tilde{M}_{fp}(u,v)_\xi$ is used to generate a pre-segmentation in 2D. It must be kept in mind that $\tilde{M}_{fp}(u,v)_\xi$ is an image and not a set of coordinates as M_ξ in eq. 2.7. To gain the pre-segmentation the image is transferred in a binary image with:

$$\hat{M}(u,v)_\xi = \begin{cases} 0 & \text{if } \tilde{M}_{fp}(u,v)_\xi = 0, \\ 1 & \text{otherwise.} \end{cases} \tag{3.1}$$

To assure that no false positive classified pixels exist at the border of the pre-

segmentation, an erosion (cp. chap. 1.4.3) by a square with an edge length of 8 pixel is performed, the result is denoted as $\hat{M}'(u,v)_\xi$ and shown in figure 3.6.

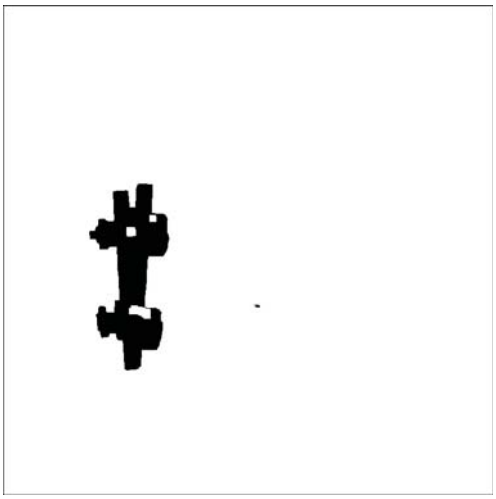

Figure 3.6.: After a erosion by a square with an edge length of 8 pixel parts of the pre-segmented areas completely disappear, because they were to small.(Black=true, white=false)

This image will help in the further segmentation process. To proceed, the original image $I(u,v)_\xi$ is denoised using the bilateral filter I_F (see eq. 1.21) with $\sigma_D = 3$ and $\sigma_R = 150$, the result is shown in fig. 3.7.

$$\hat{I}(u,v)_\xi = (I(u,v)_\xi * I_F) \tag{3.2}$$

To get a reference for each pixel on the image in which value range another pixel inside the metal object will lie, the image is tesselated using $\hat{M}'(u,v)_\xi$. For every pixel p_i with coordinates (u_i, v_i) outside the marked area of $\hat{M}'(u,v)_\xi$ (with $\hat{M}'(u_i,v_i)_\xi = 0$), the next marked pixel p_m (with $\hat{M}'(u_m,v_m)_\xi = 1$) is determined and the value of this pixel is stored in a map $V(u_i,v_i)_\xi = \hat{I}(u_m,v_m)_\xi$. The result, seen in figure 3.8, is a variant of a Voronoi tessellation.

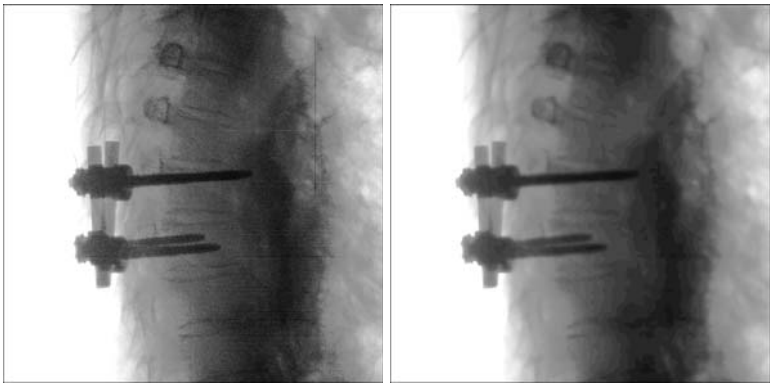

Figure 3.7.: The showed detail before and after the described bilateral filter. The images are windowed and a nonlinear transformation function is used to enhance the contrast.

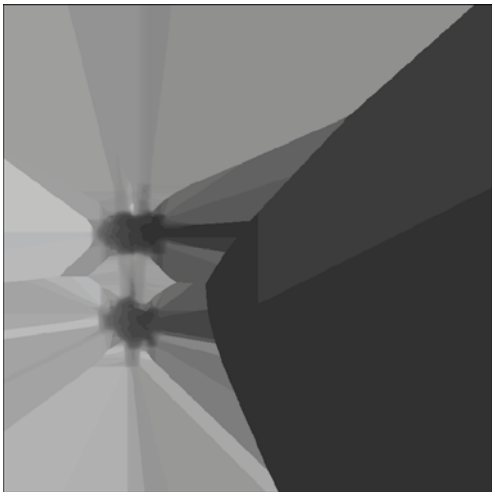

Figure 3.8.: In this detail, all pixels outside the areas marked in fig. 3.6 gets a new value determined by the nearest marked pixel.

To regard edges and noise in the images, the standard deviation in a quadratic area with an edge length of $2m + 1$ pixels centered on the interested pixel is computed (with $m = 10$) and stored in a local standard deviation map $\hat{S}(u, v)_\xi$.

$$S(u,v)_\xi = \left[\frac{1}{(2m+1)^2 - 1} \sum_{i=u-m}^{u+m} \sum_{j=v-m}^{v+m} \left[\hat{I}(i,j)_\xi - E_m \left(\hat{I}(u,v)_\xi \right) \right] \right]^{\frac{1}{2}} \tag{3.3}$$

with the mean:

$$E_m \left(\hat{I}(u,v)_\xi \right) = \frac{1}{(2m+1)^2} \sum_{k=u-m}^{u+m} \sum_{l=v-m}^{v+m} \left(\hat{I}(k,l)_\xi \right) \tag{3.4}$$

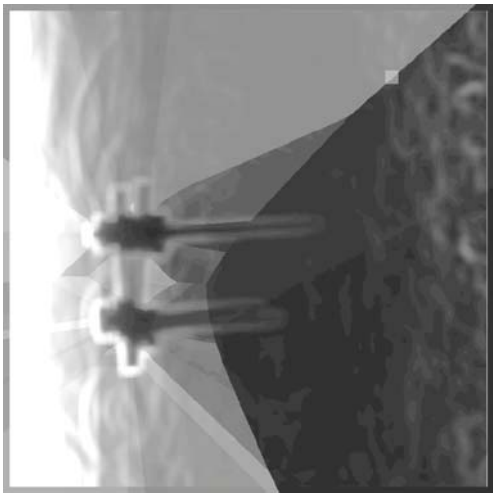

Figure 3.9.: After the combination of the Voronoi tessellation and 1.3 times the standard deviation this local threshold is gained.

With these two maps a new local threshold is generated, which covers at least 90% of normal distributed noise (the normalized cumulative sum of a normal distribution reaches 0.9 at 1.28 standard deviations, 1.3 is used here which covers 90.4%). The result is displayed in figure 3.9.

$$T(u,v)_\xi = V(u,v)_\xi + 1.3 S(u,v)_\xi \tag{3.5}$$

Figure 3.10.: This image shows the pre-result (black=true, white=false), obtained by applying the computed threshold (eq. 3.6) on fig. 3.7

Now this threshold is applied on the denoised data. The result is presented in figure 3.10 and has a lot of artifacts. It is not necessary that this image, which is one of the worst examples in the series, is in a much better quality. The next steps reduce these generated new artifacts.

$$R(u,v)_\xi = \hat{I}(u_m, v_m)_\xi < T(u,v)_\xi \tag{3.6}$$

To begin with the next step it is inevitable to perform the steps before to all images of the series, then a simplified back projection is used to obtain three dimensional information of possible metal voxels.

The difference between the FBP and the simplified back projection is the absence of a filter step. Every segmented image $R(u,v)_\xi$ is projected using the original geometry. Thereby a volume is generated whose voxel values $P_1(\mathbf{r})$ represent the number of angle positions ξ in which $R(u,v)_\xi$ is positive at the end of the ray path $l_{(u,v)_\xi}$ passing $\mathbf{r}$. The value of the voxels in $P_1(\mathbf{r})$ indicate the number of images which 'think' the voxel $\mathbf{r}$ is lying in front, behind or in mid of a metal object. The index 1 is of interest later.

In figure 3.11 a simple back projection (also called simple reconstruction) is seen. The shown slice, was chosen so that it can be compared with the figures above. The artifacts of the pre-segmentation can be seen, but the intensity of these artifacts is small against the one of the object of interest. The next

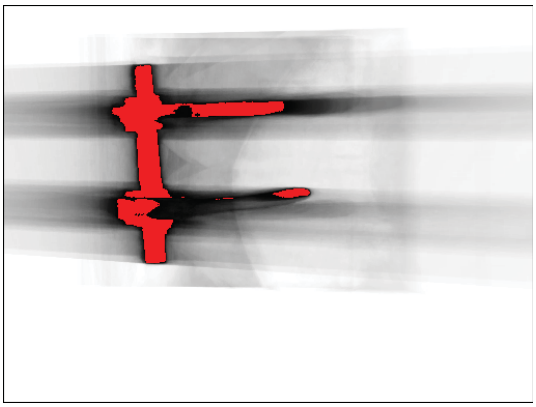

Figure 3.11.: This detail shows a slice of the result of a simple reconstruction, the blacker the higher value, all values with more than or equal to 195 ($0.975n$ where n is the number of scan angels) are marked red.

step is a simple threshold in the volume, all voxels with a value of more than or equal to 97,5% of the number of scan angles were set to 1 every other to 0.

$$\hat{P}_1(\mathbf{r}) = \begin{cases} 1 & \text{if } P_1(\mathbf{r}) \geq 0.975n, \\ 0 & \text{otherwise.} \end{cases} \tag{3.7}$$

A forward projection of $\tilde{P}_1(\mathbf{r})$ (denoted $\tilde{P}_{1FP}(u,v)_\xi$) gives a new and better estimation of pixels representing metal objects as $\tilde{M}_{fp}(u,v)_\xi$ before, as can be seen in figure 3.12.

Now the steps above are repeated, from $\tilde{P}_{1FP}(u,v)_\xi$ $\hat{P}_{1FP}(u,v)_\xi$ is gained, and with it a new $V(u_i,v_i)_\xi$, $T(u,v)_\xi$, $R(u,v)_\xi$, $P_2(\mathbf{r})$ and at the end a new $\tilde{P}_{2FP}(u,v)_\xi$. This is repeated, with increasing index. To get a break condition, be $\tilde{P}_{0FP}(u,v)_\xi$=$\tilde{M}_{fp}(u,v)_\xi$, and after each iteration step i the following ratio is computed:

$$r_i = \frac{\tilde{P}_{iFP}(u,v)_\xi - \tilde{P_{i-1}}_{FP}(u,v)_\xi}{\tilde{P}_{0FP}(u,v)_\xi} \tag{3.8}$$

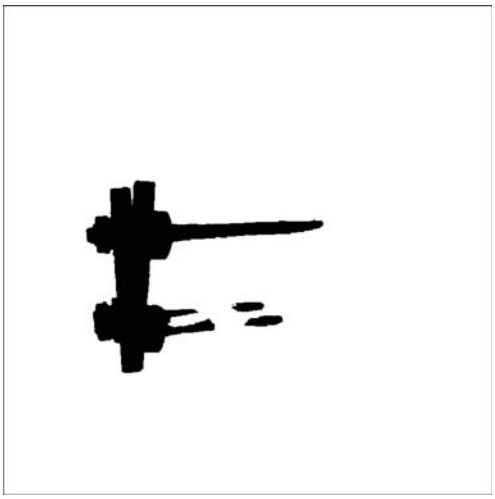

Figure 3.12.: After the forward projection a better estimation of the metal object is obtained (cp. with fig. 3.5).

If the ratio r_i is not increasing more than a certain value (in the present cases a threshold of 0.02 is used) or even decreasing the iteration process is terminated and a AND combination of the last result and the beginning $\tilde{M}_{fp}(u,v)_\xi$ is given back as result.

$$Seg(u,v)_\xi = \tilde{M}_{fp}(u,v)_\xi \wedge \tilde{P}_{iFP}(u,v)_\xi \tag{3.9}$$

This combination takes care that at least the initial segmentation is remaining. That is necessary because small metal objects, which can be segmented sufficient with a simple threshold tend to decrease during this segmentation. In such a case the iteration terminates after the first run and at least the initial segmentation, perhaps with a few additional segmented pixels, remains.

An acceleration of the algorithm can be obtained if the whole process is only computed in a ROI in which the metal objects are expected. These ROI can be received by the result of the simple threshold $\tilde{M}_{fp}(u,v)_\xi$, because the heavily disturbing artifacts protrude inside the metal implants and not at the edge.

An even bigger acceleration can be achieved if the whole segmentation is calculated on images and volumes of reduced size. With the known geometry it is a simple step to reconstruct a volume with an eighth of the original volume. It is also no problem to reduce the two-dimensional images to one

fourth of their size for this algorithm. Only at the end the last reconstruction must be in original size to get a useful result.

3.3. Reliability

A further result of this method is a reliability value for each voxel of the reconstructed volume. It is gained by making a last simple reconstruction on the last combined result of the algorithm above. After that simple back projection a volume is obtained in which every voxels gains a value that states in how many of the scan angles the information used for the FBP is disturbed due to a transit of metal implants. Every voxel with a value of zero is totaly undisturbed and every voxel with a value of n is in all angles behind a metal object and therefore for this scanning geometry it is as bad as a metal voxel itself, because no real undisturbed information can be used for reconstruction.

This information can be shown to the medical personnel to indicate areas which are difficult to diagnose either with or without MAR. A possible display is shown in chapter 3.4.

The sum of the local reliability can give an overall quality information, which indicates how good a scan of that part of body with the distinct metal implants is, due to the scan geometry. Using a different position or angulation between patient and scanner results in a better (or worse) global reliability, with a priori information and a simulation the perfect position and angulation, under certain conditions given by several mechanic restrictions, can be obtained. With that information improved CT imaging quality can be gained at the beginning of the image processing chain. More detailed research in this case is necessary but not part of this work, the idea is patent pending.

Another improvement due to the reliability is a modified version of the replacement (cp. chap. 2.2.2). This variation replaces not only the 'air inclusions' and metal implants, but modifies areas according to their reliability also. For this, additional to the metal and 'air inclusion' segmentation the reliability values and a simple classifier which voxel is inside the human body and which outside is necessary. This classifier can be obtain by a simple thresholding of the reconstruction ($B_1(\mathbf{r})$).

$$B_1(\mathbf{r}) = \begin{cases} 1 & \text{if } V(\mathbf{r}) > -550\,\text{HU}, \\ 0 & \text{otherwise.} \end{cases} \tag{3.10}$$

But due to shadow artifacts at the edge of the human body false negative seg-

mented areas can protrude. To reduce these areas, a simple thresholding (via Otsu's method [37] or basic global thresholding [13]) in the two-dimensional series, to classify body versus air, is applied. Then a simple reconstruction (see above) with a threshold of $0.975n$ gives a good estimation of the human body inside the FOV ($B_2(\mathbf{r})$). This result is combined with $B_1(\mathbf{r})$:

$$B(\mathbf{r}) = B_1(\mathbf{r}) \wedge B_2(\mathbf{r}) \tag{3.11}$$

Now a coarse class model $\hat{B}(\mathbf{r})$ is achieved with a value of $-40\,\mathrm{HU}$ for the tissue part and a value of $-1000\,\mathrm{HU}$ for outside.

$$\hat{B}(\mathbf{r}) = \begin{cases} -40 & \text{if } B(\mathbf{r}) = 1, \\ -1000 & \text{otherwise.} \end{cases} \tag{3.12}$$

With this information a new replacement $\hat{R}(\mathbf{r})$ is gained:

$$\hat{R}(\mathbf{r}) = [D(\mathbf{r}) - 1]V(\mathbf{r}) + D(\mathbf{r})\hat{B}(\mathbf{r}) \tag{3.13}$$

$$D(\mathbf{r}) = \max\left(\frac{C(\mathbf{r})}{0.9n} + A(\mathbf{r}) + \tilde{M}(\mathbf{r}); 1\right) \tag{3.14}$$

where $A(\mathbf{r})$ is a binary 'air inclusion' volume, $C(\mathbf{r})$ is the local reliability value (which differs from 0 to n) and $\tilde{M}(\mathbf{r})$ is the initial segmentation. The marked voxels in the binary volumes of 'air inclusion' and metal segmentation must be replaced completely. This is also true for every voxel with a reliability of less than 10%. All other voxels will be replaced by a linear combination between the original value and the coarse tissue model depending on the reliability.

This replacement is already used in the algorithm described in the chapter before (cp. chap. 2.2.2).

3.4. Results

Several different data sets (the same as in chapter 2.3) were segmented with the new segmentation algorithm. For one of the most difficult scans (case 3) a comparison between a simple thresholding, the projective and a manual segmentation was applied. The series first was 'perfectly' segmented by a human, then several simple thresholds were tried.

The ratio of false positives and false negatives is presented in figures 3.13 and 3.14, the figures show the results of using a definite threshold in the three-dimensional volume to classify and then forward project the classified voxels. After the projection another threshold is used to define how much voxels, classified in 3D, which are lying on an X-ray beam hitting a target pixel, are necessary that this pixel is marked as metal.

For the first figure (fig. 3.13) this second threshold is 1, so every classified voxel is represented in the 2D segmentation, in figure 3.14 only pixels which stand for more than 5 voxels are counted. In the figures not only the mean error rates, but also an additional of one standard deviation (StD) is shown.

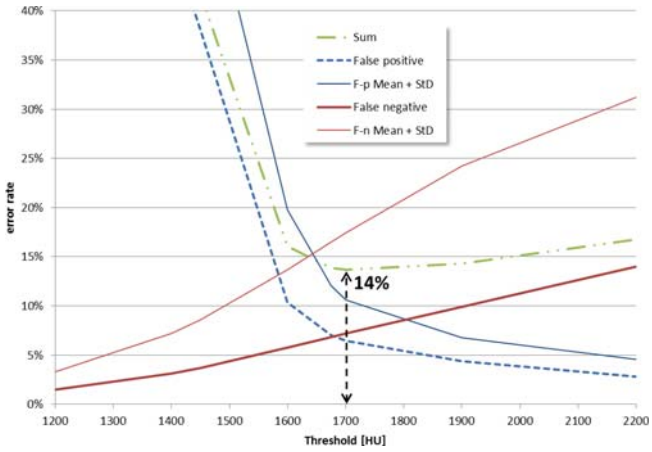

Figure 3.13.: In this figure the mean of the false positive (blue) and false negative (red) ratios from scan 3 (cp. chap. 2.3), using a simple 3D thresholding, are displayed. Additional the distance of one standard deviation and the sum of the error rates are shown.

As can be seen, the best segmentation is the one with a threshold of 1600 HU and the constraint of a minimum of 6 voxels on the beam, in this case this results in a sum of the error of 13%.

The false positive ratio of the projective algorithm is about 1% with a StD of 1.6% and the false negative ratio is 0.8% with a StD of 1.4%, that makes a total sum of 1.8% and therefore it is 7 times better than the simple thresholding!

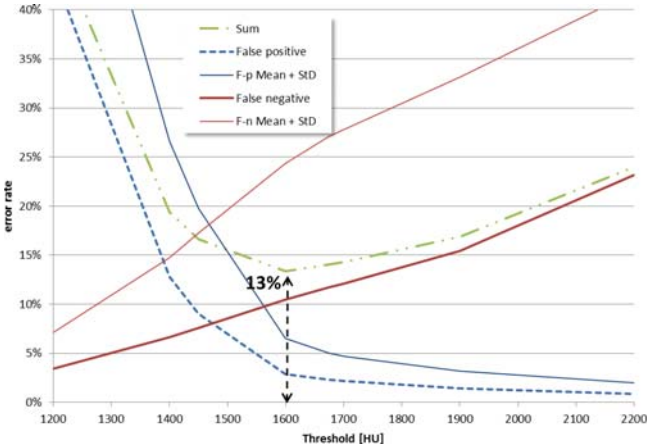

Figure 3.14.: In this figure the mean of the false positive (blue) and false negative (red) ratios from scan 3 (cp. chap. 2.3), using a simple 3D thresholding with at least 6 classified voxels on an X-ray beam (see above), are displayed. Additional the distance of one standard deviation and the sum of the error rates are shown.

In the following the results of the already described cases (cp. chap.. 2.3) are shown from different angles.

In one of the four cases (see fig. 3.15) the new algorithm is absolutely necessary, because the metal artifacts disturb the reconstruction due to a big implant more than in the other cases. In one other (see fig. 3.16) a slight improvement can be seen, which is due to the fact that the initial segmentation ignores metal outside of the FOV. And in the last two cases (see fig. 3.17 and fig. 3.18) the new algorithm is not necessary but it generates no artifacts. If a detailed comparison is made the new algorithm classifies a few more pixels at the border or at one side of the implants.

A data set very similar to case 3 but with worse contrast is also segmented sufficiently. This data set is not presented here because the results are more or less identical to case 3. But this data was recorded a few years ago with a less improved C-arm CT prototype and in this case the newer data from case 3 is more relevant.

The segmentation is very robust in case of the different parameters which must be adjusted, changes of more than 30% did not change the result in a problematic manner.

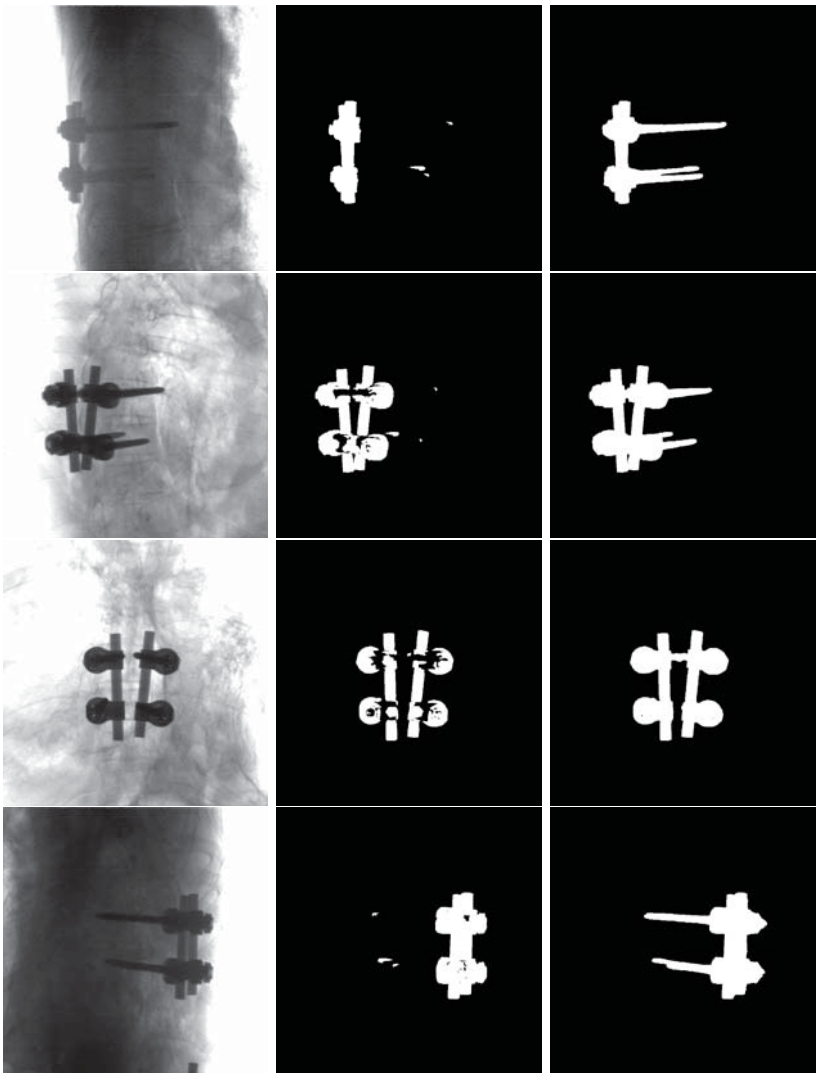

Figure 3.15.: Here the 13th, 58th, 111th and 176th image of case 3 are shown. On the left the respective original image (windowed to see the interesting parts), in the middle the initial metal segmentation, and on the right the result of the new algorithm is shown. A large improvement can be seen.

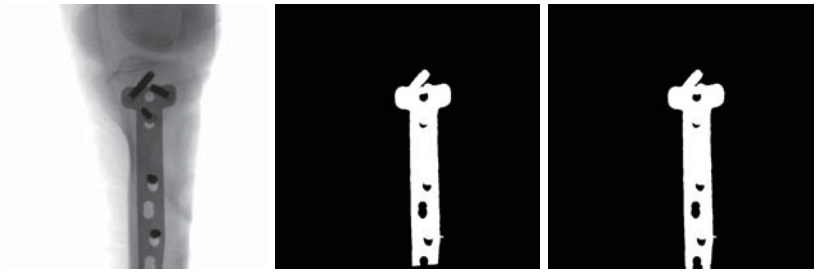

Figure 3.16.: Here the 61th image of case 4 is shown. On the left the respective original image (windowed to see the interesting parts), in the middle the initial metal segmentation, and on the right the result of the new algorithm is shown. Only on the bottom of the metal implant a slight improvement can be seen at first sight, the lack of this part in the initial segmentation is due to the fact, that this part leaves the FOV and therefore is not segmented in the initial segmentation. If a detailed comparison is made, a small enlargement of the initial segmentation is visible around the implant.

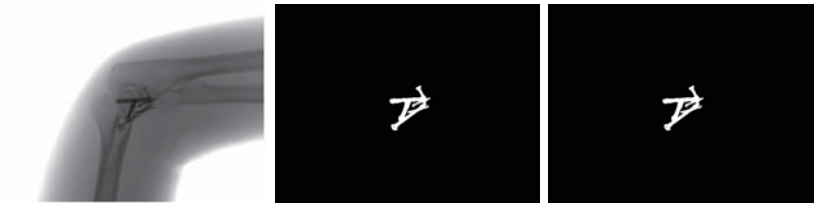

Figure 3.17.: Here the 144th image of case 1 is shown. On the left the respective original image (windowed to see the interesting parts), in the middle the initial metal segmentation, and on the right the result of the new algorithm is shown. No improvement can be seen at first sight, but also no artifacts arise. If a detailed comparison is made, a small enlargement of the initial segmentation is visible at one side of the implants.

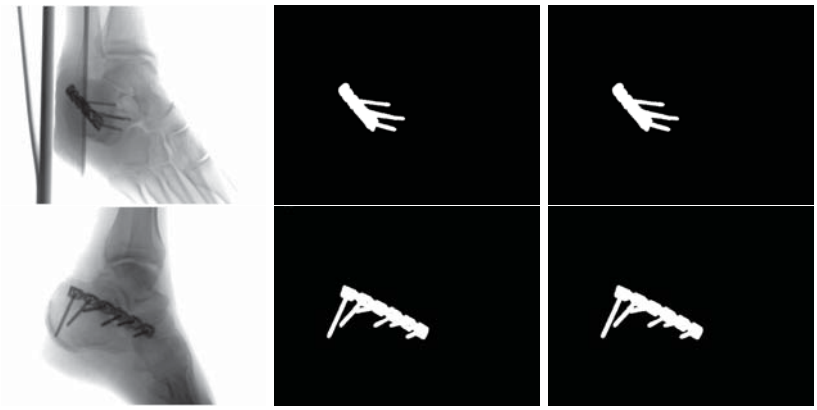

Figure 3.18.: Here the first and the 90th image of case 1 are shown. On the left the respective original image (windowed to see the interesting parts), in the middle the initial metal segmentation, and on the right the result of the new algorithm is shown. No improvement can be seen at first sight, but also no artifacts arise. If a detailed comparison is made, a small enlargement of the initial segmentation is visible around the implant.

Improvements due to reliability

As mentioned before another way to display the reconstruction can be obtained by using the reliability information. In the following a simple display is proposed. This proposal is not verified or discussed by medical personnel and will only show a part of the potential and explain some of the problems, which appear in the results of the MAR algorithm (cp. chap.. 2.3). For this case a sample of the same images as in the result chapter of the MAR is used.

The initial segmentation is marked yellow while the reliability is marked red. A total red voxel means the reliability is worse than 2.5% (less than 10 scan angles yield undisturbed information), while the color shift of the gray value is an indicator for the unreliability from 100% (no red shift) to 2.5% (total red shift).

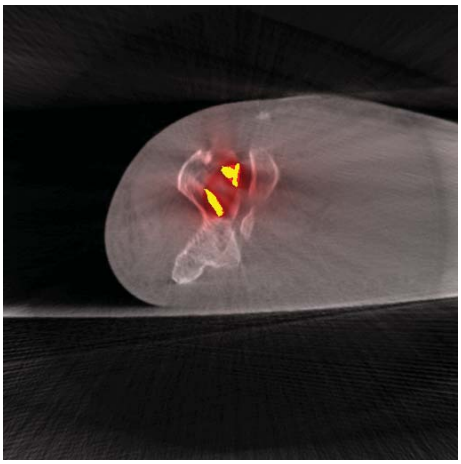

Figure 3.19.: Scan 1 : This detail shows the slice crossing the elbow joint as in fig. 2.14. (Windowed from −1000 HU to 1000 HU). Only a slight unreliability is present in this slice.

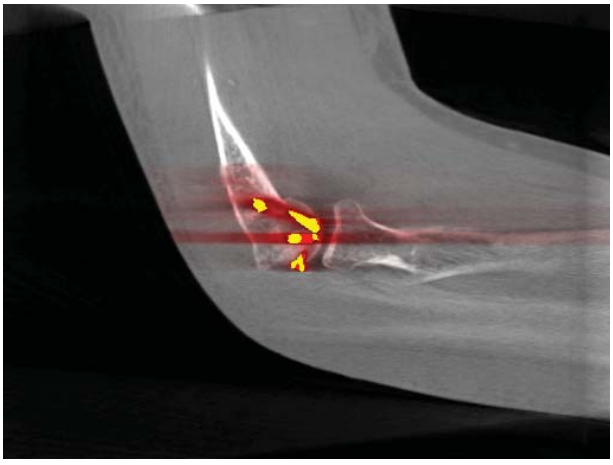

Figure 3.20.: Scan 1 : This detail shows the slice crossing the elbow joint as in fig. 2.15. In this image the slight blurring of the humerus edge is explained by the unreliability of this part of the slice (cp. fig. 2.15). (Windowed from −1000 HU to 1000 HU).

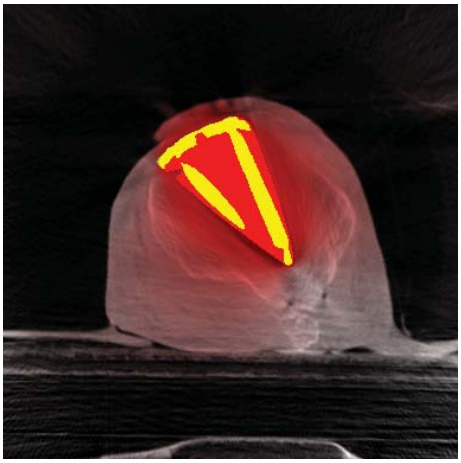

Figure 3.21.: Scan 4 : This detail shows the knee joint as shown in fig. 2.23. Here the difference between the initial segmentation and the unreliability is seen. Because of the bad position of the scanning device, the transversal plane of this scan suffers from a big unreliability which is reflected in the blurring. (Windowed from −1000 HU to 1000 HU).

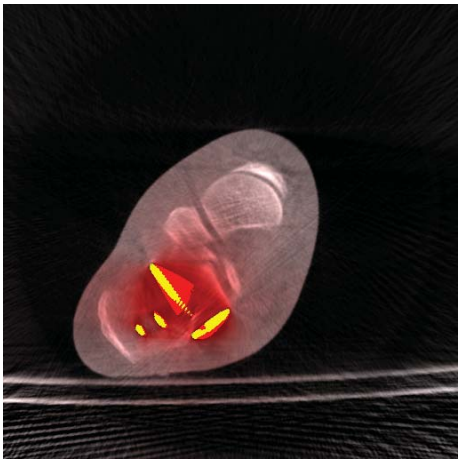

Figure 3.22.: Scan 2 : This detail shows the right heel as shown in fig. 2.24. Here the difference between the initial segmentation and the unreliability is seen. Due to the number of several metal implants the area in between is rather high unreliable, which corresponds with the blurring. (Windowed from −1000 HU to 1000 HU).

Discussion and outlook

A new algorithm which is capable of correcting CBCT images from a mobile C-arm CT using a advanced segmentation and giving more information about the reliability was developed during this work. This includes several correction steps necessary to compensate problems occurring during the process.

These problems, like segmentation, truncation, misalignment and replacement of artifacts, are solved in an acceptable way, though more investigation is needed.

The idea of using pre-reconstructed information which is obtained by other scan angles has large potential. Using information from other directions without complex reconfiguring or modifying the reconstruction algorithm allows a easy implementation in existing systems.

The results show a satisfying improvement, although distinct areas around larger implants are yet blurred. Other replacement methods and another iterative metal artifact reduction step will correct this blurring. For example, a tissue class modeling (see Bal and Spies [2]) combined with the current replacement is a possible next step.

To avoid discontinuous edges another idea published a few weeks ago by Meyer *et al.* [35] and Prell *et al.* [39] can replace or upgrade the simple adjustment of the edges (explained in chap.. 2.2.5).

One of the largest bottlenecks, a satisfying segmentation of large metal objects with lots of artifacts is also presented. The segmentation expand the existing ones and shows a robust and reliable result.

But also in this part further research will be applied. In fact, during the last weeks of the work another segmentation idea using mean-shift techniques (cp. [5, 6, 62]) was found in literature, e.g in the work of Yu *et al.* [62]. An implementation of a mean-shift segmentation to gain $R(u,v)_\xi$ in chapter 3.2 can improve the segmentation process. A short one-day-test of the mean-shift algorithm shows high potential, but more research is needed to combine the mean-shift algorithm with the presented projective-segmentation.

During the new segmentation step, further information, giving a value of reliability of a definite voxel, is available and helps the health personnel to identify

problematic areas and to train better scanning positions. The display of these information must be adjusted to the wishes of the health personnel and the constraints in the hospitals.

Further applications to other CT devices can be applied and distinct tests of the algorithm, for example with before and after comparison of data, e.g. from the cadaver study, will be investigated in detail.

A. Stitching of 2D X-ray images

During the beginning of the work on the MAR algorithm a proof of concept of a stitching of two-dimensional X-ray images was made. The aim of this method was to enlarge the image size without building a bigger detector and therefore without increasing the costs. Basic information about stitching can be read in Szeliski [52]. An important constraint of this proof of concept was the fact, that the series will be fused without additional extrinsic information.

Due to the fact, that this was a very short survey, only a short overview is given. For a detailed report more analysis must be done.

A.1. Image acquisition

For this proof two image series were acquired, using the C-14 prototype and a movable table. A long bone phantom and a chest phantom were positioned on the table and then moved during the scan. Because almost every parts of the target area appears on more than one image the dose is higher. To reduce this effect low dose scans (fluoroscopic X-ray images) were made. Some parts of the resulting loss in image quality will be regained during the fusing of the images.

As example for the raw data the long bone series is presented in figure A.1.

A.2. Method

Stitching of X-ray images using extrinsic information like a grid or a ruler is common and amongst other published in [15, 59, 60]. An image registration of X-ray images only using intrinsic information is more complicated and almost no literature was found at this subject. Most articles of intrinsic registration and stitching were about digital photographs of natural panoramas.

A first idea was to use mutual information for the registration. Because the images are very angle-constant a simple translation in two dimension was

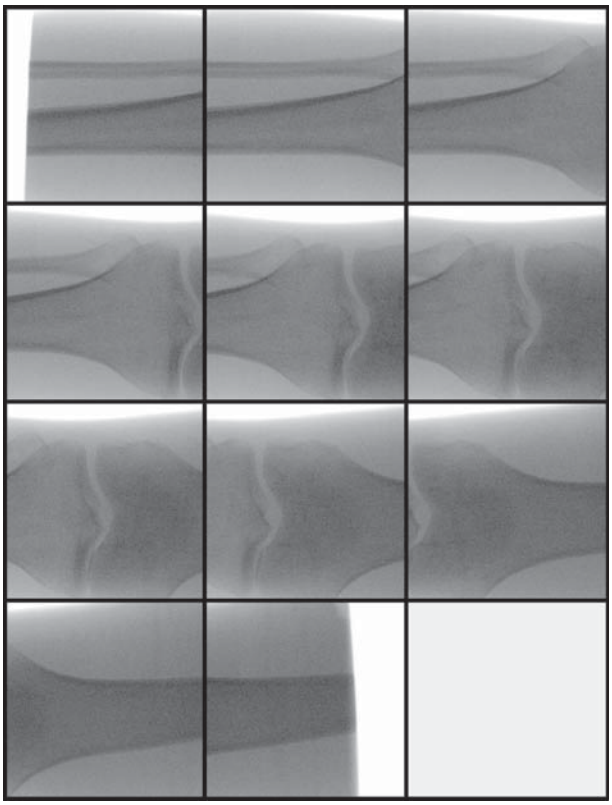

Figure A.1.: These 11 images show the parts of the long bone phantom which will be stitched together. The single images show a high amount of noise due to the fluoroscopic imaging.

sufficient. Using the already described algorithm 2.2.3 one image is stitched to another, then a simple averaging of the images was applied. After that, the next image is realigned, stitched and averaged and so on.

Different complex fusion algorithm can be used, but a simple averaging showed to be enough for the short survey of this problem.

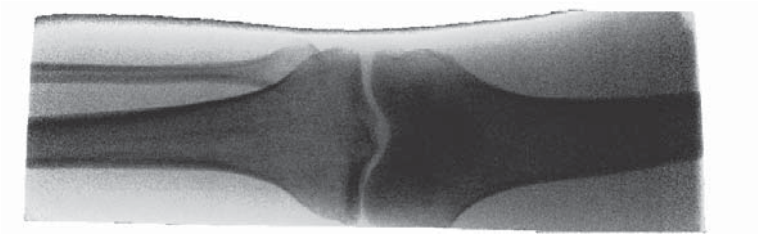

Figure A.2.: This figure shows the result of the stitching of the long bone phantom seen in figure A.1.

A.3. Results

It can be seen, that the realignment alone from intrinsic information is satisfying and averaging is a good beginning for the fusion as can be seen in figure A.2. But if the part of the body is getting larger, a problem arises from the parallax between the images. To reduce this effect only few images can be used for fusion and therefore more noise remains in the stitched image.

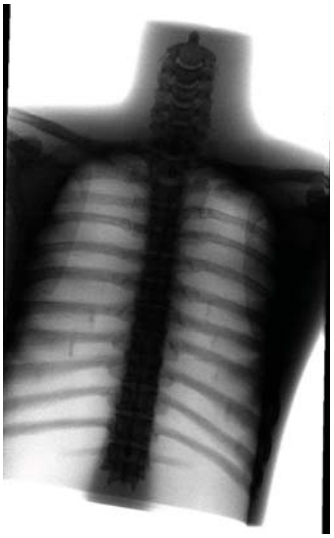

Figure A.3.: This figure shows the result of the stitching of a chest phantom. Due to the parallax fewer images can be used for the fusion of a single part and therefore more noise remains.

A.4. Outlook and Discussion

During the few weeks, while this proof of concept was performed, it can be seen that an intrinsic registration of X-ray images is possible using a mutual information criterium. This outcome was very useful for the further research on the MAR algorithm. Further it can be seen, that a simple fusion algorithm is a good beginning but more investigation is necessary. In particular the parallax problem during the fusing of larger parts of the body must be reduced. A more complicated, affine or projective registration (cp. [52]) will solve this issue. For the future also three-dimensional stitching can be interesting.

B. Hounsfield scale

Sir Godfrey Newbold Hounsfield was a engineer who shared 1979 the Nobel Prize for Physiology or Medicine with Allan McLeod Cormack for his part in developing X-ray computed tomography.

Figure B.1.: Sir Godfrey Newbold Hounsfield was a fellow of the royal-society and a commander of the British Empire
Source: Wells [58]

He introduced an up to today important scale, denoted as Hounsfield Scale using the so called Hounsfield Units HU, which should be introduced in this chapter.

For a material with a linear X-ray attenuation coefficient μ the corresponding value a_{HU} in HU is given by:

$$a_{HU} = 1000 \frac{\mu - \mu_{water}}{\mu_{water} - \mu_{air}} \tag{B.1}$$

with μ_{water} and μ_{air} as the linear X-ray attenuation coefficients of water and

air, under the same conditions (tube voltage, anode material and so on).

Due to this scaling the Hounsfield equivalent of water respectively air is zero and minus one thousand. Average values of other materials are (cp. fig. B.2):

- Bone above 400 HU
- Fat about −70 HU
- Tissue about 40 HU

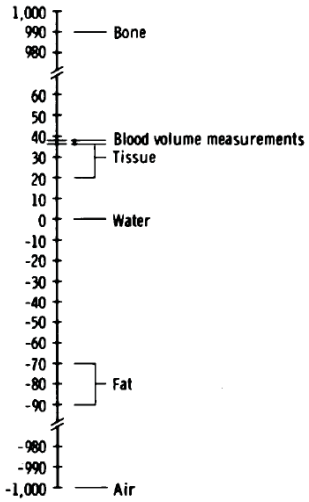

Figure B.2.: Hounsfield scale as presented by Hounsfield in 1980
Source: Hounsfield [16]

The scale is widely-used in CT imaging, due to its easy handling.

List of Figures

Bibliography

[1] Alvarez, R. and Stonestrom, J. 'Optimal Processing of Computed Tomography Images Using Experimentally Measured Noise Properties.' *J. Comput. Assist. Tomo.*, **3** (1):77–84, 1979.

[2] Bal, M. and Spies, L. 'Metal artifact reduction in CT using tissue-class modeling and adaptive prefiltering.' *Medical Physics*, **33** (8):2852–2859, 2006.

[3] Bracewell, R. and Riddle, A. 'Inversion of fan beam scans in radio astronomy.' *Astrophysics Journal*, **150**:427 – 434, 1967.

[4] Brooks, R. and Di Chiro, G. 'Beam Hardening in X-ray Reconstructive Tomography.' *Phys. Med. Biol.*, **21** (3):390–398, 1976.

[5] Cheng, Y. 'Mean Shift, Mode Seeking, and Clustering.' *IEEE Trans. Pat. Anal. Mach. Int.*, **17** (8):790–799, 1995.

[6] Comaniciu, D. and Meer, P. 'Mean Shift: A Robust Approach Toward Feature Space Analysis.' *IEEE Trans. Pat. Anal. Mach. Int.*, **24** (5):603–619, 2002.

[7] De Man, B., Nuyts, J., Dupont, P., Marchal, G. and Suetens, P. 'Metal Streak Artifacts in X-ray Computed Tomography: A Simulation Study.' *IEEE Transactions on Nuclear Science*, **46** (3):691–696, 1999.

[8] Dreike, P. and Boyd, D. 'Convolution reconstruction of fan beam projections.' **5** (4):459–469, 1976.

[9] Duerinckx, A. and Macovski, A. 'Nonlinear polychromatic and noise artifacts in X-ray computed tomography images.' *J. Comput. Assist. Tomo.*, **3** (4):519–526, 1979.

[10] Feldkamp, L.A., Davis, L.C. and Kress, J.W. 'Practical cone-beam algorithm.' *J. Opt. Soc. Am. A*, **1** (6):612–619, 1984.

[11] Glover, G. 'Compton scatter effects in CT reconstructions.' *Med. Phys.*, **9** (6):860–867, 1982.

[12] Glover, G. and Pelc, N. 'An algorithm for the reduction of metal clip artifacts in CT reconstructions.' *Medical Physics*, **8** (6):799–807, 1981.

[13] Gonzales, R. and Woods, R. *Digital Image Processing*. Pearson Prentice Hall, 3 edition, 2008.

[14] Gonzales, R., Woods, R. and Eddins, S. *Digital Image Processing using Matlab*. Pearson Prentice Hall, 2004.

[15] Gooßen, A., Schlüter, M., Pralow, T. and Grigat, R. 'A Stitching Algorithm for Automatic Registration of Digital Radiographs.' In A. Campilho and M. Kamel (Editors), *ICIAR 2008, LNCS 5112*, pages 854–862. Springer-Verlag Berlin Heidelberg, 2008.

[16] Hounsfield, G. 'Computed medical imaging.' *Med. Phys.*, **7** (4):283–290, 1980.

[17] in Deutschland, A.B.K. *Krebs in Deutschland. 4. überarbeitete, aktualisierte Ausgabe*. Saarbrücken, 4 edition, 2004.

[18] Jähne, B. *Digitale Bildverarbeitung*. Springer, 3 edition, 1993.

[19] James, A. 'Computerized transverse axial scanning (tomography): Part2. Clinical application.' *British Journal of Radiology*, **46** (552):1023–1047, 1973.

[20] Joseph, P. 'The effects of scatter in X-ray computed tomography.' *Med. Phys.*, **9** (4):464–472, 1982.

[21] Joseph, P. and Schulz, R. 'View Sampling requirements in fan beam computed tomography.' *Med. Phys.*, **7** (6):692–702, 1980.

[22] Joseph, P. and Spital, R. 'The exponential edge-gradient effect in X-ray computed tomography.' *Phys. Med. Biol.*, **26** (3):473–487, 1981.

[23] Joseph, P., Spital, R. and Stockham, C. 'The Effects of Sampling on CT Images.' *Comp. Tomo.*, **4**:189–206, 1980.

[24] Kalender, W. *Computed Tomography: Fundamentals, System Technology, Image Quality, Applications*. Wiley, 2009.

[25] Kalender, W., Hebele, R. and Ebersberger, J. 'Reduction of CT artifacts caused by metallic implants.' *Radiology*, **164** (2):567–577, 1987.

[26] Kennedy, J., Israel, O., Frenkel, A., Bar-Shalom, R. and Azhari, H. 'The reduction of artifacts due to metal hip implants in CT-attenuation corrected PET images from hybrid PET/CT scanners.' *Med Biol Eng Comput*, **45**:553–562, 2007.

[27] Kulenkampff, H. and Schmidt, L. 'Die Energieverteilung im Spektrum der Röntgenbremsstrahlung.' *Annalen der Physik*, **43** (5):494–512, 1943.

[28] Lemmens, C., Faul, D., Hamill, J., Stroobants, S. and Nuyts, J. 'Suppression of metal streak artifacts in CT using a MAP reconstruction procedure.' In *Nucl. Sci. Symp. Conf. Rec. 2006. IEEE*, pages 3431–3437. 2006.

[29] Lemmens, C., Faul, D. and Nuyts, J. 'Suppression of Metal Artifacts in CT Using a Reconstruction Procedure That Combines MAP and Projection Completion.' *IEEE Trans. Med. Imag.*, **28** (2):250–260, 2009.

[30] Liechti, A. and Minder, W. *Röntgenphysik*. Springer Verlag, 2 edition, 1955.

[31] Maschauer, S. *Kalibrierung eines Röntgen-Flachbilddetektors mit zwei Dynamikbereichen*. Master's thesis, University of Passau, 2005.

[32] Meilinger, M. *Maschinelle Lernverfahren zur adaptiven, anisotropen Rauschreduzierung in 3D-Datensätzen von Röntgentomographen*. Master's thesis, University of Regensburg, 2007.

[33] Meilinger, M., Schmidgunst, C., Schütz, O. and Lang, E. 'Alignment correction during metal artifact reduction for CBCT using mutual information and edge filtering.' In P. Zinterhof, S. Lončarić, A. Uhl and A. Carini (Editors), *Proc. 6th Int. Symp. Im. Sig. Proc. Anal., 2009. ISPA 2009.*, pages 135–140. IEEE, 2009.

[34] Meilinger, M., Schmidgunst, C., Schütz, O. and Lang, E. 'Metal Artifact Reduction in CBCT Using Forward Projected Reconstruction Information and Mutual Information Realignment.' In O. Dössel and W.C. Schlegel (Editors), *World Cong. Med. Phys. Biomed. Eng., September 7 - 12, 2009, Munich, Germany*, volume 25/II of *IFMBE Proc.*, pages 46–49. Springer, 2009.

[35] Meyer, E., Raupach, R., Lell, M., Schmidt, B. and Kachelrieß, M. 'Normalized metal artifact reduction (NMAR) in computed tomography.' *Med. Phys.*, **37** (10):5482–5493, 2010.

[36] Naranjo, V., Llorens, R., Paniagua, P., Alcañiz, M. and Albalat, S. 'A New Approach in Metal Artifact Reduction for CT 3D Reconstruction.' In J.e.a. Mira (Editor), *IWINAC 2009, Part II, LNCS 5602*, pages 11–19. Springer-Verlag Berlin Heidelberg, 2009.

[37] Otsu, N. 'A threshold selection method from gray-level histograms.' *IEEE Transactions on Systems, Man and Cybernetics*, **9** (1):62–66, 1979.

[38] Parker, D.L. 'Optimal short scan convolution reconstruction for fanbeam CT.' *Med Phys*, **9** (2):254–257, 1982.

[39] Prell, D., Kyriakou, Y., Struffert, T., Dörfler, A. and Kalender, W. 'Metal Artifact Reduction for Clipping and Coiling in Interventional C-Arm CT.' *Am. J. Neuroradiol.*, **31**:634–639, 2010.

[40] Radon, J. 'Über die Bestimmung von Funktionen durch ihre integralwerte längs gewisser Mannigfaltigkeiten.' *Ber. Sächs. Akad. Wiss. Leipzig, Math. Phys. Kl.*, **69**:262–277, 1917.

[41] Ramachandran, G.N. and Lakshminarayanan, A.V. 'Three-dimensional Reconstruction from Radiographs and Electron Micrographs: Application of Convolutions instead of Fourier Transforms.' *Proceedings of the National Academy of Sciences of the United States of America*, **68** (9):2236–2240, 1971.

[42] Rechtien, J., Lautenschlager, E. and Norling, B. 'X-Radiation Spectra.' *J. Dent. Res.*, **51**:1369–1374, 1972.

[43] Riederer, S., Pelc, N. and Chesler, D. 'The Noise Power Spectrum in Computed X-ray Tomography.' *Phys. Med. Biol.*, **23** (3):446–454, 1978.

[44] Röntgen, W. 'Über eine neue Art von Strahlen. Vorläufige Mitteilung.' *Aus den Sitzungsberichten der Würzburger Physik.-medic. Gesellschaft*, pages 137–147, 1895.

[45] Schmidgunst, C. *Untersuchung und Korrektur des Nachleuchtverhaltens von digitalen Flachbilddetektoren für Röntgenstrahlung.* Master's thesis, University of Regensburg, 2004.

[46] Schmidgunst, C. *Modell zur Konditionierung von Festkörperdetektoren für die 2D/3D-Röntgenbildgebung mit mobilen C-Bogensystemen.* Ph.D. thesis, University of Regensburg, 2008.

[47] Schmidgunst, C. and Graumann, R. 'Intraoperative 3D imaging with a mobile C-arm flat panel detector.' *5. Jahrestagung der CURAC*, 2006.

[48] Schmidgunst, C., Ritter, D. and Lang, E. 'Calibration model of a dual gain flat panel detector for 2D and 3D X-ray imaging.' *Medical Physics*, **34** (9):3649–3664, 2007.

[49] Siewerdsen, J.H. and Jaffray, D.A. 'Cone-beam computed tomography with a flat-panel imager: effects of image lag.' *Med Phys*, **26** (12):2635–2647, 1999.

[50] Siewerdsen, J.H. and Jaffray, D.A. 'A ghost story: Spatio-temporal response characteristics of an indirect-detection flat-panel imager.' *Med Phys*, **26** (8):1624–1641, 1999.

[51] Strotzer, M., Gmeinwieser, J., Völk, M., Fründ, R., Seitz, J., Manke, C., Albrich, H. and Feuerbach, S. 'Clinical application of a flat-panel X-ray detector based on amorphous silicon technology: image quality and potential for radiation dose reduction in skeletal radiography.' *Am. J. Roentgenol.*, **171** (1):23–27, 1998.

[52] Szeliski, R. 'Image Alignment and Stitching: A Tutorial.' Technical report, Microsoft Research, 2005.

[53] Thomas, J. *An introduction to Statistical Communication Theory.* John Wiley & Sons, 1969.

[54] Tomasi, C. and Manduchi, R. 'Bilateral Filtering for Gray and Color Images.' *Proc. IEEE Conf. Comp. Vis. Bombay*, 1998.

[55] Turbell, H. *Cone-Beam Reconstruction Using Filtered Backprojection.* Ph.D. thesis, Linköpings Universitet - Institute of Technology, 2001.

[56] Webb, S. *From the watching of shadows : the origins of radiological tomography / Steve Webb.* Adam Hilger, Bristol ; New York :, 1990.

[57] Wei, J., Chen, L., Sandison, G., Liang, Y. and Xu, L. 'X-ray CT high-density artefact suppression in the presence of bones.' *Physics in Medicine and Biology*, **49** (24):5407–5418, 2004.

[58] Wells, P. 'Sir Godfrey Newbold Hounsfield KT CBE. 28 August 1919 - 12 August 2004 : Elected F.R.S. 1975.' *Biogr. Mems Fell. R. Soc.*, **51**:221–235, 2005.

[59] Yaniv, Z. and Joskowicz, L. 'Long Bone Panoramas from Fluoroscopic X-ray Images.' In W. Niessen and M. Viergever (Editors), *MICCAI 2001, LNCS 2208*, pages 1193–1194. Springer-Verlag Berlin Heidelberg, 2001.

[60] Yaniv, Z. and Joskowicz, L. 'Long Bone Panoramas From Fluoroscopic X-Ray Images.' *IEEE Trans. Med. Imag.*, **23** (1):26–35, 2004.

[61] Yazdia, M., Gingras, L. and Beaulieu, L. 'An adaptive approach to metal artifact reduction in helical computed tomography for radiation therapy treatment planning: Experimental and clinical studies.' *International Journal of Radiation Oncology*Biology*Physics*, **62** (4):1224 – 1231, 2005.

[62] Yu, H., Zeng, K., Bharkhada, D., Wang, G., Madsen, M., Saba, O., Policeni, B., Howard, M. and Smoker, W. 'A segmentation-based method for metal artifact reduction.' *Acad. Radiol.*, **14** (4):495–504, 2007.

[63] Zhang, Y., Zhang, L., Zhu, X., Lee, A., Chambers, M. and Dong, L. 'Reducing metal artifacts in cone-beam CT images by preprocessing projection data.' *International Journal of Radiation Oncology*Biology*Physics*, **67** (3):924–932, 2007.